UNIVERSIDAD CARLOS III DE MADRID

TESIS DOCTORAL

Ultra-Wideband Phased Array Antennas for Low-Frequency Radio Astronomy

Autor:
Eloy de Lera Acedo

Director/es:
Dr. Luis Enrique García Muñoz
Dr. Peter James Duffett-Smith

DEPARTAMENTO DE TEORÍA DE LA SEÑAL Y COMUNICACIONES

Leganés, Enero 2010

TESIS DOCTORAL

ULTRA-WIDEBAND PHASED ARRAY ANTENNAS FOR LOW-FREQUENCY RADIO ASTRONOMY

Autor: Eloy de Lera Acedo

Director/es: Dr. Luis Enrique García Muñoz
Dr. Peter James Duffett-Smith

Firma del Tribunal Calificador:

Firma

Presidente:

Vocal:

Vocal:

Vocal:

Secretario:

Calificación:

Leganés, de de

Ultra-Wideband Phased Array Antennas for Low-Frequency Radio Astronomy

Ultra-Wideband Phased Array Antennas for Low-Frequency Radio Astronomy

A THESIS SUBMITTED FOR THE DEGREE OF
DOCTOR OF PHILOSOPHY

By

Eloy de Lera Acedo

Signal Theory and Communications Department,
University Carlos III of Madrid.

Astrophysics Group - Physics Department,
University of Cambridge.

January 2010

Supervisors: Dr. Luis Enrique García Muñoz
University Carlos III of Madrid, Spain
Dr. Peter James Duffett-Smith
University of Cambridge, UK

"It is far better to grasp the Universe as it really is
than to persist in delusion, however satisfying and reassuring"
- Carl Sagan

About the Author

Eloy de Lera Acedo (eloy@mrao.cam.ac.uk) was born in Spain in 1982. He received the M.Sc. degree in electrical engineering (best graduate of the year distinction) from University Carlos III of Madrid in 2005. Then he started working toward the Ph.D. degree in telecommunications at the same university. From 2006 to 2007 he worked at the Yebes Astronomical Center and stayed at the Netherlands Institute for Radio Astronomy (ASTRON) working in the design of array antennas for radio astronomy. Since 2007 he has a position in the Cavendish Laboratory, University of Cambridge. His main research interests include ultra-wideband array antennas as well as radio astronomy receivers.

Acknowledgments

It is a pleasure to thank those who made this thesis possible. But of course "those" are too many and they help in many ways and degrees. I acknowledge here most of the persons who made this happen.

I am heartily thankful to my supervisors, Dr. Luis Enrique García Muñoz and Dr. Peter James Duffett-Smith, whose encouragement, guidance and support from the initial to the final level enabled me to develop an understanding of the subject.

I am grateful to the Department of Signal Theory and Communications of the University Carlos III of Madrid and to the Astrophysics Group of the Cavendish Laboratory, University of Cambridge. These are the centres where most of the work in this thesis was developed. The help of the people working in these places; students, lab assistants, professors, readers, etc. was essential for the completion of this work. Specifically, I would like to thank the head of the Radio Frequency Group of the University Carlos III of Madrid, Dr. Daniel Segovia Vargas, and the head of the Astrophysics Group of the University of Cambridge, Dr. Paul Alexander. I will specially remember the students and postdocs who I spent more time with during my time in Madrid (Oscar, Rocío, Rosa, Rubén, Javi, Bert and Mari Luz) and my time in Cambridge (Nima and Gabriel).

I am indebted to many of my colleagues to support me during these years; to everyone in the OAN (National Astronomical Observatory of Spain), the Yebes Atronomical Center and the FG-IGN (*Fundación General - Instituto Geográfico Nacional*), where I started my research (special thanks to José Antonio, José Manuel and Paco); to everyone in ASTRON (Netherlands Institute for Radio Astronomy) and JIVE (Joint Institute for VLBI in Europe), where I spent 4 wonderful months and I met so many nice people and great scientists (special thanks to Wim, Jan Geralt, Rob, Marianna, Michel, Michelle, David, Oleg, Mona, Sarod, Jan, Harmen, James, Michael, Rebeca, Giuseppe, Roberto, Shafaat and Cedric); and to the people in UCL (*Université Catholique de Louvain*) with whom lately I had the pleasure to work (David and Christophe). I learned and I still learn from all of them. I am also very thankful to my colleagues in the SKADS project (Square Kilometre Array Design Studies). We have shared many occasions together and I have learned a lot from them. To them and to everyone I have met at conferences, workshops and

courses: thank you.

From outside the Engineering and Physics world a very important help has come. This thesis would not have been possible without the support and love of my family and friends.

The most special appreciation is for my sister, Raquel, and my parents, Mari Carmen and Eloy, who have always been there, no matter the distance, which is never easy to handle. Thank you for everything. This gratitude must be extended to everyone in my family, to those who are still here and to those who left, from aunts and uncles to grandparents, whose love and encouragement have been of indeterminable value.

La mayor de las gratitudes es a para mi hermana, Raquel, y mis padres, Mari Carmen y Eloy, quienes siempre han estado ahí para mí sin importar la distancia, que nunca es fácil de llevar. Muchas gracias por todo. Este agradecimiento es también extendido al resto de mi familia, a aquellos que se fueron y a aquellos que siguen con nosotros; mis tías y tíos, mis abuelas y abuelos, etc. Su amor y ánimo han sido de un valor incalculable.

To all my friends, I only have to say that nothing of this makes sense without them being out there to share and enjoy the life with. To those who stayed when I left. To those who traveled long distances to visit me when I wasn't close. To those who wondered about my life when I wasn't there. To the ones with whom I have been traveling around the world and with whom I plan to discover new places and to live new adventures. To those I met in the places I lived and visited. They helped to re-shape the world for me again and again. To all my friends: thank you. Fortunately these are too many to name them here but I hope they know who they are.

Last but no least, thank you to the person who has been closer to me the last 4 years, my girlfriend, Amandine. She appeared in my life soon after this thesis started and she is still there. We have shared many moments together and in the distance too. I have learned so many things from her that a book like this would not even be the introduction if I had to write them.

Specific acknowledgments

Different parts of this thesis have been supported by different people, I would like to specifically acknowledge some of them accordingly to the part of the project they helped in.

In general, the efforts/activities related in this thesis were supported by the European Community Framework Programme 6, Square Kilometre Array Design Studies (SKADS), contract no. 011938. http://www.skads-eu.org/.

I would also like to thank the examiners of this thesis for their efforts in the evaluation of the document: Dr. Paul Alexander, Prof. Anthony Brown, Prof. Magdalena Salazar-Palma, Dr. Daniel Segovia, Dr. José Antonio López, Dr. Marianna V. Ivashina and Prof. Christophe Craeye.

Chapter 3

I would like to acknowledge and thank several entities for the scientific and financial support given to the work described in this chapter:

- ASTRON (Netherlands Institute for Radio Astronomy). In particular to Jan Geralt bij de Vaate (leader of the FLOWPAD^3 project), Rob Maaskant (original idea of the CPS line to slotline transition and scientific support and advice), Michel Arts (Measurements of the final prototype and scientific advice), Marianna V. Ivashina, Michael Zuliani and Wim Van Cappellen (scientific advice).

- FG-IGN (*Fundación General - Instituto Geográfico Nacional*).

- Yebes Astronomical Center (part of the National Astronomical Observatory of Spain).

- University Carlos III of Madrid and University of Cambridge.

- David Zhang (University of Manchester) for the measurement of FLOTT.

- MARIE CURIE grants.

- RADIONET.

- NL-IS-PACMAN.

- The antenna foil production has been sponsored by MECO Equipment Engineers B.V.

Chapter 4

I would like to thank the Yebes Astronomical Center and the National Astronomical Observatory of Spain for its support, comments and suggestions. Also I would like to thank Prof. D. H. Schaubert for his comments, suggestions and time spent in private communications. Furthermore, I would like to thank my co-authors, colleagues and advisors in the University Carlos III of Madrid (Dr. José Luis Vázquez- Roy, etc.), Dr. Vicente González-Posadas, from *Universidad Politécnica de Madrid,* and Rob Maaskant, from the Netherlands Institute for Radio Astronomy (ASTRON).

Chapter 5

I am grateful to my SKA colleagues in the University of Cambridge for several discussions around the topics discussed in this chapter.

Chapter 6

I would like to thank Prof. Christophe Craeye from the *Université Catholique de Louvain* for his advise and supervision of the work described in this chapter and the work still on going. Furthermore, I would like to thank David González Ovejero, research assistant at *Université Catholique de Louvain* for his efforts and work, in which the research presented in this chapter is based. Also, I would like to thank my colleagues in the University of Cambridge (specially Dr. Nima Razavi-Ghods).

List of Publications

The works related to the contents of this thesis are also described in the following publications:

Journals

- E. de Lera Acedo, N. Razavi-Ghods, E. García, P. Duffett-Smith, and P. Alexander, "Ultra Wide-Band Aperture Array Element Design for Low Frequency Radio Astronomy," submitted to the special issue on *Antennas for Next Generation Radio Telescopes, IEEE Transactions on Antennas and Propagation.*

- E. de Lera Acedo, E. García, V. González-Posadas, J. L. Vázquez-Roy, R. Maaskant, and D. Segovia, "Study and design of a dierentially-fed tapered slot antenna array," *IEEE Transactions on Antennas and Propagation*, vol. 58, pp. 68-78, January 2010.

- E. García, E. de Lera Acedo, and E. Rajo, "Tapered slotline antenna modification for radiation pattern improvement," *Microwave and Optical Technology Letters*, vol. 49, no. 10, pp. 2590-2595, 2007.

Conference papers

- E. de Lera Acedo, N. Razavi-Ghods, D. González-Ovejero, E. García, C. Craeye, P. J. Duett-Smith, and P. Alexander, "The SKA AA-lo array; e.m. simulation and design," in *Wide Field Science and Technology for the SKA - SKADS Conference 2009*, (Chateau de Limelette, Belgium), November 2009.

- E. de Lera Acedo, N. Razavi-Ghods, E. García, P. J. Duett-Smith, and P. Alexander, "System noise analysis of an ultra wide band aperture array element for low frequency radio astronomy," in *Proceedings of the 6th IASETD International Conference Antennas, Radar, and Wave Propoagation (ARP 2009)*, (Ban, Alberta, Canada), July 2009.

- D. González-Ovejero, E. de Lera Acedo, N. Razavi-Ghods, and C. Craeye, "Fast MBF-based method for large random array characterization," in *IEEE Antennas and Propagation Society International Symposium, APSURSI '09*, (Charleston, SC), pp. 14, 1-5 June 2009.

- E. de Lera Acedo, N. Razavi-Ghods, E. García, P. J. Duett-Smith, and P. Alexander, "Analysis of an ultra wideband aperture array element for low frequency radio astronomy," in *IEEE Antennas and Propagation Society International Symposium, APSURSI '09*, (Charleston, SC), pp. 14, 1-5 June 2009.

- O. García-Perez, L. García-Muñoz, E. de Lera Acedo, J. Serna-Puente, V. González-Posadas, J. Vázquez-Roy, and D. Segovia-Vargas, "Differential active antennas for the SKA," in *3rd European Conference on Antennas and Propagation 2009, EuCAP 2009*, (Berlin), 23-27 March 2009.

- M. Arts, R. Maaskant, E. de Lera Acedo, and J. G. bij de Vaate, "Broadband differentially-fed tapered slot antenna array for radio astronomy applications," in *3rd European Conference on Antennas and Propagation 2009, EuCAP 2009*, (Berlin), pp. 566-570, 23-27 March 2009.

- E. García, E. de Lera Acedo, V. González, and D. Segovia, "Elimination of scan impedance anomalies in ultra-wide band phased arrays of differentially-fed tapered slot antennas," in *XXIII Simposium Nacional de la Unión Cientíca Internacional de Radio, URSI'08*, (Madrid), 12-15 September 2008.

- E. García, E. de Lera Acedo, D. Segovia, and V. González, "Elimination of scan impedance anomalies in phased arrays," in *IEEE Antennas and Propagation Society International Symposium 2008*, (San Diego, CA), pp. 14, 5-11 July 2008.

- E. de Lera Acedo and E. García, "Mutual coupling edge effect approximation for phased-array antennas," in *IEEE AP-S International Symposium 2007*, (Honolulu, Hawaii, EEUU), 11-15 June 2007.

- E. de Lera Acedo, E. García, E. Rajo, J. A. López, J. M. Serna, and M. Azuaga, "Dipolo plano de banda ancha con balanceador de corriente integrado," in *XXI Simposium Nacional de la Unión Cientíca Internacional de Radio, URSI'06*, (Oviedo, Spain), pp. 1227-1231, 12-15 September 2006.

- E. de Lera Acedo, E. García, E. Rajo, and D. Segovia, "A coplanar vivaldi antenna with wideband balun proposal for the low frequency band of the SKA: approach to the FPA solution," in *IEEE Mediterranean Electrotechnical*

Conference 2006, MELECON 2006, (Benalmádena, Málaga, Spain), pp. 557-560, 16-19 May 2006.

Workshops

- E. de Lera Acedo, "Low costing arrays of differentially-fed TSA elements," in *SKADS MCCT Technical Workshop on Design of Wideband Receiving Array Systems*, (Dwingeloo, The Netherlands), 26-30 November 2007. available on http://www.astron.nl/other/workshop/MCCT/index.php.

- E. de Lera Acedo, "Differential dual-polarized antenna array design," in *2nd SKADS Workshop and Mid Term Review*, (Meudon, France), 10-11 October 2007.

Technical reports

- E. de Lera Acedo, "PACMAN FLOWPAD^3 demonstrator (PACMAN active tile with cots lna) - antenna design and performance analysis," technical report, Dwingeloo, The Netherlands, June 2007. Available on http://www.skadseu.org/.

Nomenclature

B2B Back-to-Back

D-plane It is the diagonal plane between the E- and H-planes. In this thesis it is usually used for the D-plane of one of the antennas in the unit cell

DLNA Differential Low Noise Amplifier

E-plane It is the plane containing the electric field vector. In this thesis it is usually used for the E-plane of one of the antennas in the unit cell

FOV Field-Of-View

H-plane It is the plane containing the magnetic field vector. In this thesis it is usually used for the H-plane of one of the antennas in the unit cell

LNA Low Noise Amplifier

MBF Macro Basis Function

MoM Method of Moments

PCB Printed Circuit Board

SKA Square Kilometre Array

SKA-AAhi Square Kilometre Array - Aperture Array high band

SKA-AAlo Square Kilometre Array - Aperture Array low band

TSA Tapered Slot Antenna

VSWR active Voltage Standing Wave Ratio (in an array environment)

Contents

Chapter 1

Introduction

We see the world around us because our eyes are sensible to electromagnetic waves at certain frequencies, called the visible light. However, objects on Earth and the Universe emit radiation in other portions of the electromagnetic spectrum, among them radio waves. The study of the celestial objects in these radio frequencies is known as radio astronomy.

2009 was the International Year of Astronomy. Nowadays astronomers can study and unveil many of the mysteries of the Universe. For instance they can observe the cosmic microwave background radiation, which is the remnant signal of the birth of our Universe in the Big Bang. 2009 was also the 200^{th} anniversary of Charles Darwin's birth, who once said about life: "There is grandeur in this view of life... from so simple a beginning endless forms most beautiful and most wonderful have been, and are being, evolved". The Universe also evolves in its own way. To understand better this process of evolution, new radio astronomy instruments (radio telescopes) and techniques are being developed all around the world.

The "Dark Ages", the time before the first stars or galaxies, and the earliest generation of them, are also a matter of study for the latest radio telescopes. Since radio waves penetrate dust, scientists use radio astronomy techniques to study regions of the sky that cannot be seen in visible light by optical telescopes, such as the environments where stars and planets are born, and the center of our Galaxy, the Milky Way. Radio waves also allow astronomers to locate and trace the density and motion of the hydrogen gas that forms 75% of the ordinary matter in the Universe. The black holes that live at the centre of most galaxies, pulsars or the origin and evolution of cosmic magnetism are examples of key scientific projects which need from powerful radio telescopes.

The contents of the first section on the history of radio astronomy are extracted from 6 main sources [1, 2, 3, 4, 5, 6].

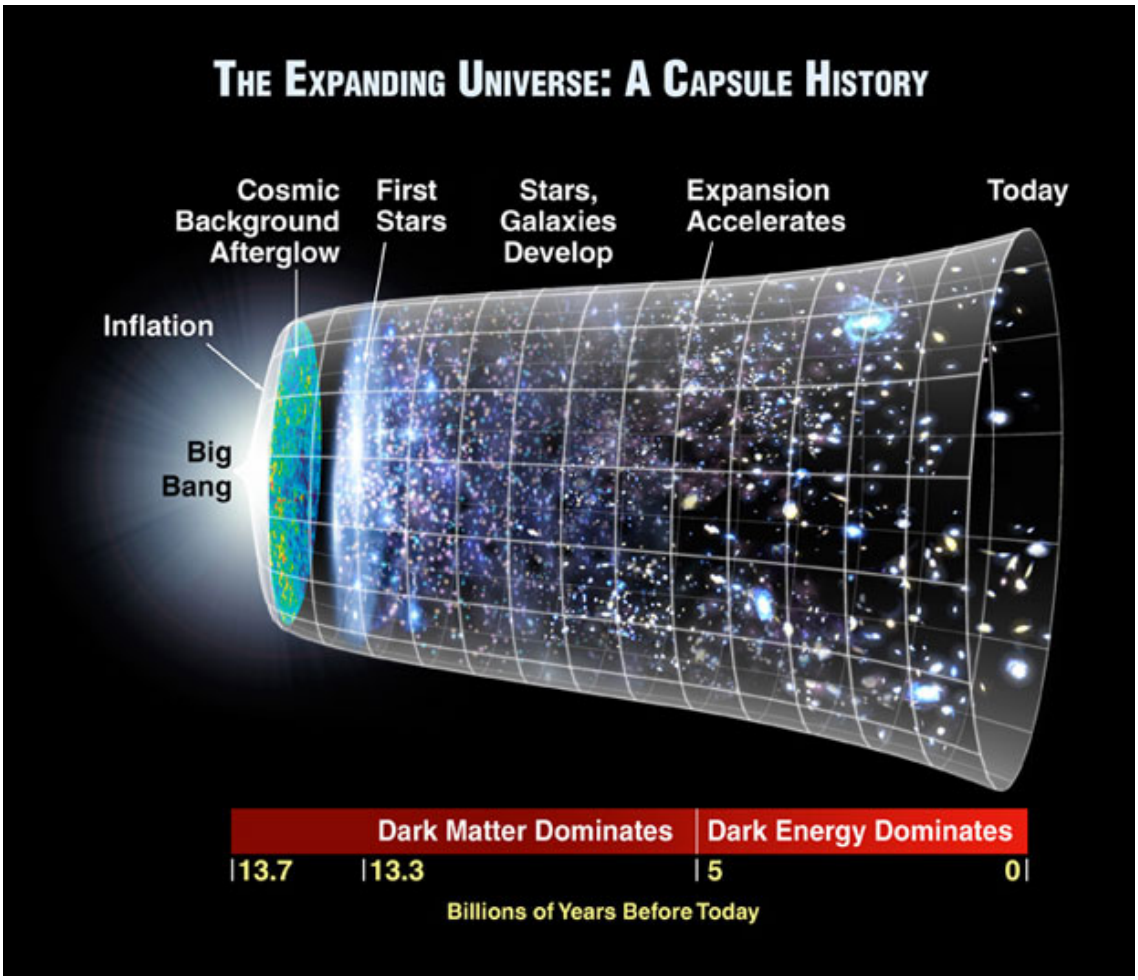

Figure 1.1: History of the Universe. Image available on http://hetdex.org/dark_energy/index.php.

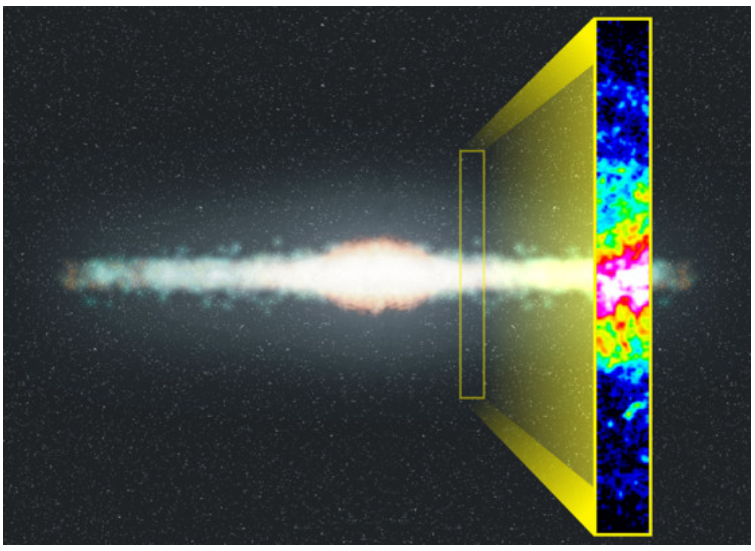

Figure 1.2: Cross-section of Milky Way Galaxy's diffuse halo of hydrogen gas. Image courtesy of NRAO/AUI.

1.1 History of radio astronomy

Astronomy is the science which investigates all the matter-energy in the universe: its distribution, composition, physical states, movements, and evolution. It is concerned with the evolution, physics, chemistry, meteorology, and motion of celestial objects, as well as the formation and development of the Universe. Astronomy is one of the oldest sciences, however, at present time, state-of-the-art technologies allow scientist to study the Universe not only in the visible region of the spectrum but in other frequencies too. When these frequencies are between 3 Hz and 300 GHz they are called radio waves, and the science in charge of studying them, radio astronomy.

The initial detection of radio waves from an astronomical object (the Milky Way) was made in the 1930s. However, almost 70 years before the story began. James Clerk Maxwell's equations had shown that electromagnetic radiation from stellar sources could exist with any wavelength, not just optical. Several scientists such as Nikola Tesla, Oliver Lodge, and Max Planck predicted that the sun should be emitting radio waves. It was however Karl Guthe Jansky the first person to identify the first astronomical radio source. In the early 1930s Jansky was an engineer working for Bell Telephone Laboratories, who was investigating static that interfered with short wave transatlantic voice transmissions. Using a large directional antenna, Jansky found a repeating signal of unknown origin. A more thought analysis showed that the source was not exactly following the 24 hour daily cycle of the Sun, as suspected by Jansky at the beginning, but instead repeating on a cycle of 23 hours and 56 minutes. Jansky helped by the astrophysicist A. M. Skellett concluded that the radiation was coming from the Galaxy and its peak was in the direction of the center of the Milky Way. He announced his discovery in 1933. Jansky was unfortunately re-assigned by Bell-Labs to another project, so he did no further work in the field of astronomy. However, his work in the field of radio astronomy have been recognized by the naming of the fundamental unit of radio flux density, the Jansky (Jy), after him.

Soon after Jansky made his pioneering discovery, Grote Reber built a large parabolic reflector in his back yard (9 m in diameter) in 1937. He was trying to repeat Karl Jansky's observations, and went on to conduct the first sky survey in the radio frequencies. In 1942, J.S. Hey, a British Army research officer, found that the Sun emits radio waves. By the early 1950s Martin Ryle and Antony Hewish at Cambridge University had used the Cambridge Interferometer to map the radio sky, producing the famous 2C and 3C surveys of radio sources.

The difficulty in achieving high resolutions with single radio telescopes led to radio interferometry, developed by Martin Ryle, Joseph Lade Pawsey and Ruby Payne-Scott in 1946. The Australia group of Payne-Scott, Pawsey and Lindsay

McCready set up the principles of aperture synthesis in their paper published in 1947. The Cambridge group of Ryle and Vonberg observed the sun at 175 MHz for the first time in mid July 1946 with a Michelson interferometer consisting of a two radio antennas with spacings of some tens of metres up to 240 metres. Modern radio interferometers consist of widely separated radio telescopes observing the same object that are connected together. On top of the increase in resolution this also increases the total signal collected. The aperture synthesis technique works by interfering the signal waves from the different telescopes on the principle that waves that coincide with the same phase will add to each other while two waves that have opposite phases will cancel each other out. This creates a combined telescope that is the size of the antennas furthest apart in the array.

An example of an interferometer active nowadays is the Very Large Array (VLA), with 27 telescopes giving 351 independent baselines at once. Very Long Baseline Interferometry (VLBI) beginning in the 1970s, improved the sensitivity of radio telescopes to a dimension where one can synthesise an antenna that is effectively the size of the Earth. In VLBI, the data collected from different telescopes around the world, is post-correlated to produce a very high resolution image. Each array usually operates separately, but occasional projects are observed together producing increased sensitivity. This is referred to as Global VLBI. The availability today of worldwide, high-bandwidth optical fiber networks makes it possible to do VLBI in real time. This technique (referred to as e-VLBI) was pioneered by the EVN (European VLBI Network) who now perform an increasing number of scientific e-VLBI projects per year. Another example of VLBI is the Very Long Baseline Array.

Up to now, many telescopes have been used to explore the universe. Some of them are ground-based and others are mounted on satellites or spacecrafts. One of the most relevant telescopes, currently under construction, is the Atacama Large Millimeter Array (ALMA). It is an international project that consists of an interferometer formed from an array of radio telescopes, located in the Atacama desert in northern Chile. The telescope will work in millimeter and submillimeter wavelengths and is expected to revolutionize modern astronomy by providing an insight on star formation in the early Universe and imaging local star and planet formation in great detail. Other recent instruments are the Planck Space Observatory and the Herschel Space Observatory, both recently launched in 2009. The Planck Space Observatory is a space observatory designed to observe anisotropies of the cosmic microwave background over the entire sky, using high sensitivity and angular resolution. The Herschel Space Observatory was originally proposed in 1982 by a consortium of European scientists. Herschel can image the coldest and dustiest objects in space; for example, cool cocoons where stars form and dusty galaxies just starting to bulk up with new stars. In the optical range, an example of a state-of-

the-art instrument is the *Gran Telescopio de Canarias* (meaning "Canaries Great Telescope"), also known as GranTeCan or GTC. It is a 10.4 m reflecting telescope undertaking commissioning observations at the Roque de los Muchachos Observatory on the island of La Palma, in the Canary Islands of Spain, as of July 2009. During the last 60 years, a large number of telescopes have been in use; mentioning all of them is beyond the scope of this thesis.

Currently, several telescopes are being upgraded or planned, but in this thesis I will concentrate on one of them: the Square Kilometre Array. More information is given in the references provided at the beginning of this chapter. The Square Kilometre Array (SKA) [7] represents the next big step in radio astronomy. This interferometer will be 50 times more sensitive than any current instrument and several thousand times faster at surveying the sky. The next section is about the SKA project, which is the framework of the studies and prototypes designed in this thesis.

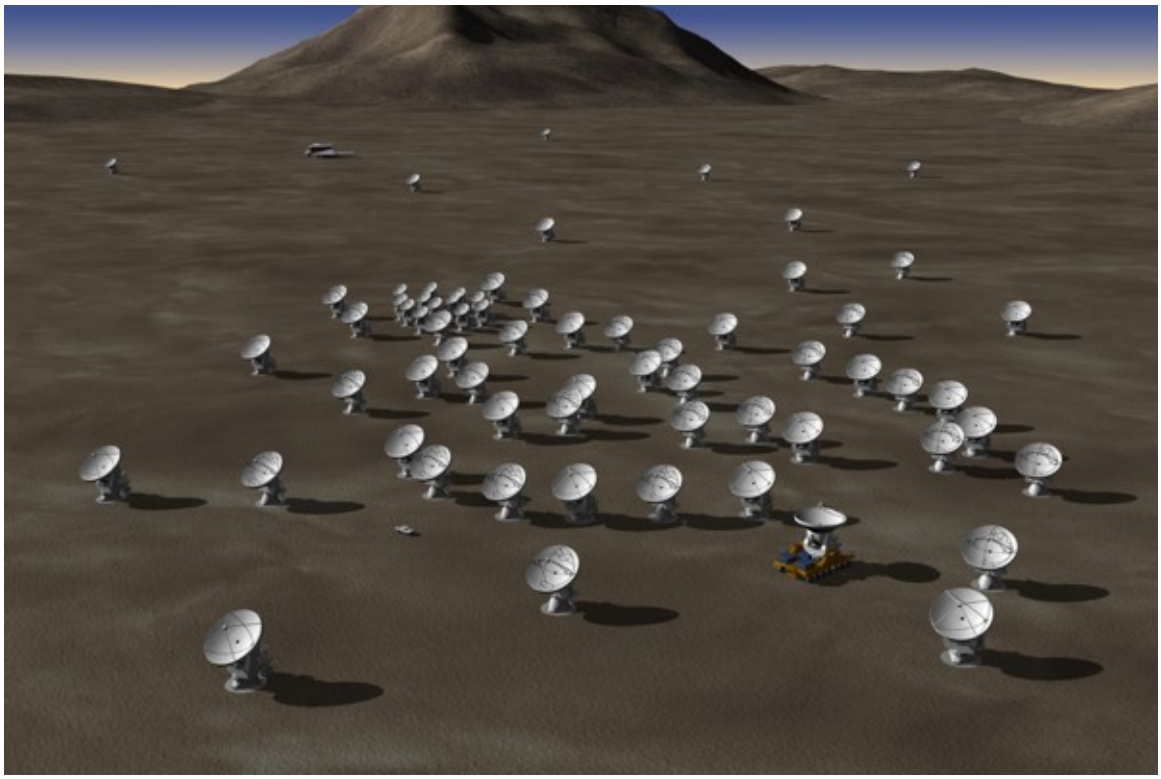

Figure 1.3: Artist's impression of ALMA. Image courtesy of NRAO/AUI.

1.2 Motivation - the SKA

The SKA will be a radio telescope with a total collecting area of approximately one square kilometre. It will be fully operational by around 2020 and will look at the sky over a wide range of frequencies (70 MHz to 10 GHz). By making use of powerful

back-ends to process the digital signal it will be able to survey the sky more than ten thousand times faster than ever before. With receiving stations extending out to a distance up to several thousand kilometres from a central core, it will provide the highest resolution images in all astronomy. The SKA will be located either in South Africa or Australia, both in the southern hemisphere, where the view of the Galaxy is best and radio interference least. With a total budget of €1.5 billion, the SKA is a global collaboration of 19 countries which will revolutionise our understanding of the Universe by providing answers to fundamental questions about its origin and evolution. The funding will come from many international funding agencies. Preliminary expectations are that Europe, the United States and the rest of the world will each contribute a third of the project's funding.

At sub 1 GHz frequencies the SKA will combine (as a 250 stations interferometer) the signals received from thousands (up to millions) of small antennas spread over a distance of more than 3,000 km to achieve a radio telescope capable of extremely high sensitivity and angular resolution. The SKA will also have a very large Field-Of-View (FOV) with a goal at frequencies below 1 GHz of 200 square degrees and of more than 1 square degree at higher frequencies. The use of phased array technology to provide multiple FOVs will also be largely exploited in the SKA. It will greatly increase the survey speed of the SKA and enable multiple users to run different observation process over different pieces of the sky simultaneously (see Fig. 1.4). The SKA is one of the most ambitious scientific projects in development at world level and it will require state-of-the-art technology in several fields: antennas, amplifiers, beamforming, communications, power supply, calibration, data storage, processing, etc.

The SKA was originally conceived in the early 1990s with an international working group set up in 1994. This led to the signing of the first Memorandum of Agreement in 2000. Considerable early development work then followed. This culminated in the commencement of PrepSKA (http://www.jb.man.ac.uk/prepska/) in 2008 leading to a full SKA design in 2012.

Although it is not decided yet (see [8] for more information), a likely scenario for the SKA construction is as follows. The phase 1 will provide approximately 20% of the total collecting area at low and mid frequencies by 2017. The phase 2 completion will represent a fully operational array at low ($<$ 450 MHz) and mid frequencies (300 - 1000 MHz) by 2022. A third phase of the telescope may extend the frequency range up to 30 GHz.

- SKA-AAlo: A phased array of low profile antennas to cover the frequency range from 70 - 450 MHz. These will be grouped in $\sim$ 200 m diameter stations each containing about 15,000 elements placed in a non-regular sparse configuration.

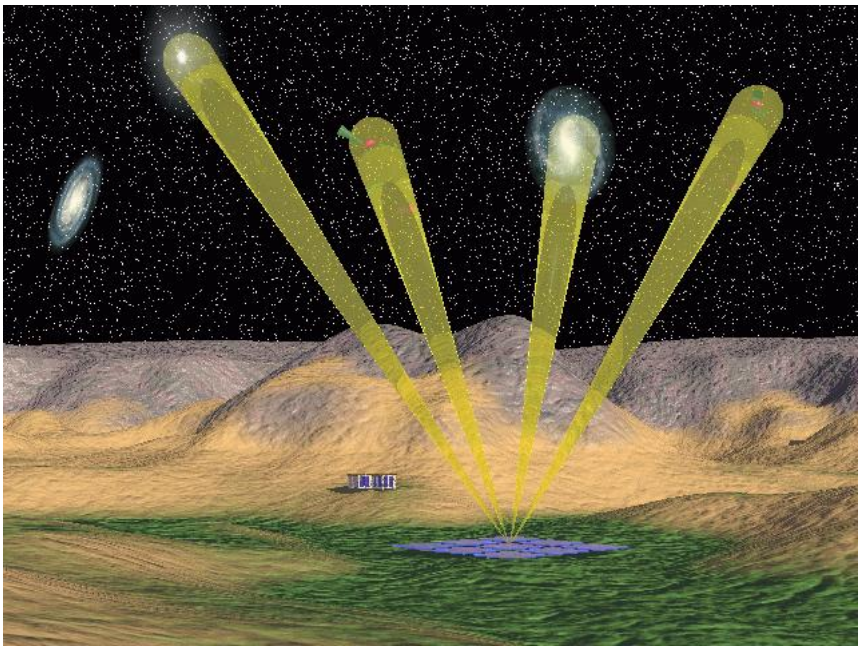

Figure 1.4: SKA's multiple fields-of-view. Image available on www.skatelescope.org.

- SKA-AAhi: This is likely to be a phased array of "tiles" to cover the medium frequency range from 300 to 1000 MHz. The tiles will be grouped into circular stations, ~ 60 m in diameter and around 75,000 elements per polarization and station. This would represent a dense regular array sampled at the high end of the band.

- Dish Array: Several thousand dish antennas to cover the frequency range 500 MHz to 10 GHz. The parabolic dishes would be equipped with focal plane arrays at their focus for the sub 3 GHz frequencies and wideband feeds up to 10 GHz. These focal plane arrays would allow the dishes to observe over a far wider field-of-view than that achieved with a single element feed.

The central region of the SKA will contain approximately half of the total collecting area of the three SKA arrays. A mid region will extend out to 180 km. This will contain dishes and pairs of SKA-AAlo and SKA-AAhi stations. An outer region will be located from 180 km to 3,000 km away from the core.

The SKA will be a highly flexible instrument designed to address a wide range of questions in astrophysics, fundamental physics, cosmology and particle astrophysics. It will be able to probe previously unexplored parts of the distant Universe. A number of key science projects have been selected:

- Extreme tests of general relativity.

- Galaxies, cosmology, dark matter and dark energy. The large-scale structure revealed will determine the processes by which galaxies formed and grew.

- Probing the dark ages.
- The origin and evolution of cosmic magnetism.
- The cradle of life.
- The search for extraterrestrial intelligence.
- Exploration of the unknown. History has shown that many of the greatest historical discoveries have happened unexpectedly. The unique sensitivity and versatility of the SKA will make it a discovery machine.

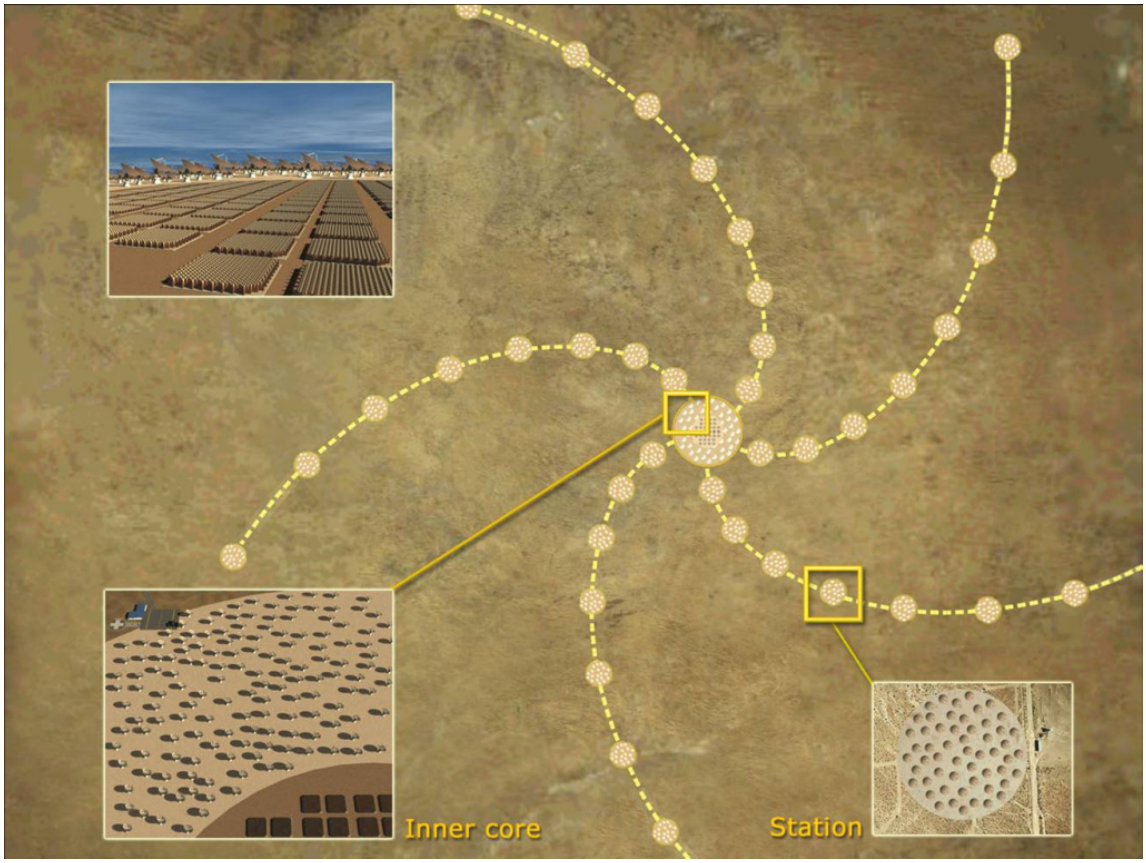

Figure 1.5: Computer image of a possible SKA. Image available on www.skatelescope.org.

Suitable sites for the SKA need to be in unpopulated areas with guaranteed very low levels of man-made radio interference. After considerable site evaluation surveys, two sites are now shortlisted:

- Australia: The core site is located at Boolardy 26°59′S 116°32′E in Western Australia 315 km north-east of Geraldton on a flat desert-like plain at an elevation of about 460 metres (see Fig. 1.6(a). Image available on www.skatelescope.org). The most distant stations would be located in New Zealand.

- South Africa: The core site is located at S30.72113° - E21.41113° at an elevation of about 1000 metres in the Karoo area of the arid Northern Cape Province, about 75 km north-west of Carnarvon (see Fig. 1.6(b). Image available on www.scienceinafrica.co.za), with distant stations in Ghana, Kenya, Madagascar, and Mauritius.

The final decision on the site will be made between 2011 and 2012.

(a) Australia (b) South Africa

Figure 1.6: SKA candidate sites.

Many groups are working globally to develop the technology and techniques required for the SKA. Some of these are:

- MeerKAT: MeerKAT is a 860 million Rand project to build an array of 50 or more 12 m diameter dishes to enable technology required for the SKA to be developed.

- KAT-7: A seven-dish engineering testbed and science instrument near Carnarvon in the Northern Cape Province of South Africa, will be ready to do science by 2012. The dishes will be equipped with wideband single feeds to cover frequencies from 800 MHz up to 8 GHz.

- Australian SKA Pathfinder: The Australian SKA Pathfinder, or ASKAP, is a AU$ 100 million project to build an array of 36 12 m dishes employing advanced phased array feeds to give a wide field of view (30 square degrees). ASKAP will be built on the Australian Boolardy site. Completion of the array which covers the frequency range 700 to 1700 MHz is scheduled for 2012.

- LOFAR: LOFAR (LOw Frequency ARray) is a €120 million Dutch project building novel low-frequency phased aperture arrays spread over northern Europe. It is an all-electronic telescope covering low frequencies from 10 to 250 MHz. Its completion was in progress in 2009. LOFAR will demonstrate crucial processing techniques vital to the SKA.

- Allen Telescope Array: The Allen Telescope Array (ATA) uses innovative 6.1 m offset Gregorian dishes equipped with wideband single feeds covering frequencies from 500 MHz to 11 GHz. A 42 element array is currently in operation to be extended to 350. The dish design has explored methods of low-cost manufacture.

- Square Kilometre Array Design Studies: The Square Kilometre Array Design Studies, or SKADS, is a €38 million European funded project to develop a range of technologies and science studies for the SKA. The focus of the technical developments are high frequency aperture arrays operating from 300 MHz to 1 GHz. As an all-electronic telescope, aperture arrays can provide a very large number of simultaneous beams to provide the highest survey speeds.

- Technology Development Programme: The Technology Development Programme, or TDP, is a $12 million US programme to specifically develop dish and feed technology for the SKA. It is operated by a consortium of universities led by Cornell University and completes in 2012.

In the context of the SKA and the SKADS, in this thesis I explore antenna technologies to cover the sub 1 GHz frequency band of the telescope. I study and design array antennas to cover the high frequency band of the aperture array proposal for the SKA (300 MHz to 1 GHz) using dense arrays and the sub 450 MHz band using sparse arrays. Special effort is put on analyzing possible issues, such as narrow band anomalies, related to the use of ultra-wideband differential technology. Low-cost and high sensitivity are the main objectives of the designs I present in this thesis. The chapters are arranged in chronological order. First I elaborate on dense arrays of Tapered Slot Antennas (TSAs) to cover the SKA-AAhi band. This work was done during my 4 months internship in the Netherlands Institute for Radio Astronomy in 2007, the time I worked for the Yebes Astronomical Center since January 2006 until September 2007 and the time I have been a graduate student at the *Universidad Carlos III de Madrid* since October 2005. After, I present the work I have done on sparse arrays of bow-tie antennas for low-frequency radio astronomy since I started my work at the Cavendish Laboratory, University of Cambridge, UK, in September 2007. Finally I conclude with a chapter on characterization of large irregular arrays of ultra-wideband antennas for low-frequency radio astronomy. This work started in 2009 when I was already in Cambridge and it was done in close collaboration with the *Université Catholique de Louvain*, Belgium.

1.3 Organization and contributions

This thesis is organized as follows:

- Chapter 2 is dedicated to define some important concepts for phased array antennas and to summarize the state-of-the-art of phased array antennas for radio astronomy.

- Chapter 3 relates the design and measurement process of low-cost differentially-fed phased array antennas for modern radio astronomy applications, mainly, the SKA. All the aspects of a fundamental design are considered: the choice of materials and its evaluation, the electromagnetic design and optimization of the feeding system and the antenna structure, and the measurement of the most representative parameters of the array. The main contribution of this chapter is the novel design of a low-cost differentially-fed array and its measurement. Two demonstrator instruments for the SKA have been built based on the designs presented in this chapter: **FLOWPAD**^{3} (Foil-based LOW-cost PAcman Differential Dual-polarized Demonstrator) and **FLOTT** (FlowPAD Towards TwoPAD).

- Chapter 4 focuses on the design of a differentially-fed array free of dielectric material to cover the mid frequency band of the SKA. In this chapter special attention is dedicated to the analysis and solution of narrow band anomalies which arise when the array is scanned to a particular angle. The study of these anomalies and the novel design of the array are the main contributions of this chapter. A prototype array antenna for the SKA has been built based on the designs presented in this chapter: **FIDA**^{3} (FG-IGN Differential Active Antenna Array).

- Chapter 5 explains the design of a sparse array to cover the low-frequency band of the SKA. The main issues in the design of low-frequency large array antennas for radio astronomy are considered as well. The sensitivity of the array is the main figure of merit analyzed. A choice of a bow-tie antenna is justified and a modification to the basic structure shows an improvement in the system performance. The analysis in terms of sensitivity of a sparse array for a noise limited application and the novel design of the low-profile bow-tie antenna element are the main contributions of this chapter. The **BLU antenna** (Bow-tie Low-frequency Ultra-wideband antenna) is a prototype built after the designs presented in this chapter.

- Chapter 6 presents a novel technique based on a numerical method to electromagnetically simulate very large array antennas of sizes up to hundreds of

wavelengths, such as SKA stations. The extension of the original method to simulate SKA size stations is the main contribution of this chapter.

- Chapter 7 summarizes the most important aspects learned from the preparation of this thesis and the main goals achieved during its development. The specific contributions I have made with this thesis are explained and some general future lines of work are proposed.

Each chapter has its own introduction, conclusions and future lines of work as well.

Chapter 2

On the State-of-the-Art Theory and Technology in Phased Antenna Arrays for Radio Astronomy

This chapter is dedicated to the review of the state-of-the-art of the theory and the technology in phased antenna arrays. The reader will find in this chapter a review of modern array theory relevant for this thesis, with special consideration given to ultra-wideband systems and mutual coupling effects. Also, focusing on radio astronomy applications and Aperture Arrays [9], the state-of-the-art in designing tools and prototype technologies are reviewed. Furthermore, a list of definitions of relevant parameters on phased array theory is given.

2.1 Introduction

A good approach to classical array theory may be found in e.g. [10, 11]. However, any serious ultra-wideband phased antenna array design must take into account mutual coupling. There are the books where one could find information about it. A very well recognized book for phase array theory where mutual coupling is analyzed in detail is [12], by R. C. Hansen. Another book where one could find information on mutual coupling is [13], by R. J. Mailloux. The analytical modelling of mutual coupling is not very well developed yet, due to the complexity of the electromagnetic interactions taking place in complex structures. Other than a few analytical descriptions of specific phenomena associated to mutual coupling, such as narrow band anomalies in phased arrays of dipoles or tapered slot antennas, e.g. [14, 15], only analytical descriptions of mutual coupling for very basic structures can be found in the literature, e.g. [12]. These studies are summarized in section 2.3. It is important to mention that in this thesis "transmission" and "reception" are

exchanged sometimes using the reciprocity theorem [11].

The most of the efforts nowadays go towards characterization of the effects associated with mutual coupling through electromagnetic simulations based on numerical methods. These tools, either commercial [16, 17] or home-brew [18, 19], are also used to design complex phased arrays of up to several hundred elements (or thousands of elements as explained in chapter 6).

In radio astronomy at several GHz one can find the classical dish antennas, where either the feed is realized as a wide band single antenna, such as the classical horn antennas, or as a focal plane array, which is a phased array which allows multiple beams within the field-of-view. Examples of focal plane arrays can be found in [20, 21]. At frequencies below $\sim$1 GHz, aperture arrays are being developed for the next generation radio telescopes. Examples of these are e.g. LOFAR (LOw Frequency ARray) [22] or EMBRACE (Electronic Multi-Beam Radio Astronomy ConcEpt) [23]. In section 2.4 these and other demonstrators are presented.

I begin with a definition of terms.

2.2 Definition of terms

In this section several terms which are widely used within the context of radio astronomy applications and phased antenna arrays are described. This list includes all the terms of importance for a clear reading of this thesis.

2.2.1 Ultra-wideband

In this thesis, the term "ultra-wideband" refers to the capacity of an antenna system to perform properly according to a certain figure of merit (typically the active reflection coefficient) in a very wide range of frequencies (3:1 or more). In [10] "broadband" antennas are defined to have impedances and beam patterns which do not change significally for a band of 2:1 or lager. In any case this implies that the response of the system to a wideband signal would be adequate. Typically, in radio astronomy applications, the signals coming from the sky are processed in narrowband channels. However, the advantage of having ultra-wideband antenna systems (so as LNAs (Low Noise Amplifiers) and beamforming networks) is the cost saving. Furthermore, if a certain bandwidth of frequencies would be covered with different antenna arrays, it would not be possible to locate these in the same spatial position. Certainly this is true for dense arrays.

2.2.2 Unit cell

For the infinite array simulations in this thesis, it is defined as the smallest periodic portion of the array. For example, for dense arrays of dual-polarized tapered slot antennas, a unit cell can be any square portion of the array with side length equal to the spacing between elements. In this case it must include one port per polarization (see Fig. 3.19). In commercial available software packages, such as CST or HFSS [16, 17], one can solve for the electromagnetic fields in an infinite array by imposing certain periodic boundary conditions in the walls of a portion of the array such as a unit cell. This trick reduces the complexity of the simulation with respect to solving the system of equations for a large array. In this thesis, when a unit cell containing two identical antennas (one per polarization) is analyzed, I present the results for one of the antennas, unless otherwise stated.

2.2.3 Mutual coupling

The mutual coupling effects include those electromagnetic effects related to the coupling of currents and fields between closely located elements.

2.2.4 Active impedance

In an array antenna, is the impedance of an element when all the elements of the array are excited (connected to a generator and an identical impedance). The real part of the active impedance represents the power leaving the array structure while the imaginary part is related to the energy stored in the array.

2.2.5 Active reflection coefficient

It is the reflection coefficient of an antenna in the "active" mode of the array, i.e. when all the other antennas of the array are also excited (in a transmission sense). It was introduced by Hannan in [24] and typically given as the Greek letter Γ (or Γ_{act}). Then, between brackets, one indicates the scan angles for which this active reflection coefficient is calculated, i.e. $\Gamma(\theta_0, \phi_0)$. In the situation defined by the active reflection coefficient all the elements of the array are connected to a signal generator and an impedance, identical for all of them. The active return loss will also be represented in this document by the active Voltage Standing Wave Ratio (VSWR).

2.2.6 Embedded element pattern

The Embedded Element Pattern, also known as *Scan Element Pattern*, is the pattern of an array when one element is excited and all the other elements are loaded with the same impedance. In this situation the pattern of the array is referred as the embedded element pattern of the excited element. From section 7.2.3 of [12] it can be derived as Eq. 2.1.

$$G_{eep}(\theta, \phi) = G_{iso}(\theta, \phi) \cdot (1 - |\Gamma(\theta, \phi)|^2) \tag{2.1}$$

It is important to note that in [12] the active reflection coefficient is called *scan reflection coefficient*. Also, note that in Eq. 2.1 three situations of the array are mixed. The "active" situation is when all the elements are excited to point to a certain direction defined by the angles θ_0 and ϕ_0, and this condition is represented in Eq. 2.1 by the active reflection coefficient, $\Gamma(\theta, \phi)$. Therefore $\theta_0 = \theta$ and $\phi_0 = \phi$. The "open circuit" situation describes the situation when all the elements (except for the element of interest) are open circuited. This is represented by the isolated element pattern $G_{\text{iso}}(\theta, \phi)$. And finally one can identify the "passive" situation, which is when all the elements (except for the one of interest which is loaded and excited) are loaded with the same impedance. This is represented by the embedded element pattern. From [12] one can read the following description.

> "A most important and useful parameter is *scan impedance*; it is the impedance of an element as a function of scan angles, with all elements excited by the proper amplitude and phase. From this the *scan reflection coefficient* is immediately obtained. Array performance is then obtained by multiplying the isolated element power pattern (normalized to 0 dB max) times the isotropic array factor (power) times the impedance mismatch factor (1 - $|\Gamma|^2$). The isolated element pattern is measured with all other elements open-circuited. This is not quite the same as with all other elements absent, except for canonical minimum scattering antennas (see next section). Here it is assumed that the array is sufficiently large that edge effects are negligible and that *scan impedance* is that for an infinite array. This simple performance expression allows the contributions of array lattice and element spacing, element type, and mutual coupling to be discerned.
>
> An equivalent array performance expression combines the isolated element pattern and the impedance mismatch factor into a new parameter, the *scan element pattern* (SEP) (formerly active element pattern). Now the overall array performance is the product of the isotropic array factor and the *scan element pattern*. The former shows the array beamwidth

and sidelobe structure for the scan angle of interest; the latter, like the isolated element pattern, is slowly varying, and shows array gain versus scan angle. Unlike *scan impedance*, which is difficult to measure as all elements must be properly excited, *scan element pattern* is measured with one element excited and all other elements terminated in Z_0. It is important to note that *scan element pattern* provides the radar or communications system designer array gain, at the peak of the scanned beam, versus scan angles."

2.2.7 Single & differential technology

By single or single-ended technology one should understand in this thesis the technology of the type of devices that have as an output two unbalanced terminals. An example is a single-ended LNA. In this case a balancing device (balun) is typically needed to avoid a malfunction of the instrument due to presence of unbalanced currents in a symmetric structure, such as a dipole antenna, when it is connected to an unbalanced device.

By differential technology one should understand in this thesis the technology of the type of devices that have as an output two balanced terminals. These terminals should be identical and should be able to support currents of identical magnitude and opposite phase. This type of devices don't require an external balancing mechanism.

2.2.8 Dense & sparse arrays

A dense array it is defined here as the array with spacing between elements small enough so that the physical size of the unit cell imposes an upper limit in its effective aperture. The specific value for this distance will be shown in chapter 5.

A sparse array it is defined here as the array with spacing between elements large enough so that the effective aperture of the unit cell is not constrained by its physical size.

2.2.9 Regular & random arrays

A regular array is the array where the elements are arranged in a regular lattice.

A random array is the array where the elements are placed in the area allocated for the array following a random distribution (random positions). In this thesis irregular arrays are also mentioned. These are arrays where the elements are not arranged in a regular lattice.

2.2.10 Noise temperature

The noise temperature of a radio telescope is a key parameter which limits its sensitivity. Therefore, a whole section is dedicated to explain it (see section 5.3).

2.3 Review of relevant theory

A good summary of general concepts of mutual coupling theory is given in chapter 7 and chapter 8 of the book *Phased Array Antennas*, by R. C. Hansen [12]. In these chapters, the reader can find information about mutual coupling and finite arrays, with its correspondent edge effects. In the context of this thesis the reading of this or an equivalent reference is essential. In chapter 7 of [12] one can find a definition of relevant terms like the scan impedance or minimum scattering antennas and canonical minimum scattering antennas (antennas for which the isolated element pattern is that of the independent antenna). An analytical model for calculating the impedance coupling coefficients between two thin dipoles can be found in chapter 7 of the mentioned book. Spatial-domain and spectral-domain approaches are explained and a brief description to blind angles (angles at which no power is radiated by the array) is given. Chapter 8 of [12] is specifically dedicated to the mutual coupling effects on finite arrays (or infinite-by-finite arrays). This line of work served as inspiration for the work on characterization of edge effects on arrays of printed dipoles which I carried out at the beginning of the thesis [25].

In the aforementioned book of Hansen, various references are given which represent the most relevant studies and the basis of mutual coupling in array antennas. For the matter of this thesis, the work of authors like D. M. Pozar and D. H. Schaubert on e.g. the explanation of scan blindness effects on arrays of printed dipoles [14] is fundamental reading. In [14], a study of infinite phased arrays of printed dipole antennas is presented. A method of moments algorithm is used to calculate the array impedance versus scan angle. There, the coupling from Floquet modes to surface wave modes on the substrate is explained, and how this predicts the occurrence of scan blindness. Measurements from a waveguide simulator of the scan blindness confirm the theory.

D. H. Schaubert has also published several studies on array antenna design and various mutual coupling effects which will be mentioned, when relevant, in this thesis. Specifically, Schaubert has intensively worked on the field of arrays of tapered slot antennas. H. Holter, whose work will be quoted in this thesis, has also contributed.

The work of C. Craeye and M. Arts in [26] has also been used during the preparation of the studies contained in this document. In [26], a rigorous derivation is given

for the receiving cross section of an antenna located in infinite linear and planar arrays.

Several other publications on array antennas theory will be referenced in this thesis.

2.4 Review of relevant tools and technology

2.4.1 Characterization of large finite arrays

Most of the effort in characterization of mutual coupling effects are focused on developing efficient numerical methods. Analyzing and designing large phased array antennas of sizes up to hundreds of wavelengths is a real challenge and a limiting factor in the design of the new generation of radio telescopes. The commercial packages available, based on classical numerical methods such as Method of Moments (MoM) [27], Finite Differences in Time Domain (FDTD) [16], or Finite Element Method (FEM) [17], are limited in the maximum size of the array they can simulate. For the size of radio astronomy instruments such as the SKA, the analysis of an infinite array of elements would be accurate for the central elements, but this requires dismissing the truncation effects [12] and the assumption that the array has a regular configuration of identical elements. In chapter 5, the reader can find a summary of the most important advances on characterization of large arrays.

2.4.2 Prototypes, demonstrators and other instruments

The field of radio astronomy has recently being demanding phased array antennas capable of scanning the sky over a wide range of angles in a large bandwidth (up to $\sim$ 7:1 in the case of the arrays designed in this thesis). But it is not only radio astronomy that needs such instruments; civil and military applications, such as radars, also demand wide bandwidths. Radio astronomy applications, however, require large collecting areas and typically have low budgets, so that the antennas must also be carefully designed to minimize the cost. The design of phased array antennas therefore, especially in the field of radio astronomy, has been very active in the past 10 years. Lately, the Aperture Arrays [9] are becoming very popular. These are phased antenna arrays composed of millions of elements which are used to sample the incoming wavefront directly. The most important design goal in a unit cell of instruments like these is to have a smoothly-varying impedance in which extreme values are limited within an acceptable range, and free from anomalies across the band for all scanning angles. This will lead to acceptable matching with the low noise amplifier, and will help to obtain a low noise figure. It is also important to aim for low losses in the structure by removing as many lossy elements as possible. Finally,

the effective aperture and beamwidths should be as large as possible in order to scan the desired portion of the sky. Large 3 dB beamwidths, free of anomalies, allow the application of different beamforming schemes which will determine, amongst other things, the side-lobe pattern.

There are several "new generation" radio telescope designs for low-frequency radio astronomy (below $\sim$ 300 MHz) based on phased array antennas. Some examples are LOFAR (LOw Frequency ARray) [22], which in phase one consists geographically of a compact core area and 45 remote stations. Each of the remote stations will be equipped with 100 "high band" antennas (a composite system consisting of 4x4 dual-polarization dipoles and a dual-polarization RF beam former working from 110 to 250 MHz) and 100 "low band" antennas (electrically small, thin dipoles which are optimized for the 30-80 MHz range and can be used for zenith angles less than 60 degrees). The MWA (Murchison Widefield Array) [28] is a 500-antenna element instrument. Each MWA antenna element consists of 16 dual-polarization active dipoles, with analog beam former and electronic steerability, giving a total of 8,000 dipoles and $\sim$ 8,000 m^2 of collecting area at 150 MHz. It will cover the 80-300 MHz band with a wide field-of-view. The LWA (Long Wavelength Array) [29] will be a low-frequency radio telescope designed to produce high-sensitivity. This will be accomplished with large collecting area (approaching 1 square kilometre at its lowest frequencies) spread over an interferometer array with baselines up to at least 400 km. The SKA-AAlo will follow these instruments in about 2020 and will be the next big step in low-frequency radio astronomy. The BLU antenna (Bow-tie Low-frequency Ultra-wideband antenna) is a single-polarization prototype presented in this thesis as a candidate antenna for the SKA-AAlo (see Fig. 2.3).

(a) LOFAR "low band" antenna (b) LOFAR "high band" antenna

Figure 2.1: LOFAR antennas.

Figure 2.2: MWA tile.

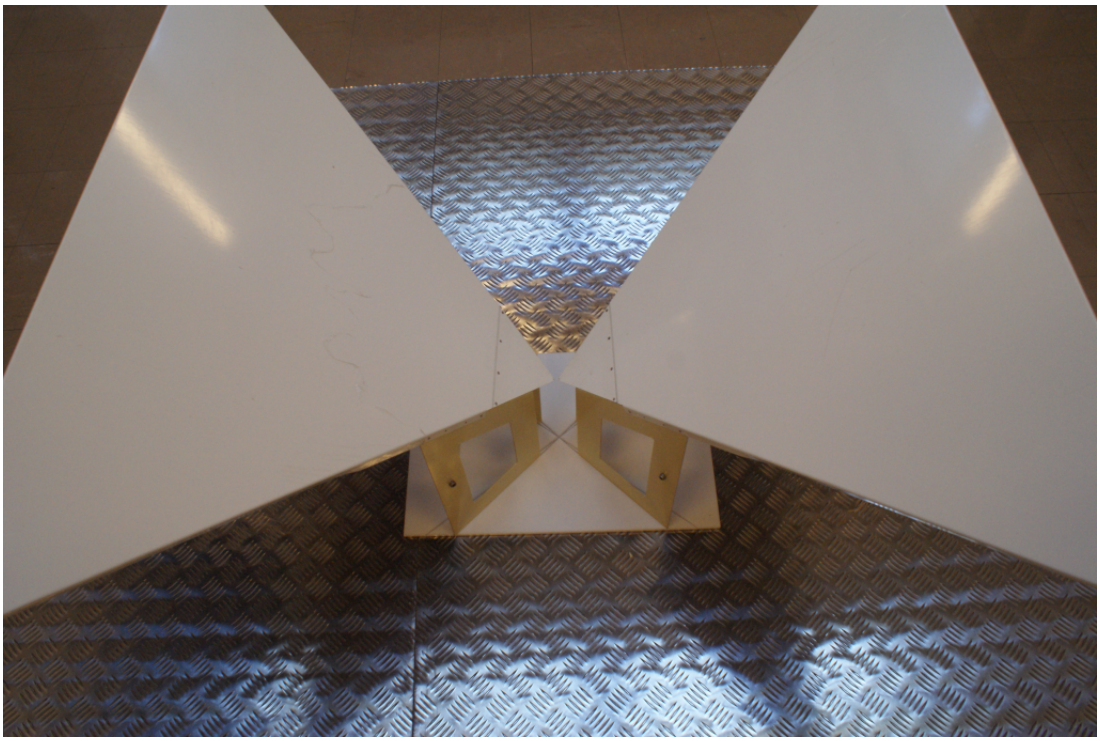

Figure 2.3: The BLU antenna.

At higher frequencies dense regular arrays are of special interest in order to provide a fixed effective aperture across the band, wider beams that result in faster survey speeds and easier beamforming, and absence of grating lobes. Tapered slot antennas, as described in chapter 3 and chapter 4, have been frequently used in these type of array and there are several designs that have been published in recent years which are relevant for radio astronomy applications [21, 30, 31, 32, 33]. Many

different antenna elements have also been used to form these dense regular ultra-wideband arrays, like the body-of-revolution elements of Holter [34] or the patches in [35].

The contributions to dense regular arrays for radio astronomy of this thesis follow the developments started on the late nineties in the Netherlands Institute for Radio Astronomy (ASTRON) with the THousand Element Array (THEA) [36] and continued with the Electronic Multi-Beam Radio Astronomy ConcEpt (EMBRACE) [23] and the Vivaldi ALuminium ARRaY (VALARRY) [31]. The Foil-based LOW-cost PAcman Differential Dual polarized Demonstrator (FLOWPAD^3) and the FG-IGN Differential Active Antenna Array (FIDA^3) are prototypes described in this thesis. In Table 2.1 the main differences with previous prototypes are described, and in Figs. 2.4 to 2.7 the tiles are presented. Other demonstrators, like the 2 Polarizations All Digital array (2-PAD), are being developed in different universities and research centres around the world. 2-PAD is a European effort, led by the UK to build a dual-polarization, all-digital phased-array. The system will consist of two-fully operational tiles plus ten dummy tiles to compensate for edge effects. 2-PAD tiles will be system compatible with EMBRACE, and will use the FLOWPAD^3 front-end for its initial tests. More information about 2-PAD is given on the SKADS website [37]. The next chapter is dedicated to explain the design of a differentially-fed low-cost array antenna which led to the construction of FLOWPAD^3.

Table 2.1: Relevant characteristics of some dense regular array prototypes for radio astronomy

	EMBRACE	VALARRY	FLOWPAD^3	FIDA^3
Technology	Single	Single	Differential	Differential
Polarization	Single	Dual	Dual	Dual
Fabrication issues	- Feeding board needed - Substrate needed	- Feeding board needed	- Bridge needed	
Frequency band	300 - 1500 MHz (-45^{o}to 45^{o}scan)	600 - 1500 MHz (limited scan)	300 - 1000 MHz (-45^{o}to 45^{o}scan)	300 - 1000 MHz (-45^{o}to 45^{o}scan)
LNAs/m^2	128	128	77.7	70.8

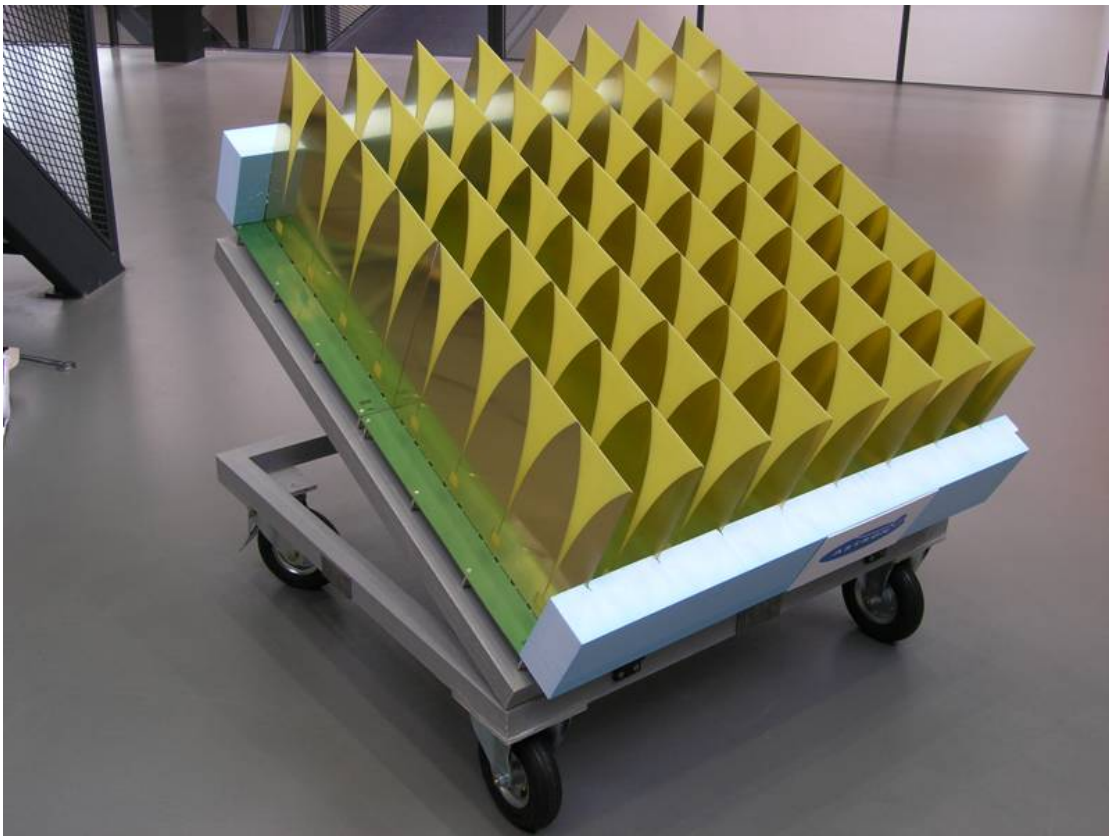

Figure 2.4: EMBRACE tile.

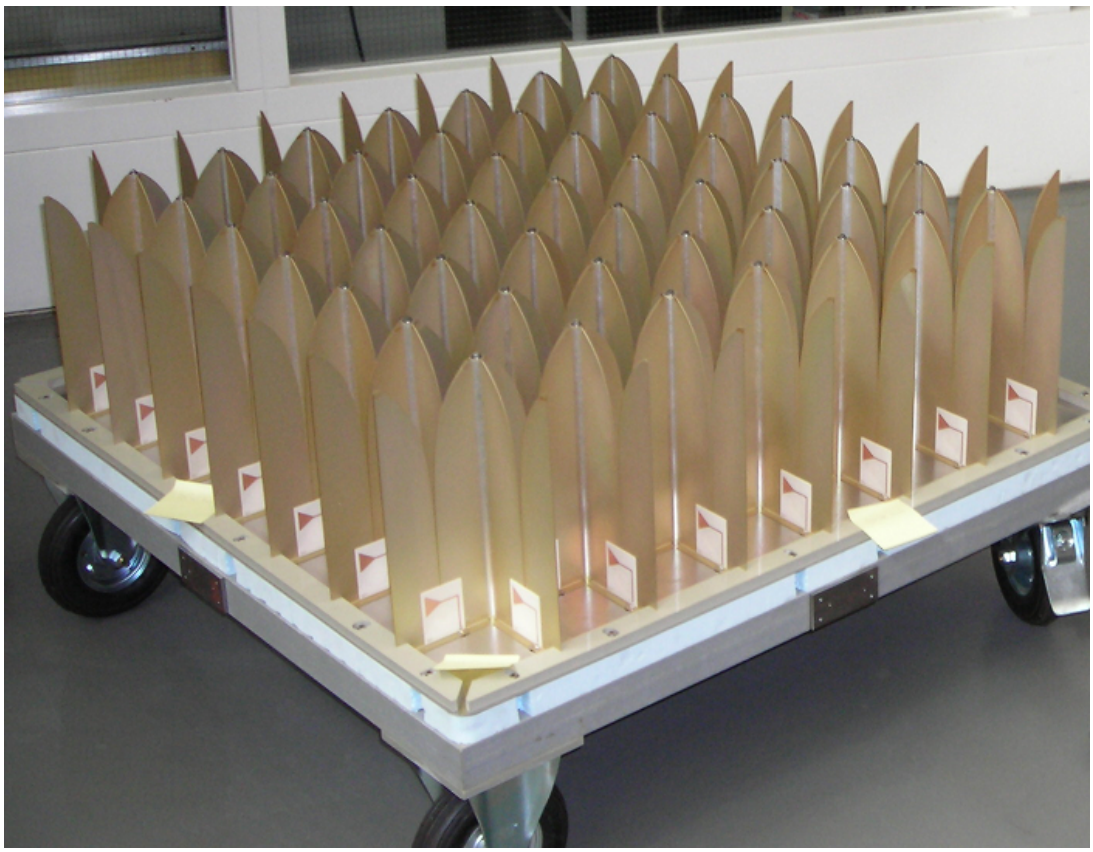

Figure 2.5: VALARRY tile.

Figure 2.6: FLOWPAD^3 tile.

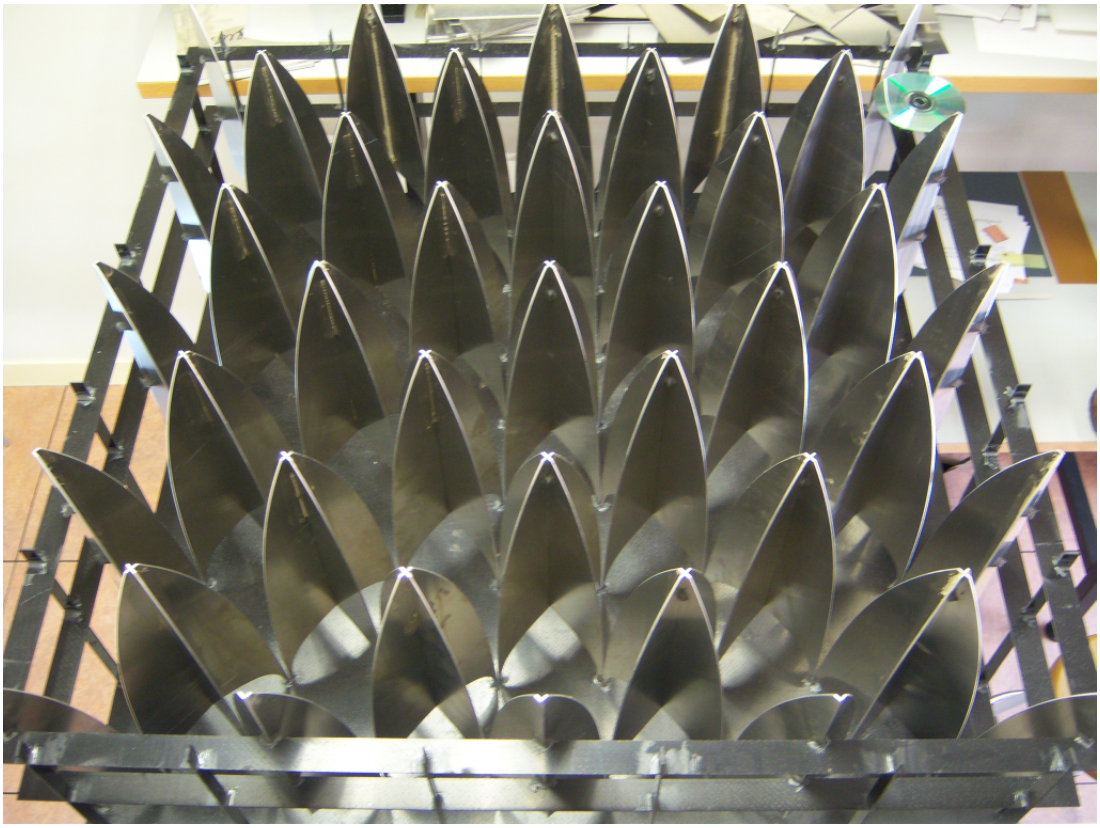

Figure 2.7: FIDA^3 tile.

Chapter 3

On the Design and Optimization of Low Cost Ultra-Wideband Tapered Slot Antenna Arrays

Low-cost antennas are a key factor in the success of new radio telescopes of the size of the SKA. The frequency band from 300 MHz to 1 GHz is planned to be covered in the SKA with a dense Aperture Array [9, 38]. This, so-called mid-frequency band array, will have about 20,000,000 antennas per polarization. This is assuming 250 stations of 56 m of diameter each, as stated in [8]. The cost of this array is estimated to be 25% of the total cost of the SKA [8] and the cost of the antennas is estimated to be approximately 25% of the cost of the SKA-AAhi as described in [39]. The chart of Fig. 3.1 shows the cost for a SKA-AAhi station with analogue beamforming. As the choice of digital or analogue beamforming does not affect the antenna layer, one can see that for 250 stations the cost of the antennas for the SKA-AAhi array is remarkable. With the tight budgets available for radio astronomy projects, the choice of very low-cost materials and antenna designs is a necessary condition for the achievement of the desired capabilities of the SKA.

FLOWPAD^3 (Foil-based LOW-cost PAcman Differential Dual-polarized Demonstrator) is a demonstration array to show innovative technologies which were studied during the PACMAN (Phased Array Communication Antennas for Mass-Market Application Needs) [40] and the SKADS projects [37] in the Netherlands Institute for Radio Astronomy (ASTRON). The demonstrated technologies focus on the reduction of the cost of the antenna tile with differential feeding using printed manufacturing technology, the aim of which is a high performance and low-cost antenna. The antenna pitch (width of the antenna) is chosen to be sufficiently big to allow a reduction of the number of LNAs per square metre, while maintaining a sufficiently large effective area. Initially, this pitch was set to 176 mm ($= \lambda/2$ @ 850 MHz) which

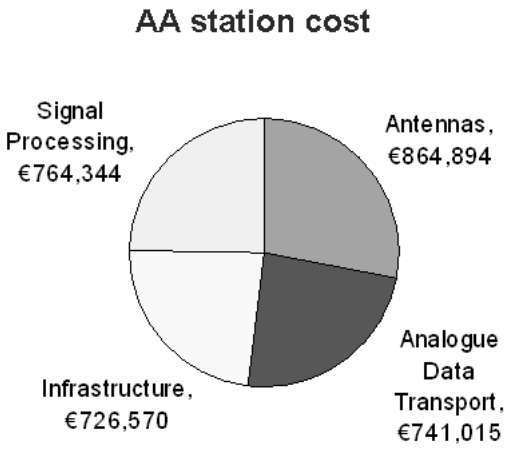

Figure 3.1: Cost of an AA-hi station extracted from [39].

is larger than the 125 mm of EMBRACE [23]. Furthermore, the use of cheap materials, cheap printing technology, and cheap antenna element designs will also help to reduce the cost of the final prototype and, in the future, the cost of SKA. In order to reduce the cost of materials and elements, the strategy is to use differentially-fed Vivaldi antennas printed over a very thin foil (polyester, kapton), which has not been realized before. These foils are placed into a cheap foam structure in order to keep the printed antennas straight and give to the array the desired lattice (see Fig. 3.2). In this chapter I present the results of the design process based on infinite array simulations and the measurements of the differentially-fed prototype tile carried out during and after a 4 months internship in ASTRON. As a result of the work presented in this chapter, a prototype was built and measured and it is now part of the FLOTT project (FlowPAD Towards TwoPAD), a larger implementation of ASTRON's FLOWPAD^3 array for testing of the SKADS demonstrator 2-PAD. Another prototype for SKADS, FIDA^3, is in line with the designs explained in this chapter and utilizes differential technology as well. As it will be shown in chapter 4, FIDA^3, as FLOWPAD^3, fulfils the requirements of the SKA.

The contents of this chapter have been published or made public in one technical report for the SKADS project [41], two contributions to workshops [42, 43] and two conference proceedings [44, 45].

3.1 Introduction

The use of differentially-fed elements, such as differentially-fed tapered slot antennas, as explained in chapter 4, brings numerous advantages when ultra-wideband performance at low-cost is desired. The absence of a balun, otherwise needed for

Figure 3.2: Array tile made of foam and polyester elements.

single-ended technology, not only reduces the cost and the losses of the system, and therefore the overall system noise, but also allows one to directly connect differential LNAs (DLNAs) and favours wider bandwitdhs otherwise limited by the balun. Furthermore, in the present design, cheap materials are used. The main properties of these materials were measured; the foam, polypropylene (EPP) has an average $\varepsilon_r = 1.24$ and dielectric loss tangent of 0.01 and the polyester has $\varepsilon_r = 3.1$ and dielectric loss tangent of 0.0096. One of the main purposes of the present design is to prove that these materials can be used while preserving the electromagnetic properties of an array free of dielectric and foam.

The differential solution here is therefore realized on polyester foil (see Fig. 3.3). As described in [45], the foil is produced in two steps; first a silver ink layer is screen printed on the foil and on this layer an electrolytic process grows a copper layer. The production rate is 100 metres of foil per hour. To provide conductivity between antenna rows, metallic clips are used, connecting the top and bottom of the antenna. The production cost of the antenna is approximately 0.75 € per antenna. This is significantly lower than the cost of other realizations, like low-loss Printed Circuit Board (PCB) antennas or any design which requires a feeding board [23, 31], which is typically equal to the cost of the rest of the antenna. Including foam and clips, a cost of less than 2 € per antenna can be achieved with the present design.

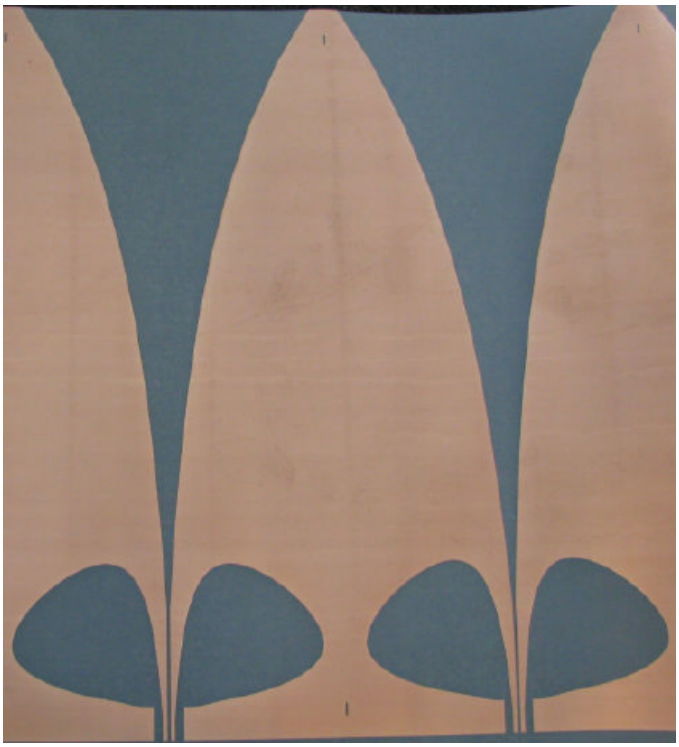

Figure 3.3: Copper plated polyester foil antenna. Picture extracted from [44].

In order to achieve the differential feed, an equivalent scheme to that of the standard microstrip to slotline transition [32] is used. The comparison with the current design is shown in Fig. 3.4. The output feeding line is now a CPS (Coplanar Strips Line) transformed from a CCWG (Coupled Coplanar Waveguides) transformed from a slotline which feeds the aperture. Note that previous designs like VALARRY [31] or EMBRACE [23] used a microstrip line as output feed line. In order to close the current path, the 2 cavities at both sides of the differential line are connected by means of a metallic wire or strip (see Fig. 3.5). This feeding system represents a novel design and has been patented by Rob Maaskant, ASTRON [46]. One of my objectives during the internship period at ASTRON was to optimize the design of this integrated feeding system. Note that the technology transformation from the slotline to the differential CPS line is regarded in the same layer as the antenna and only one thin layer of substrate is needed for supporting purposes.

The specifications of the FLOWPAD^3 project are summarized in Table 3.1.

As I mentioned before, in this chapter the design of an infinite TSA array as a potential candidate for the middle frequency band of the SKA is presented. The main focus is the use of low-cost differential technology. First single TSA elements will be studied in order to analyze the necessity of making simulations including the polyester and the foam, as they add complexity to the computer model. Then, in section 3.3, the design and optimization of a transition between differential technologies is explained. These technologies are the slotline which forms the antenna

and the CPS line which connects to the DLNA. Starting from this transition, a TSA element is created and simulated in an infinite array environment in section 3.4. Finally, the measured performance of a finite tile of antennas like the ones designed in section 3.4 is presented in section 3.5, where the measurement process is also described. The conclusions and future lines of work can be found in section 3.6.

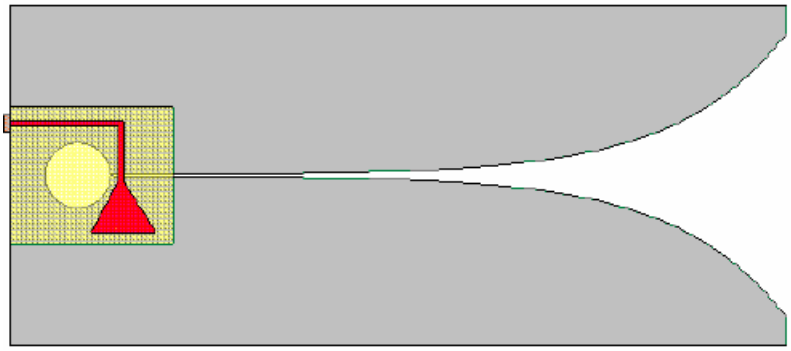

(a) Vivaldi antenna with standard microstrip line feed

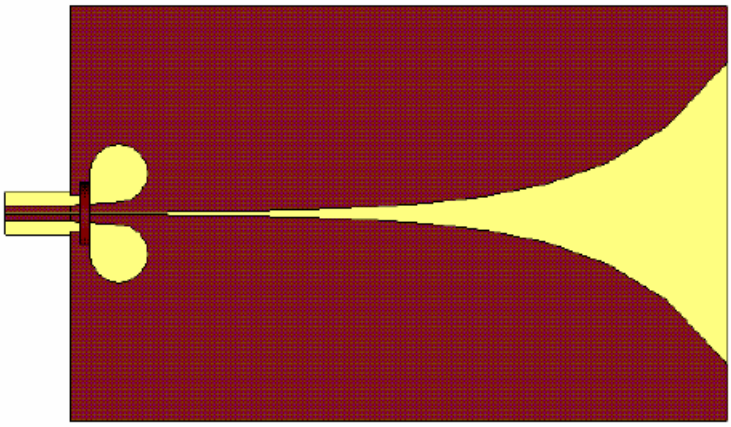

(b) Vivaldi antenna with novel differential feed

Figure 3.4: Realizations of the feeding line.

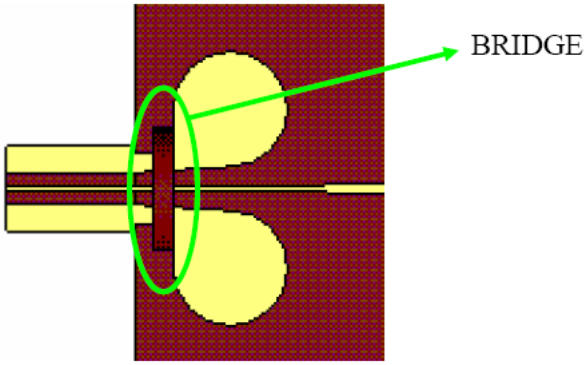

Figure 3.5: Feeding of the Vivaldi antenna.

Table 3.1: FLOWPAD[3] specifications.

Property	Value	Note
Antenna	Vivaldi type with differential feeding.	Not been realized before. Potentially cheaper. Potentially better compared to single-ended with respect to loss in antenna feed network.
Polarization	Dual polarization.	SKADS benchmark design.
Frequency band	300-1000 MHz.	SKADS benchmark design.
Antenna pitch	176 mm (= $\lambda/2$@ 850 MHz).	Modified SKADS benchmark design (from 800 to 850 MHz). Enables max 1000 MHz freq. Or as big as possible.
Tile	Partially active; functional: LNAs only.	To enable measuring of antenna and T_{sys} performance.
Tile size	8x8 (32 per polarization). See Fig. 3.2.	Related to beam forming: 4:1.
Beamformer	Optional; no steering.	Demonstrated by EMBRACE.
T_{sys}	35 K.	System = antenna + LNA.
Expected LNA gain	COTS LNA: 18 dB. Custom1 LNA: 20-30 dB. Custom2 LNA: reduced slope.	
Power match vs noise match	Noise match to Γ_{act} @ broadside.	Noise coupling issue.
Active impedance	150 Ω.	High for ultra-wideband performance.
Output	Single.	Balun included in LNA board.
Supply	Via RF coax.	Cost / crosstalk / oscillation.

3.2 Single elements: the effect of the foam and the foil

The aim is to design and optimize the performance of an array of differentially-fed TSAs. As explained in chapter 6, the electromagnetic simulation of finite arrays of the size of a SKA station is rather complex. Infinite array simulations are therefore used and typically they accurately represent the behaviour of most of the elements in the array except for those close to the edge [12]. Even for an infinite array simulation, the presence of dielectric materials, such as the polyester or the polypropylene rapidly increase the computation time. It is in the interest of a fast design process, where limited computing resources are available, to consider the possibility of excluding these elements from the simulation, once it is shown that their electromagnetic effect is minimal. The first step was therefore to build several models in order to check how accurate were the electromagnetic simulations (HFSS software [17]) for this kind of differentially-fed antenna elements and what was the actual effect of the foam and the foil.

The first model built (see Fig. 3.6) was a single Vivaldi element where a balun, comprising of a microstrip to CPS transition, was attached at the feeding point of the element in order to balance the current for measurement purposes. The copper layer was printed on a 0.1 mm thick polyester layer. The balun was calibrated for the measurement. The reference impedance for the calculation of the S_{11} parameter was 100 Ω.

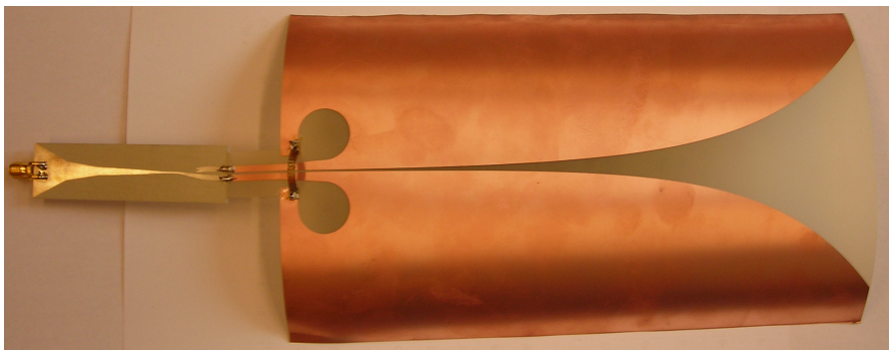

Figure 3.6: Differentially-fed Vivaldi element with wideband balun.

The results shown in Fig. 3.7 are not expected to be good in terms of reflection coefficient, as the present antenna was mechanically adapted from previous models. From these results we can conclude that the effect of the polyester foil in the single antenna impedance is weak. Also, the simulations show a reasonably good agreement with the measurement.

The second model was a single unit cell that consisted of two elements of orthogonal polarizations (see Fig. 3.8). In this case the entire unit cell including the

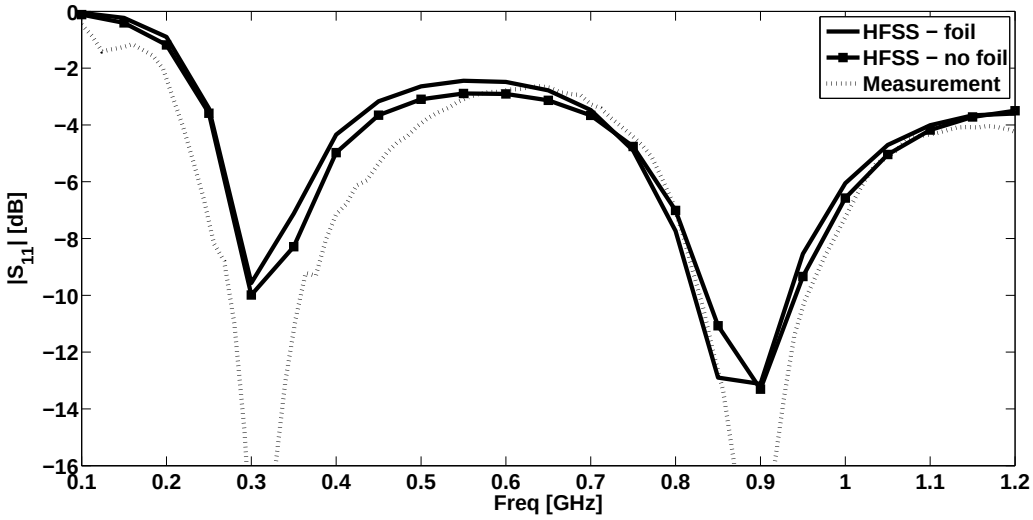

(a) Magnitude

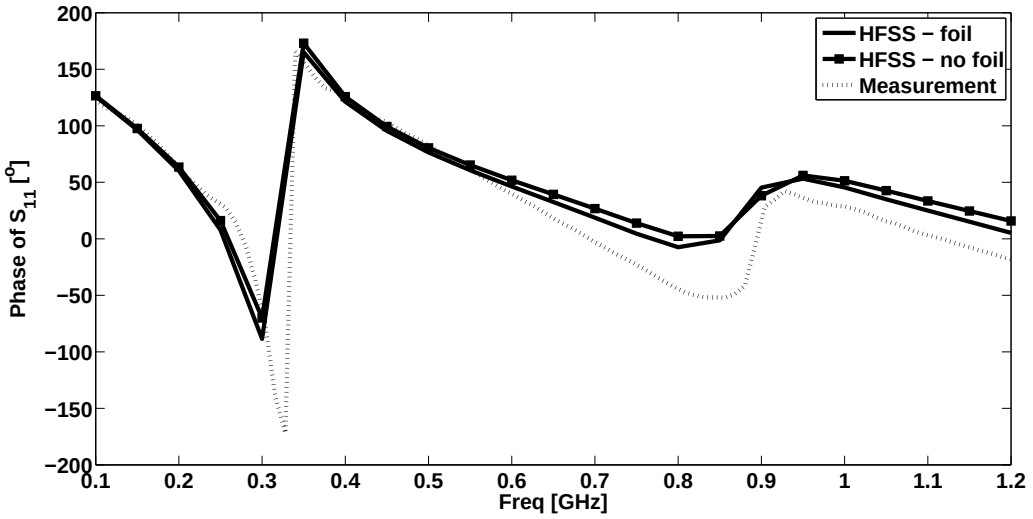

(b) Phase

Figure 3.7: S_{11} for a single differentially-fed Vivaldi element.

foam, the polyester foil and the two orthogonal elements were simulated. The balun was attached to both elements in order to measure the full S-matrix. The results for the comparison between simulation and measurement and the effect of the foam and foil are shown in Fig. 3.9 and Fig. 3.10.

Simulations and measurements show a good agreement. The foam has little effect in terms of impedance matching due to its very low permittivity ($\varepsilon_r = 1.24$). The effect of the foam in terms of radiation efficiency must however be analyzed as it will have an effect on the system temperature (see chapter 4). The foam, as also the polyester, are only useful for supporting purposes and they must be removed from the structure as much as possible in order to reduce losses and cost. Again, the effect of the polyester on the impedance is minimal.

Finally, a third model was built to check the simulation software for a slightly

larger structure. It was a 3-element linear array (see Fig. 3.11). In this case the balun was attached to the central element in order to measure the S_{22}. The side elements were therefore matched to 100 Ω loads. The results of Fig. 3.12 show again a good agreement between simulation and measurement.

Once the single elements were studied, a transition between different transmission line technologies, necessary in order to connect the antennas and the DLNAs, was optimized for the present application. This transition led into a TSA element which was simulated in an infinite array environment.

Figure 3.8: Single unit cell with balun in both elements.

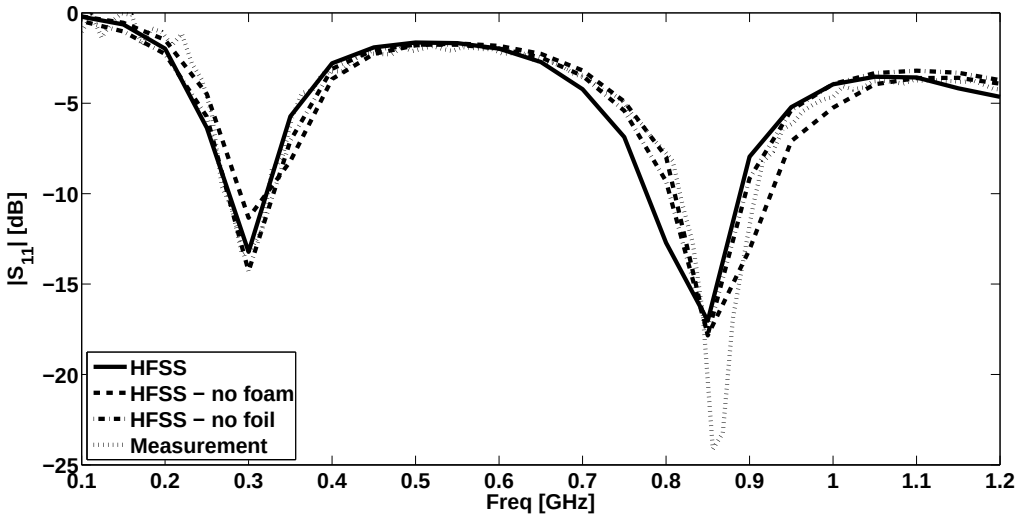

(a) Magnitude

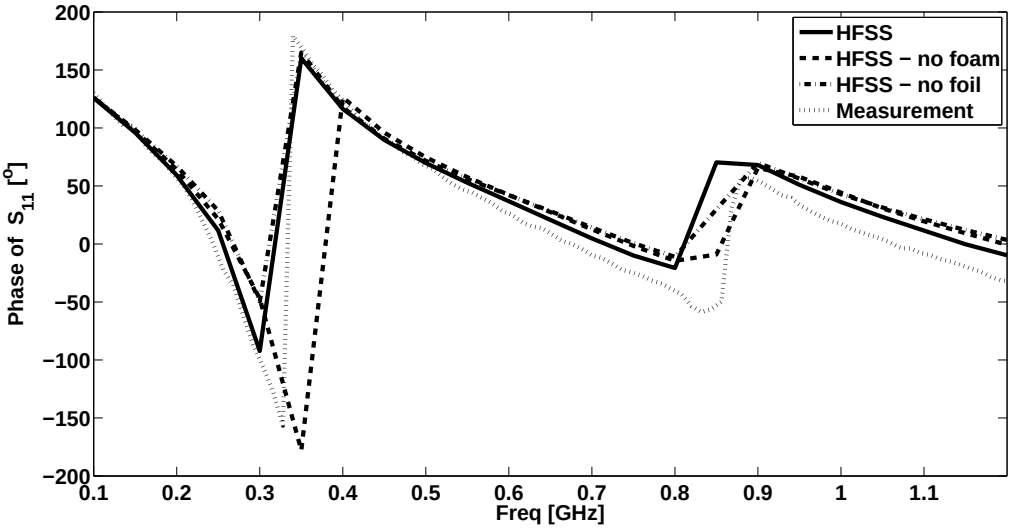

(b) Phase

Figure 3.9: S_{11} (one of the elements of the single unit cell).

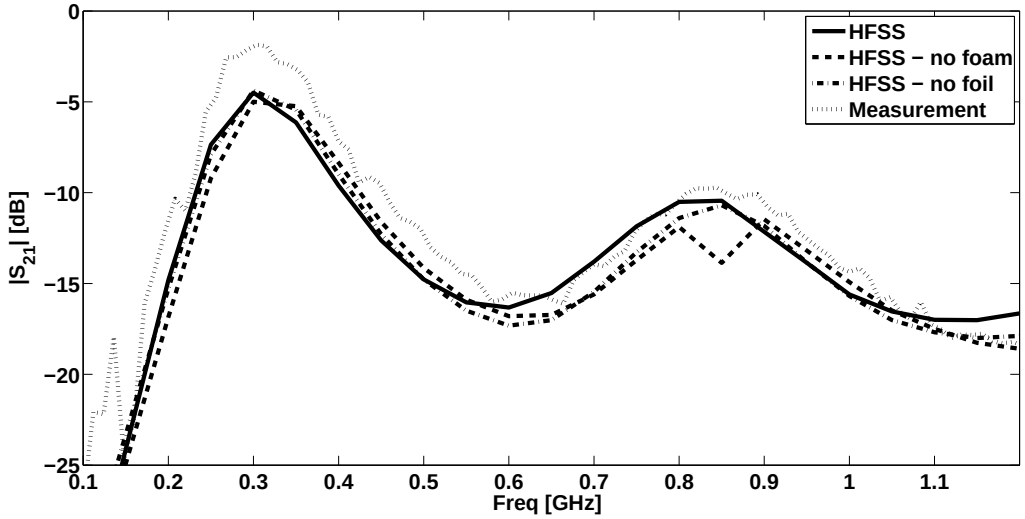

(a) Magnitude

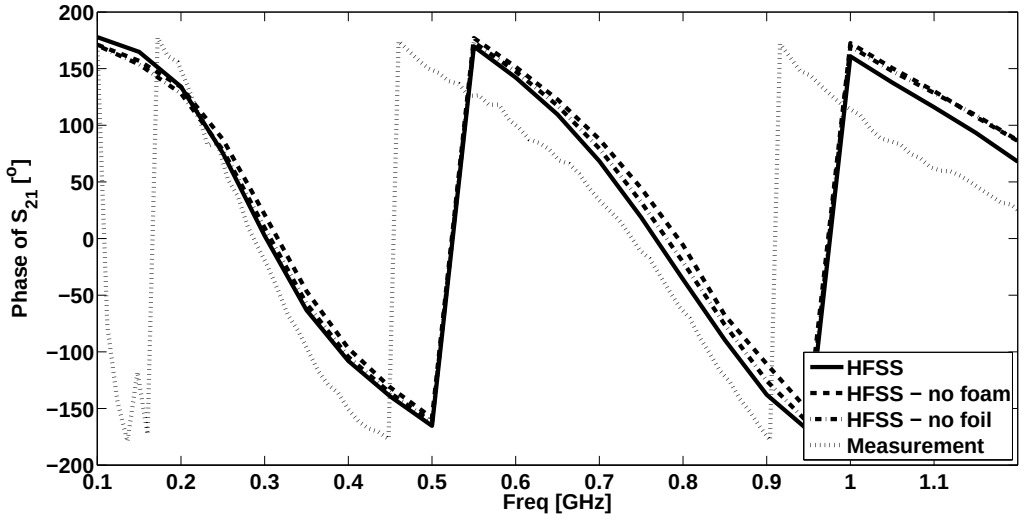

(b) Phase

Figure 3.10: S_{21} (coupling between the elements of the single unit cell).

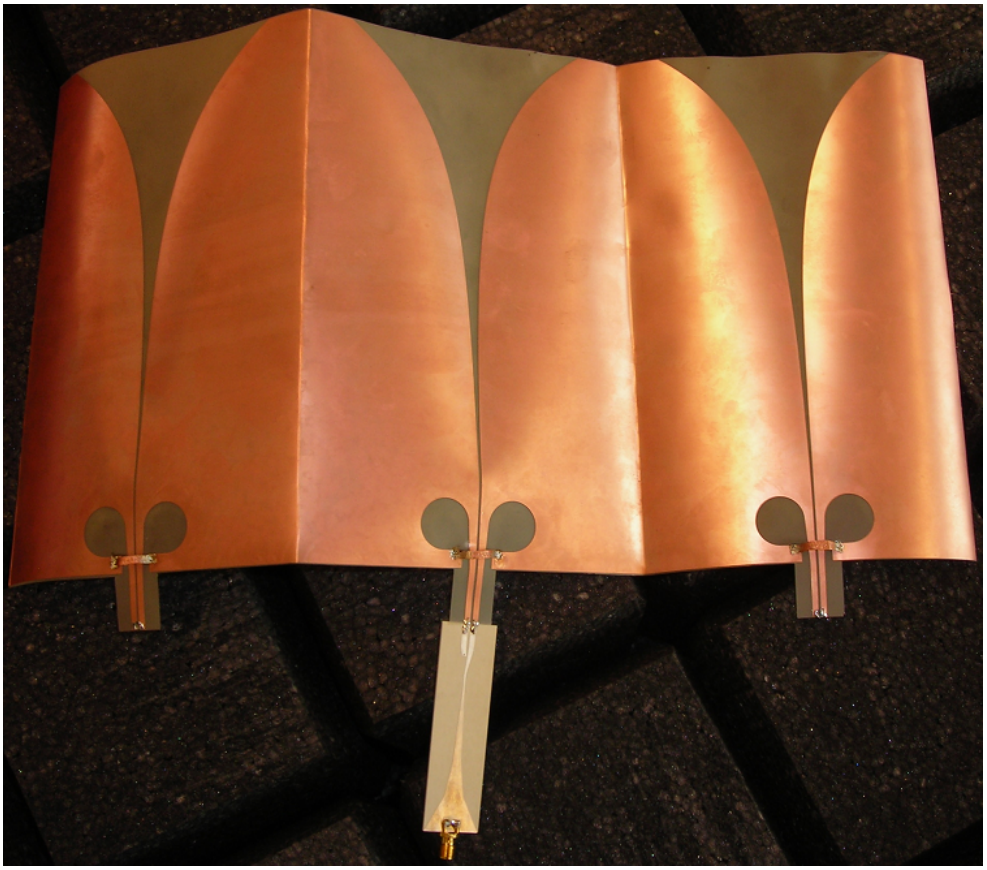

Figure 3.11: Central embedded element in a 3x1 array of differentially-fed Vivaldi elements.

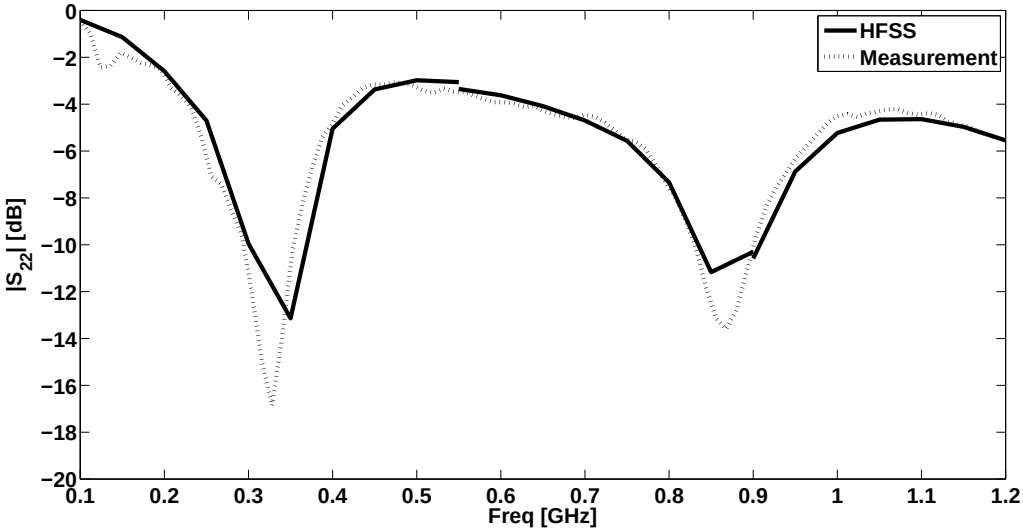

(a) Magnitude

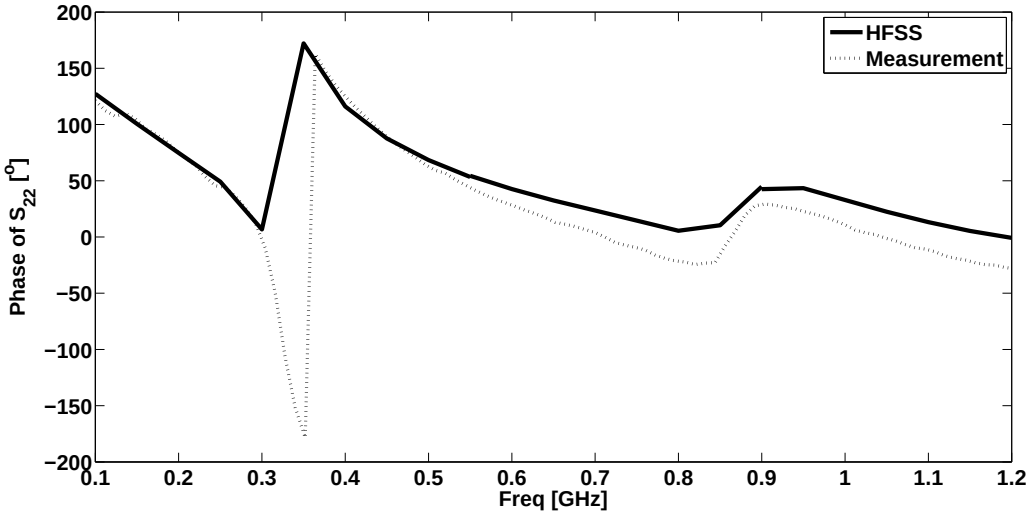

(b) Phase

Figure 3.12: S_{22} (central Vivaldi element of a 3x1 array).

3.3 Transition CPS line to slotline

3.3.1 Dielectric-free transition from a CPS line to a slotline

As explained before, the proposed transition could be regarded a one-layer version of the standard transition microstrip to slotline transition [47]. The circular slot cavity in [47], which forced an open circuit at the crossing point to push the field into the microstrip line, has now been substituted by two cavities, which perform the same task. The field from the slotline is pushed into the CPS line through a short CCWG line. A wire or strip connects both external sides of the CCWG line in order to close the current path and to assure that there is no a potential difference between them. This will frequently be referred as the bridge connection. This connection is

necessary in order to preserve a balanced differential-mode as explained by Gupta et al. [48] (see Fig. 3.13).

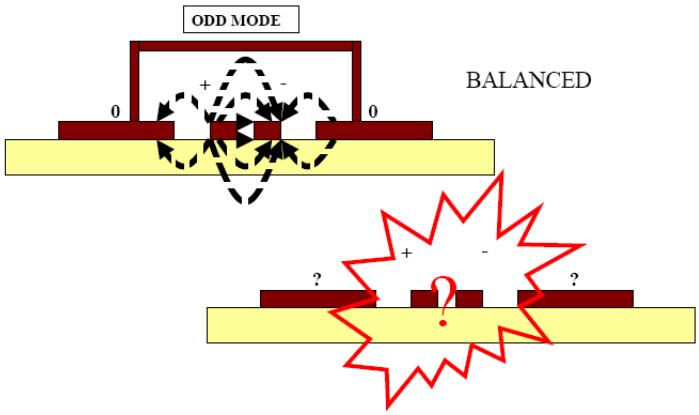

Figure 3.13: Differential-mode of the field for a bridge connection.

Fig. 3.14 shows a bridge connection made with a strip line on the DLNA board, which may decrease the cost compared to the use of a metallic bridge. In this case two metallic vias are needed in order to connect the strip to the side conductors of the differential line.

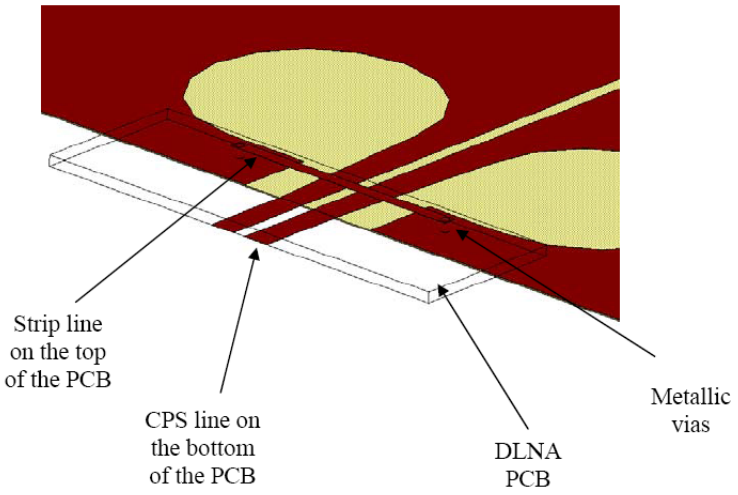

Figure 3.14: Connection of cavities realized with a Strip line printed on the DLNA board.

3.3.2 Tuning process

The first step taken in the design of the dual-polarized array was to tune the physical dimensions of the Back-to-Back (B2B) model of the transition from the feeding line to the tapered slot (Vivaldi antenna). The tapered slot antenna would be then attached to the transition and a new optimization process would take place for the infinite array model. The pitch of the B2B corresponds to the antenna pitch (176 mm, which was the original target of the design).

There are several parameters that may be tuned to find the optimum performance of the B2B, such as the positions of the cavities, which affect the tapering of the transition, the cavity radius, which affects not only the size of the cavity but also the tapering of the transition, and the slot width, which affects the impedance matching through the modification of the characteristic impedance of the line.

In order to find an optimum solution, a fully-parametrized model of the antenna and the B2B in HFSS were made, allowing modifications of several dimensions of the model in a simple way. The smart optimization process used was based on doing a series of simulations where the cavity shape, its size, and its position could be modified independently through 5 points joined by curved lines defining the contours of the twin cavities, aiming for the best performance in terms of S-parameters. It was observed that the size and tapering of the transition were important in the B2B performance. The tapering of the transition is defined by the dashed line marked in Fig. 3.15. Furthermore by placing the cavity in a different position, the tapering is changed as well as the effective propagation length for the electric current around the cavity. The size of the cavity and the tapering of the line can be independently modified by changing point 2 or 1 in Fig. 3.15.

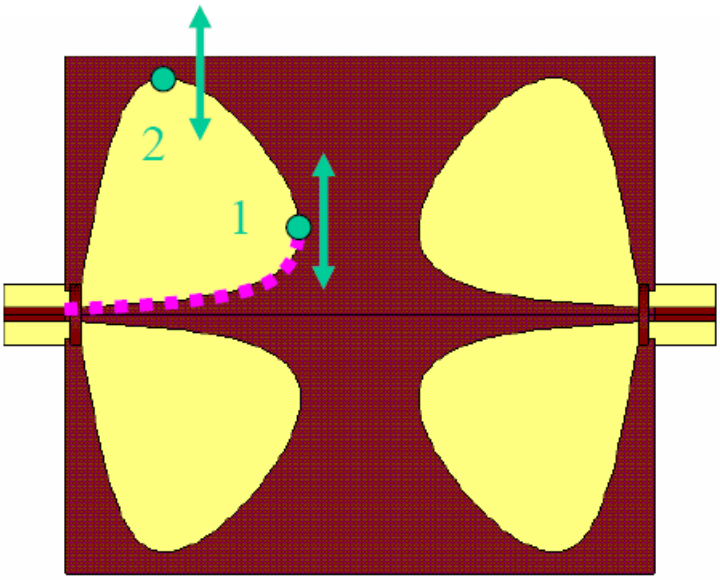

Figure 3.15: B2B model of the transition.

A parametric simulation was carried out in where these two points were allowed to move freely on the plane of the B2B. As it could be expected, larger cavities improve the results at lower frequencies and an optimal smooth tapering for the line was found for a desired 150 Ω input impedance. The measured results are shown in Fig. 3.17.

3.3.3 Measurement results

A model of the B2B was printed on a very thin layer of kapton. This material is supposed to have as little effect as the polyester and can be regarded as air dielectric in the analysis. In Fig. 3.16 we can see the B2B model and the two baluns that are needed to measure the differentially-fed B2B board in a similar way as in the case of the single element measurements explained before. The effect of the baluns was calibrated in the measurement.

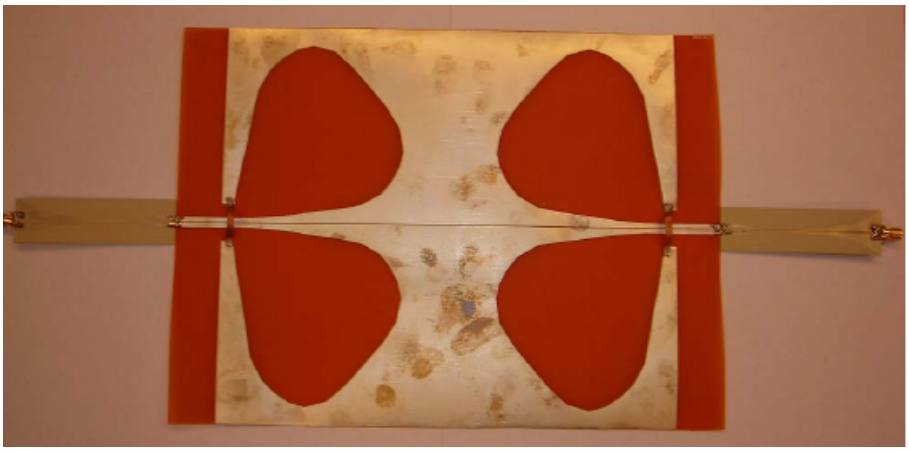

Figure 3.16: B2B model built.

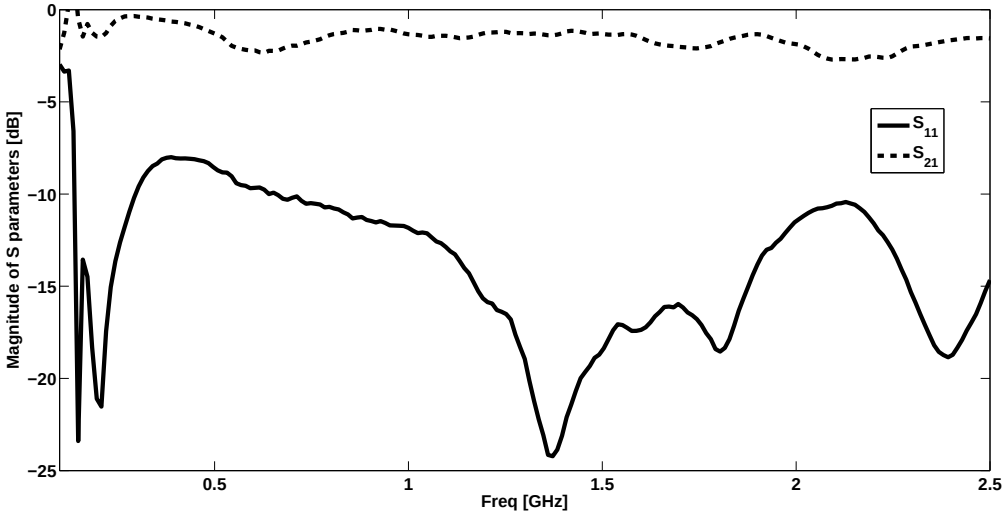

Figure 3.17: B2B measurement.

The measured performance presented in Fig. 3.17 shows that the average radiation loss up to 1 GHz is of about 1.5 dB in the B2B configuration and 0.75 dB in the case of a single transition. This is still quite high for a radio astronomy application such as the SKA, but good enough to prove the differential feeding concept.

3.3.4 Conclusions

The size and the tapering of the CPS to slotline transition have been identified as being key parameters of the transition. The cavity must have the right shape so that the tapering between the CPS and the slotline is optimum (e.g. the presence of straight parallel lines may cause losses in the form of undesired radiation). A model with an average insertion loss of 0.75 dB (radiation losses) was built, which is similar to the B2B performance as measured for the VALARRAY design [31].

Having optimized the isolated transition, I now extend it into a TSA element and immerse it into an infinite array in order to design the SKA-like array.

3.4 Infinite array simulations

The next step was to carry out simulations of an infinite-by-infinite dual-polarized array in order to check the effect of the bridge, the ground plane and the transition. Also, I optimized the infinite array performance at broadside and analyzed and optimized the scanning capabilities of the array.

3.4.1 Selection of unit cell

The simulations I carried out did not include foam or polyester in the unit cell. This was allowable as they have been shown to have negligible effect in terms of impedance matching. This reduced the simulation time. The reference element used for the simulations is shown in Fig. 3.18. The antenna is realized by adding to the optimized transition an exponential taper to form the receiving aperture. The tapering follows equation 3.1.

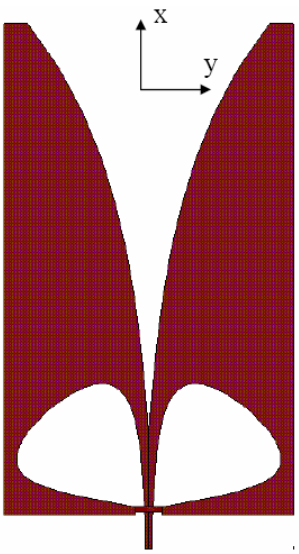

Figure 3.18: Reference model for the simulations.

$$y = A \cdot e^{B \cdot x} + C \tag{3.1}$$

The first step was to select the unit cell to be simulated. In Figs. 3.19(a) and 3.19(b) one can see two different 3D views of the unit cell. The first as it was simulated, without the presence of the foam or the dielectric, and the second with both of them (the foam is shown as a transparent box). This unit cell contains the smallest periodic portion of the infinite array, including the connection between different rows of antennas.

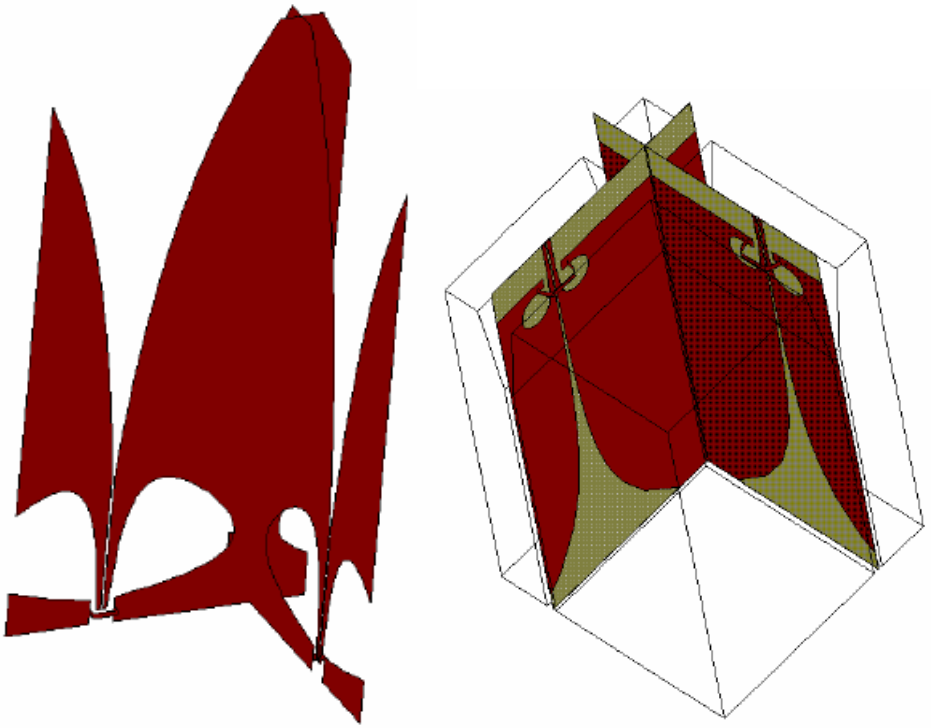

(a) Without foam and dielectric (b) With foam and dielectric

Figure 3.19: View of the unit cell.

It is known from other studies (e.g. see chapter 4) that the bandwidth is proportional to the ratio of the antenna length to its pitch, but of course, when the aim is to reduce the number of LNAs per square metre, increasing the length would increase the final cost. As the bandwidth is a key parameter of the specifications, the antenna length was chosen to be as close as possible to the maximum allowed by the construction process, but leaving some space for bending the substrate at the bottom of the antenna where the DLNA is connected. The length is set to 37.2 cm. (MECO construction process [49]: current maximum was 38 cm). It is also know from previous studies (e.g. see chapter 4 and [32]) that a more linear antenna tapering means higher minimum operational frequency, but also smaller humps in the VSWR. Some important parameters chosen for the reference element are shown in Table 3.2.

Table 3.2: Initial geometrical parameters of the array.

Total length	*A*	*B*	Rest of parameters
372 mm	5 mm	0.00802 mm^{-1}	From the B2B optimization

3.4.2 Optimum pitch of the antenna

I aimed to achieve a bandwidth from 0.3 to 1 GHz for broadside scan as mentioned in the specifications. Once the length of the antenna had been fixed to its current maximum possible value, I needed to determine the maximum pitch of the antenna which would allow a 3.3:1 bandwitdh. Both the opening rate of the tapering (parameter B) and size of the antenna aperture are simultaneously changed so that the degree of tapering for the exponential profile remains similar. Note that in this case a ground plane is used instead of the bridge. As shown in Fig. 3.20 the highest operational frequency is reduced about 90 - 100 MHz for every 10 mm increase in the pitch for a fixed length. The results are promising, as it can be seen the frequency band ranges from 0.257 to 1.071 GHz (VSWR<2) for a 175 mm pitch. The initial requirements have already been fulfilled at this point.

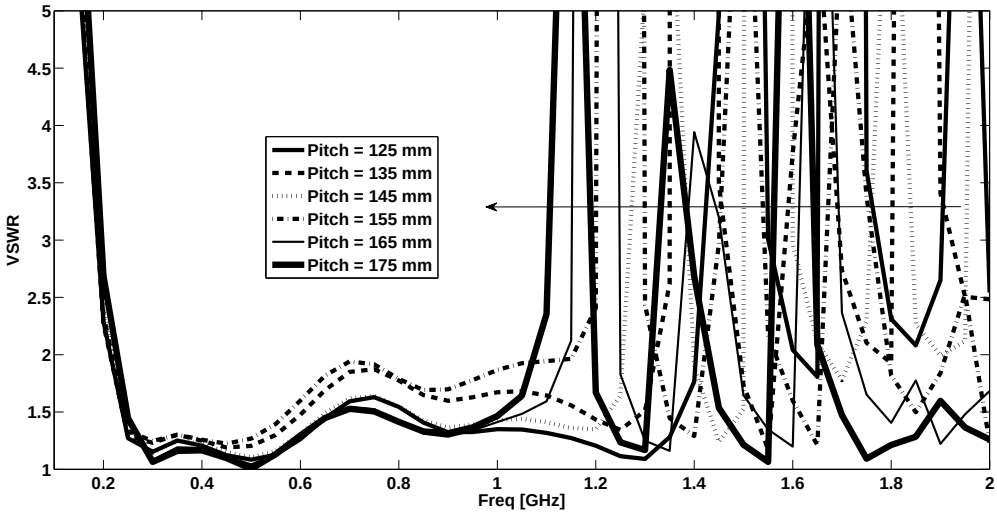

Figure 3.20: Effect of the pitch on the active VSWR at broadside for an infinite dual-polarized array.

3.4.3 Effect of the ground plane

The effect of using a ground plane instead of a bridge to create the appropriate connection between the fins of each antenna element (see Fig. 3.21) is analyzed here. By using a bridge, the price and complexity of the model is assumed to decrease, since one does not need to process a metallic ground plane (if the radome can support the antennas), drill holes in it, attach it to the antennas, etc. Because Vivaldi

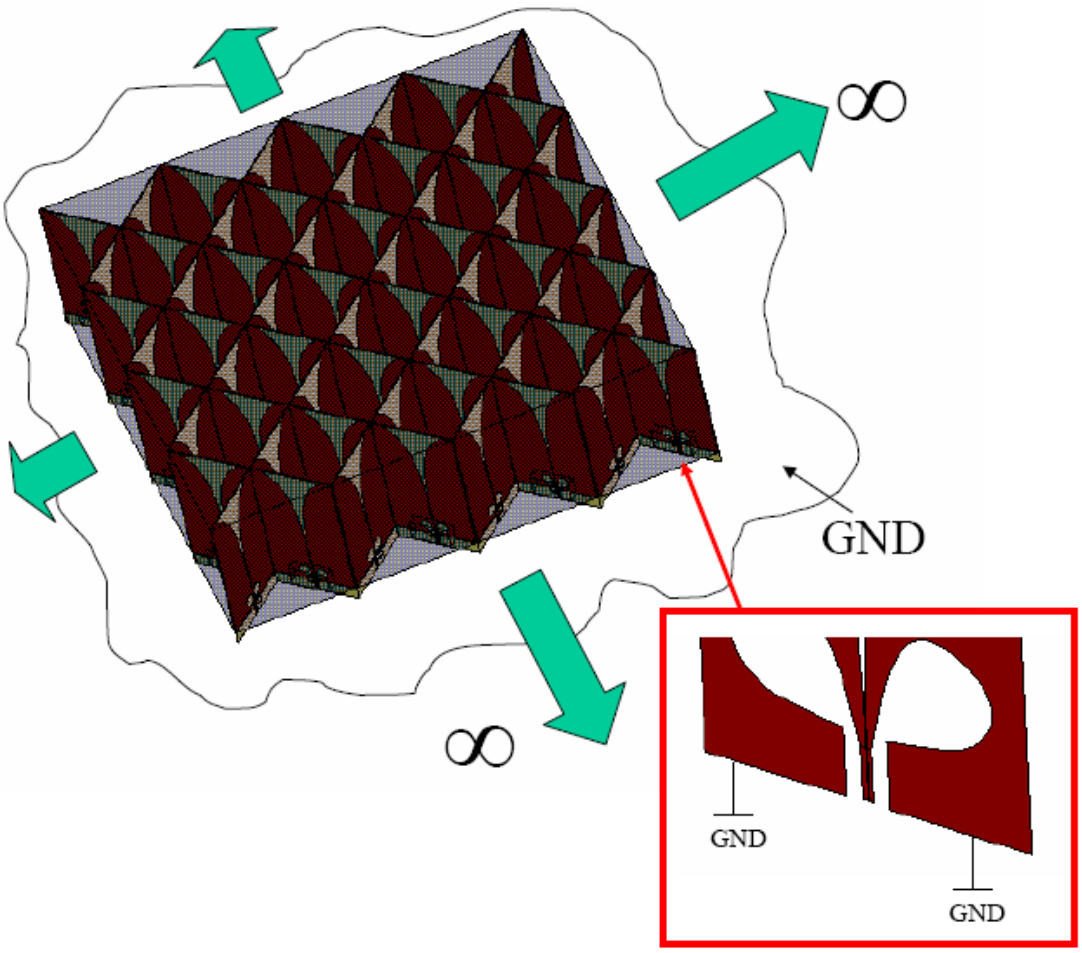

Figure 3.21: One tile embedded in the infinite array and the ground plane below.

antennas radiate in only one direction (end-fire radiators), the reflector ground plane may not be necessary for controlling the radiation, and if a bridge could be used instead of a ground plane it would represent a further cost saving. Unfortunately it is quite unlikely that a ground plane is not used at all, as it will probably be required for the beamforming board.

In Fig. 3.22 one can see how the use of a bridge (and no ground plane) degrades the VSWR compared to the infinite ground plane case. However, it still falls within an acceptable range and both the locations of the resonances due to the structure geometry and the trend of the active impedance remain the same with frequency. Another difference is that by using the bridge it is possible receive some signal at the resonant frequencies in the higher part of the band. This is not possible in the case of using a ground plane, because the resonances become very sharp and strong. Furthermore, it can be seen how the highest usable frequency decreases rapidly if neither a ground plane or a bridge are used, even if the lower frequencies performance improves (below 200 MHz). Therefore, for dual-polarized arrays of the present element, it seems that the use of either a bridge or ground plane will simplify

the design in order to obtain a good performance. This is again due to the necessity to maintain the voltage balance in the ground planes of the feeding line as it was mentioned in section 3.3.1. The result for a partial connection between the ground plane and the antennas is also shown in Fig. 3.22. The connection is made only at some points along the structure. The results are still acceptable and follow the trend of the infinite ground plane case.

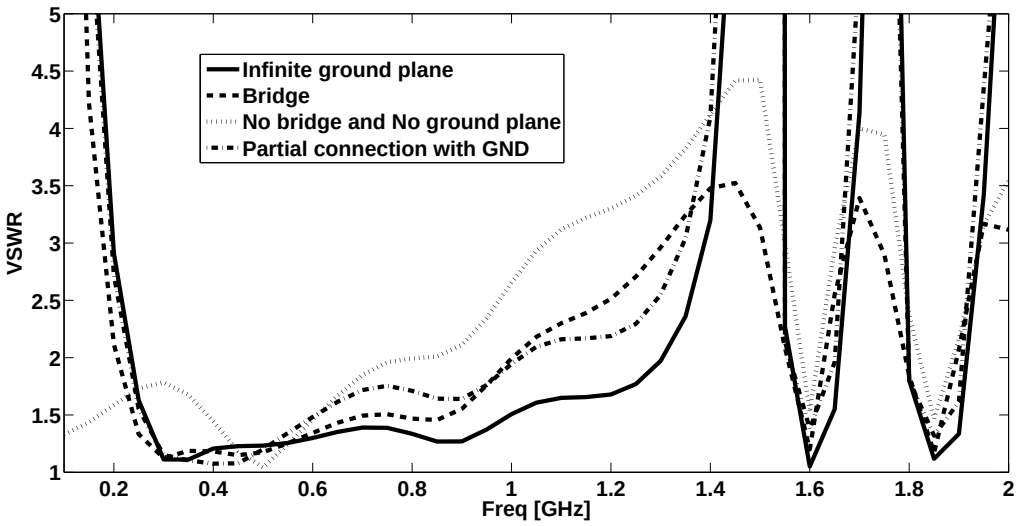

Figure 3.22: Effect of the ground plane.

3.4.4 Effect of the cavity size and the feed line

After analyzing the cavity size for the B2B structure, the cavity was further analyzed and optimized for the infinite array. As previously observed for the B2B results a larger cavity means better performance at lower frequencies.

An optimum value of 4 mm was found for the side slot of the differential CPWG line (see Fig. 3.23). This value affects the impedance matching in a similar manner as does the slot width. An optimum slot width for the CPS line was found at 0.7 mm. As in the case of the side slot, variations of the slot width change the characteristic impedance of the line and consequently the input impedance.

3.4.5 Final result at broadside

As shown in Fig. 3.20 a model with a frequency band slightly larger than 0.3 to 1 GHz has been designed for a broadside scan. The active VSWR fluctuates around 1.5, i.e. a return loss of -14 dB. This means that the requirements have been fulfilled for a dual-polarized infinite array of Vivaldi elements with differential feeding.

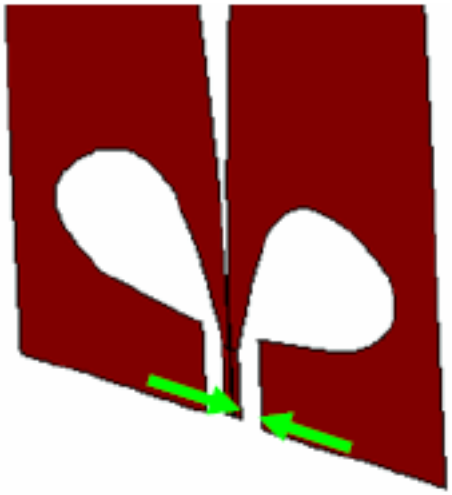

Figure 3.23: Side slot of the differential CPWG line.

3.4.6 Scanning the array

In order to design an array with full capabilities for the SKA, scanning is also desired up to 45^o in every plane. One must be careful however as there are several impedance anomalies that may appear in dual-polarized arrays of TSA elements when scanning takes place as explained more in detail in chapter 4. Also the appearance of grating lobes maybe a limitation for the scanning capabilities.

The final broadside design was considered again for scans up to 45^o in both the E- and H-planes (Fig. 3.24 and Fig. 3.25). It can be seen in Fig. 3.24 that the highest operational frequency reduces to 0.87 GHz for a 45^o scan angle. Or, the scan is limited to - 35^o to 35^o in both planes. Furthermore, the impedance match degrades rapidly with increasing scan angle (results not shown for larger scan angles).

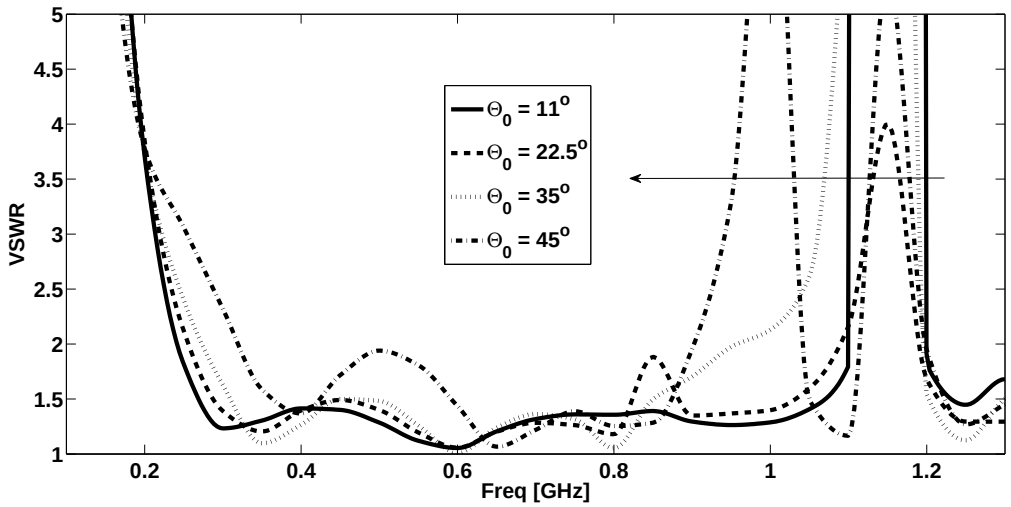

Figure 3.24: VSWR for an E-plane scan.

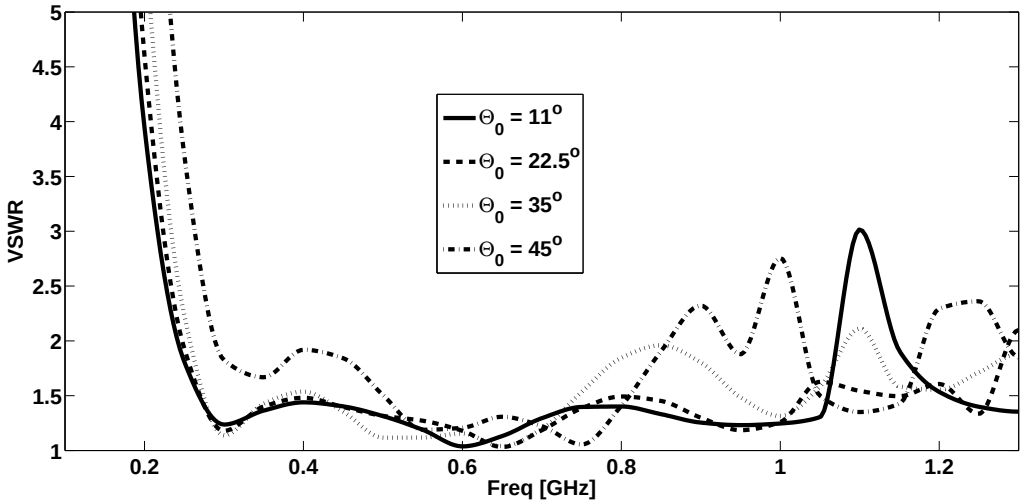

Figure 3.25: VSWR for an H-plane scan.

I carried out a parametrized simulation following the same procedure as for the broadside case. It was found, as might be expected, that the most direct way to improve the scan performance was to reduce the pitch of the antenna. Finally, using a 165 mm pitch, the results as shown in Fig. 3.26 and Fig. 3.27 were obtained. Other than the reduction of the antenna pitch, the feeding line was shortened for matching purposes from 21 to 8 mm yielding a total antenna length of 359 mm. Also the cavity size has increased.

Fig. 3.26 shows the E-plane scan performance, where fair impedance matching along the band for angles up to 45^o is observed, with the worst match at around 500 MHz (VSWR = 2.3). In Fig. 3.27 the H-plane scan performance shows a similar good result. In this case the return loss is always better than -10 dB (VSWR $\lesssim$ 2) for the entire band.

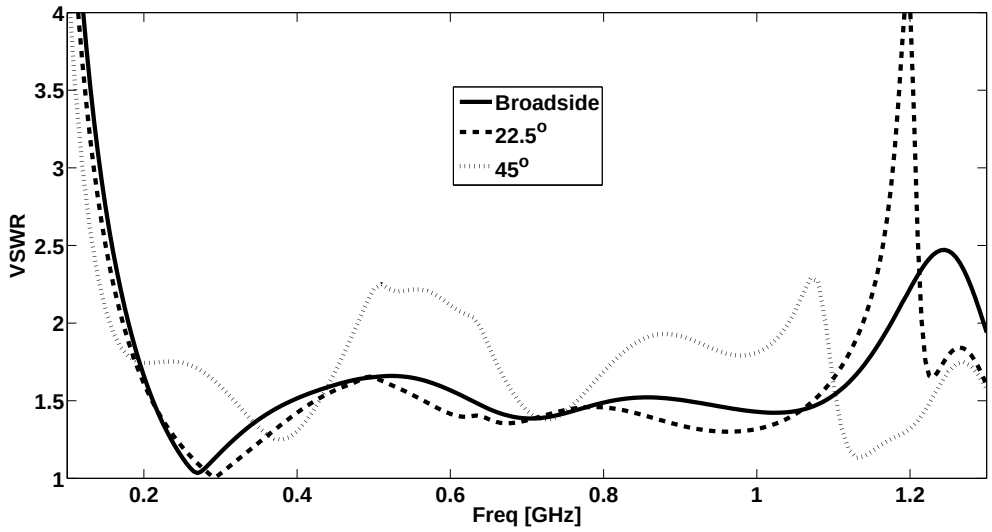

Figure 3.26: Differential VSWR for various scans in the E-plane.

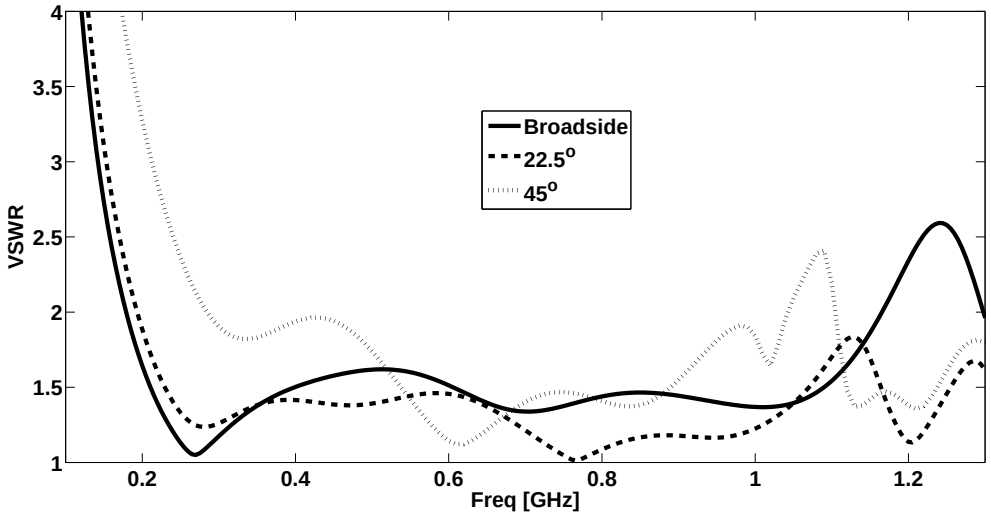

Figure 3.27: Differential VSWR for various scans in the H-plane.

Based on the designs presented in this section a finite tile of FLOWPAD[3] was built. The measurement process is explained in the coming section and its results are analyzed.

3.4.7 High-Q resonances

It is worth mentioning that, for certain designs of the feeding line, high-Q resonances were observed in the differential VSWR plot. These were initially attributed to the differential nature of the structure in the presence of a third conductor, such as a ground plane. At this point nothing else is said about this issue, but in chapter 4 an explanation is given to a similar phenomena and a low-cost - low noise solution is proposed. Furthermore, for radio astronomical applications, the energy received by tracking a source would be shortly disturbed by these resonances and it can be speculated whether this is going to distort the received data, since during a survey the received signal is integrated over a period of time.

3.5 Prototype of a differentially-fed tapered slot antenna array

This section describes the preliminary results of the differentially-fed tapered slot antenna array built as a result of the previous design studies. The main focus is on the measurement procedure (led by Michel Arts in ASTRON) and the determination of the active reflection coefficient. The properties of the common-modes are also discussed. Finally, the embedded element pattern as measured by David Zhang in the University of Manchester is shown.

The first tile of antennas was made (more than 1,250 antennas were built) following the structure shown in the computer model of Fig. 3.28. Fig. 3.29 illustrates a part of the interior of the array structure during its construction phase. The antenna elements are printed on a foil using silver ink and have been copper plated afterwards as explained in the introduction section.

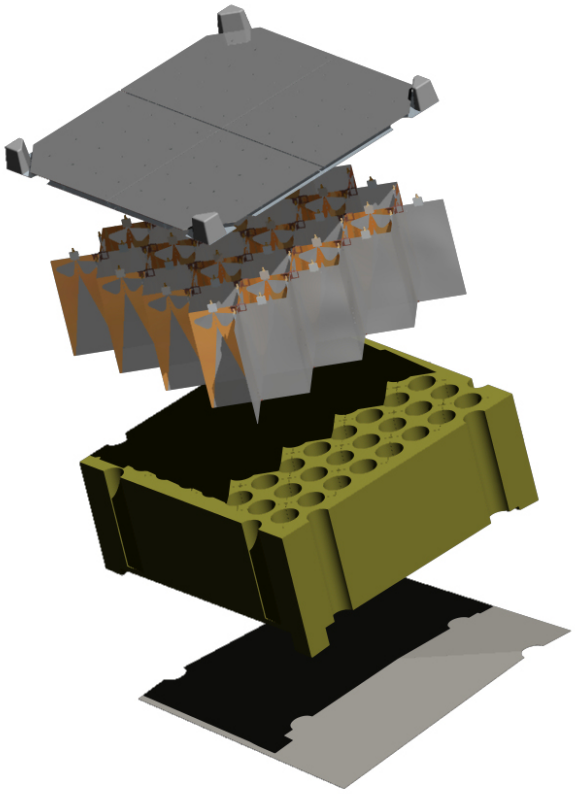

Figure 3.28: Computer model of the tile. The model is reversed.

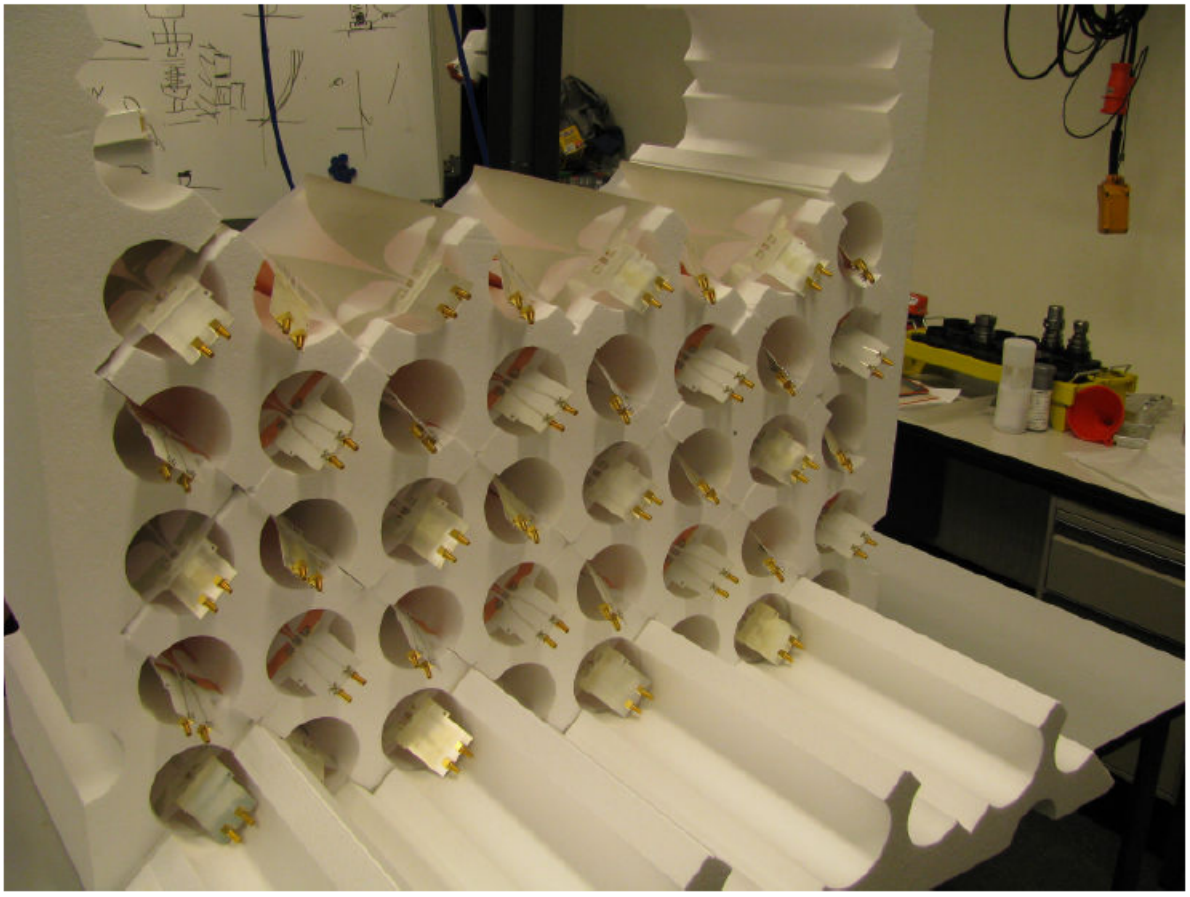

Figure 3.29: View inside the array.

The attached PCBs will contain the DLNAs in the final array design. It has been conjectured that, even though the absorption losses of the foam are expected to be low, the cylindrical holes inside the supporting structure may further reduce the foam losses as well as the associated noise contribution. In the final fully phase-steered array, each of the antenna elements will be connected to a differential LNA, providing a low noise figure while achieving a large common-mode rejection ratio (CMRR). The CMRR reduces the second order inter-modulation, which is important for wideband array systems.

3.5.1 Measurement procedure

When the technology is differential the classical measurement procedures for array antennas are no longer valid and a specific one is necessary. In this section, a measurement procedure for differential arrays using standard equipment is explained and used to measure the present array antenna. Each element is equipped with two single-ended ports instead of a differential one so that the common-mode properties of the array can be measured. These ports have SMA-connectors. Using a four-port network analyzer the full S-parameter set of the array is measured. Because the

array is symmetric, the number of S-parameters that have to be measured can be reduced. The S-matrix is measured including the feed boards between each antenna element and its two SMA-connectors. After the measurements the reference point has to be shifted from the SMA-connectors to the point where each antenna element is connected to its feed board by compensating for the transmission line length. For this purpose, a low insertion loss ($\sim$ 0 dB) and return loss ($\ll$ -10 dB) of the feed boards was assumed. After shifting the reference point, the reference impedance was renormalized from 50 to 75 Ω. This was done because the antenna is designed for a reference impedance of 150 Ω (note that the S-matrix is the matrix with the couplings between the single-ended ports, a characteristic impedance of 150 Ω for a differential port corresponds with a characteristic impedance of 75 Ω of the single-ended ports). From the renormalized S-matrix of the single-ended ports, the differential- and common-modes properties of the array can be derived. One symmetric port consists of two asymmetric single-ended ports p and q. The incident waves on the two single-ended ports of port n are denoted by $A_{p,n}$ and $A_{q,n}$. The corresponding reflected waves are denoted by $B_{p,n}$ and $B_{q,n}$. If port n is excited by a differential-mode $A_{diff,n} = 1$ the excitation of the single-ended ports is $A_{p,n} = 1$ and $A_{q,n} = -1$. If port n is excited by a common-mode $A_{comm,n} = 1$ the excitation of the single-ended ports is $A_{p,n} = 1$ and $A_{q,n} = 1$. In general, for a linear combination of common-mode wave amplitude $A_{comm,n}$ and a differential-mode wave amplitude $A_{diff,n}$ the incoming waves of the single-ended ports $A_{p,n}$ and $A_{q,n}$ are given by:

$$A_{p,n} = A_{comm,n} + A_{diff,n} \tag{3.2}$$

$$A_{q,n} = A_{comm,n} - A_{diff,n} \tag{3.3}$$

The differential- and common-modes can be obtained as a function of the incoming waves of the sub ports p and q by the inverse of 3.2 and 3.3:

$$A_{diff,n} = \frac{A_{p,n} - A_{q,n}}{2} \tag{3.4}$$

$$A_{comm,n} = \frac{A_{p,n} + A_{q,n}}{2} \tag{3.5}$$

For the reflected waves $B_{p,m}$ and $B_{q,m}$, $B_{diff,m}$ and $B_{comm,m}$ a similar relationship can be derived. The differential- and common-modes of a reflected wave can be derived from the reflected waves from the sub ports p and q by:

$$B_{diff,m} = \frac{B_{p,m} - B_{q,m}}{2} \tag{3.6}$$

$$B_{comm,n} = \frac{B_{p,m} + B_{q,m}}{2} \tag{3.7}$$

The coupling between the single-ended ports of element m and n is given as:

$$B_{p,m} = S_{pp,mn}A_{p,n} + S_{pq,mn}A_{q,n} \tag{3.8}$$

$$B_{q,m} = S_{qp,mn}A_{p,n} + S_{qq,mn}A_{q,n} \tag{3.9}$$

By substituting 3.2 and 3.3 into 3.8 and 3.9, and 3.8 and 3.9 into 3.6 and 3.7, and writing the results in matrix notation, one can get:

$$\begin{pmatrix} B_{diff} \\ B_{comm} \end{pmatrix} = \begin{pmatrix} S_{diffdiff} & S_{diffcomm} \\ S_{commdiff} & S_{commcomm} \end{pmatrix} \begin{pmatrix} A_{diff} \\ A_{comm} \end{pmatrix} \tag{3.10}$$

The elements m, n of the sub matrices $S_{diffdiff}$, $S_{diffcomm}$, $S_{commdiff}$ and $S_{commcomm}$ are defined by:

$$S_{diffdiff,mn} = \frac{S_{pp,mn} - S_{pq,mn} - S_{qp,mn} + S_{qq,mn}}{2} \tag{3.11}$$

$$S_{diffcomm,mn} = \frac{S_{pp,mn} + S_{pq,mn} - S_{qp,mn} - S_{qq,mn}}{2} \tag{3.12}$$

$$S_{commdiff,mn} = \frac{S_{pp,mn} - S_{pq,mn} + S_{qp,mn} - S_{qq,mn}}{2} \tag{3.13}$$

$$S_{commcomm,mn} = \frac{S_{pp,mn} + S_{pq,mn} + S_{qp,mn} + S_{qq,mn}}{2} \tag{3.14}$$

The vectors A_{diff} , A_{comm}, B_{diff} and B_{comm} are defined by:

$$A_{diff} = (A_{diff,1}...A_{diff,n}...A_{diff,N})^T \tag{3.15}$$

$$A_{comm} = (A_{comm,1}...A_{comm,n}...A_{comm,N})^T \tag{3.16}$$

$$B_{diff} = (B_{diff,1}...B_{diff,n}...B_{diff,N})^T \tag{3.17}$$

$$B_{comm} = (B_{comm,1}...B_{comm,n}...B_{comm,N})^T \tag{3.18}$$

where N is the number of elements and T denotes the matrix transpose.

In general the active reflection coefficient of element m for a scan direction (θ_0, ϕ_0) is calculated as:

$$\Gamma_{act,m}(\theta_0,\phi_0) = \sum_{n=1}^{N} S_{m,n} e^{-jk(x_n sin\theta_0 cos\phi_0 + y_n sin\theta_0 sin\phi_0)} = \sum_{n=1}^{N} S_{m,n} e^{-jk(x_n u_0 + y_n v_0)} \tag{3.19}$$

with

$$u_0 = sin\theta_0 cos\phi_0 \tag{3.20}$$

$$v_0 = sin\theta_0 sin\phi_0, \tag{3.21}$$

where (x_n, y_n) is the position of element n and k the wavenumber. Because the sine and cosine functions are always between -1 and 1 the following relation between u_0 and v_0 holds:

$$u_0^2 + v_0^2 < 1 \tag{3.22}$$

The region for which this relation holds is called the "visible space".

Each of the four sub matrices mentioned above can be used to calculate four different active reflection coefficients. It is possible then to calculate the active reflection coefficient for broadside ($u_0 = 0$, $v_0 = 0$) by using the $S_{diffdiff}$ matrix. This reflection coefficient is referred as the differential-mode active reflection coefficient. The differential-mode active reflection coefficient shows the amount of differential-mode power that is reflected if all elements are excited differentially. Fig. 3.30 illustrates this reflection coefficient for all x-polarized elements. One can see that the differential-mode active reflection coefficient is lower than -5 dB between 0.6 and 1.2 GHz. This is not good compared to the specification of -10 dB (see section 3.5.2 for the explanation). The active reflection coefficient for broadside of all x-polarized elements calculated by using the $S_{commcomm}$ matrix is shown in Fig. 3.31. This active reflection coefficient is the common-mode active reflection coefficient. The active reflection coefficient is near 0 dB for most frequencies. This means that if the antenna is excited with a common-mode signal all common-mode power will be reflected. i.e. a common-mode signal will not be radiated by the array (in a transmission sense). Note that the active reflection can be larger than 0 dB for some elements if the active reflection coefficient for other elements is less than 0 dB; this does not necessarily violate the principle of conservation of energy. Fig. 3.32 shows the active reflection coefficient for broadside of all x-polarized elements by using the $S_{commdiff}$ matrix. This active reflection coefficient is a measure of the cross talk between the incident differential-mode and the reflected common-mode. It is better than -10 dB for all frequencies and even below -20 dB between approximately

0.2 and 1 GHz. Ideally an incident differential-mode should not cause a reflected common-mode.

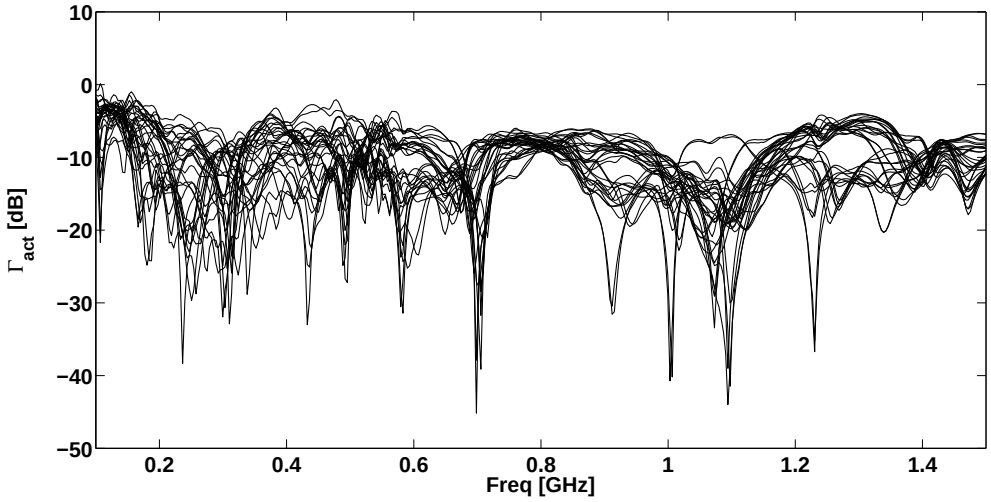

Figure 3.30: Differential-mode active reflection coefficient of all x-polarized elements at broadside ($Z_0 = 75\ \Omega$ (single-ended)).

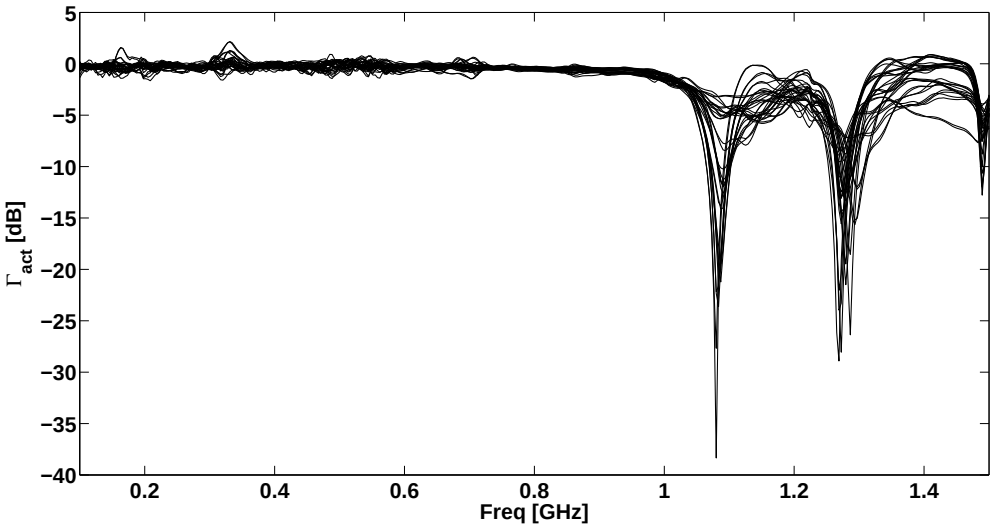

Figure 3.31: Common-mode active reflection coefficient of all x-polarized elements at broadside ($Z_0 = 75\ \Omega$ (single-ended)).

3.5.2 Comparison with simulations

The array has been designed using an infinite array approach. After the S-parameters of the array were measured, a finite array simulation (using [16]) was performed to verify the results. However, the array was too large to perform a full S-parameter simulation with single-ended ports. For that reason, the two single-ended ports of each element were replaced by a single differential port and the array was simulated

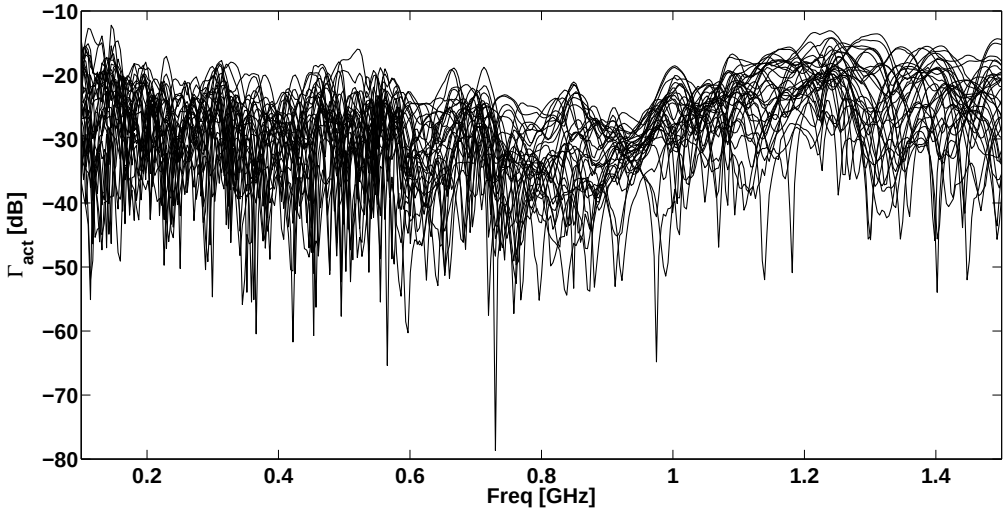

Figure 3.32: Active reflection coefficient (based on $S_{commdiff}$) of all x-polarized elements at broadside ($Z_0 = 75\ \Omega$ (single-ended)).

in the time-domain for one excitation. Fig. 3.33 shows the simulated differential-mode active reflection coefficient of the infinite and finite array simulations together with the measured differential-mode active reflection coefficient. The measured differential-mode active reflection coefficient is shown as well. Array simulation and measurement was made for one of the four center elements. One can see that the infinite array simulation predicts an active reflection coefficient of less than -10 dB between 0.2 and 1 GHz. The finite array simulation is rather different from the infinite array simulation which shows that the finite array effects are significant. As expected, the measurements are much closer to the finite array simulations. Because a full S-parameter simulation could not be performed, the common-mode active reflection coefficient could not be computed. It is possible however to perform a simulation in which all single-ended ports of all x-polarized elements are excited. However, it is important to keep in mind that a SKA-AAhi station will behave similarly to an infinite array.

The simulated and measured single-ended active reflection coefficient of element "16x" (center element) is shown in Fig. 3.34. One can see that the measurements and simulations are in good agreement.

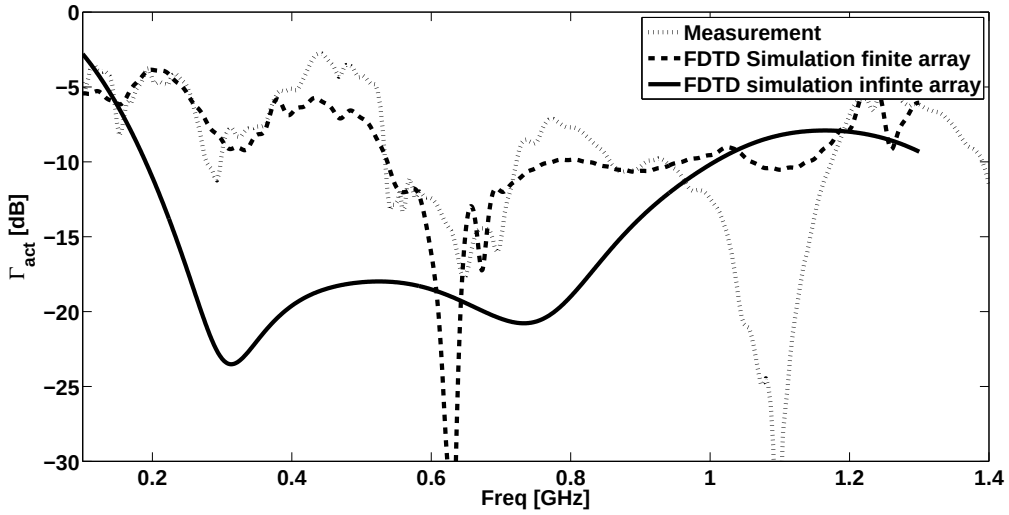

Figure 3.33: Simulated differential-mode active reflection coefficient of both a finite and an infinite array. The measured differential-mode active reflection coefficient is shown as well.

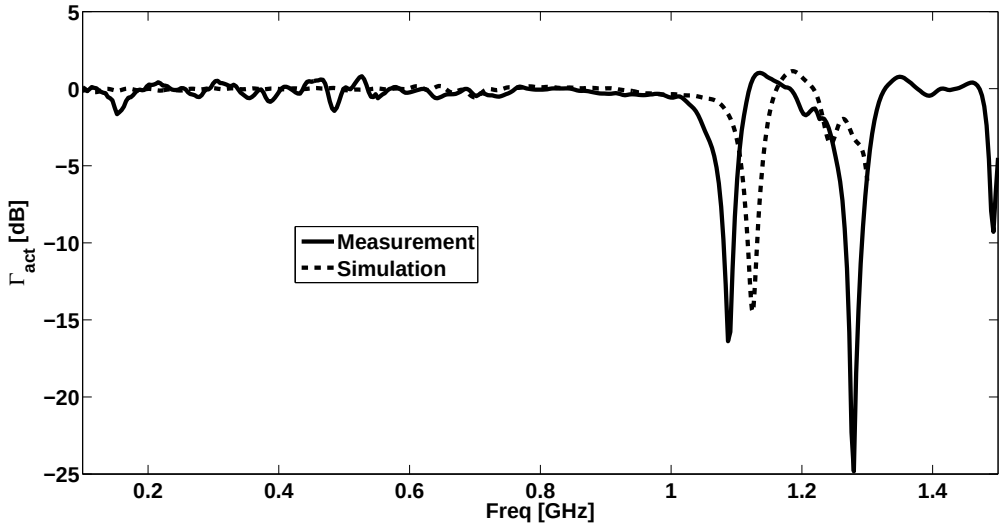

Figure 3.34: Measured and simulated single-ended active reflection coefficient of one of the four center elements.

3.5.3 Embedded element pattern

The embedded element pattern was measured in an anechoic chamber (see Fig. 3.35) for an antenna element located in the center of a 16x16 elements array (FLOTT prototype). The normalized patterns for the E, D and H-planes are shown in Fig. 3.36, 3.37 and 3.38. In these results one can see that in the E-plane the cross-polarized pattern is lower than 15 dB with respect to the co-polarized one in the scanning range (-45^o to 45^o). In the H-plane this degrades down to 10 dB in the worst case and the diagonal plane has the worst ratio with a 4 dB cross-polarization at 1 GHz at 40^o. This can be and will need to be calibrated out for a proper

functionality of the telescope. It is however still undecided which is the best way to perform this calibration for an array of the size of the SKA.

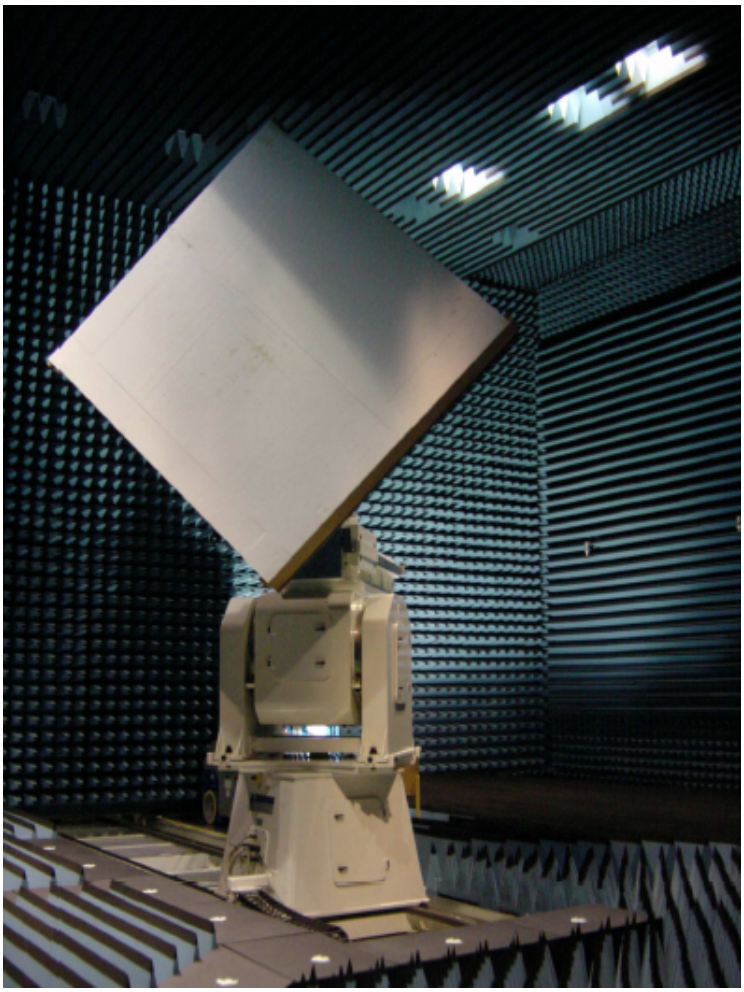

Figure 3.35: FLOTT prototype in the anechoic chamber.

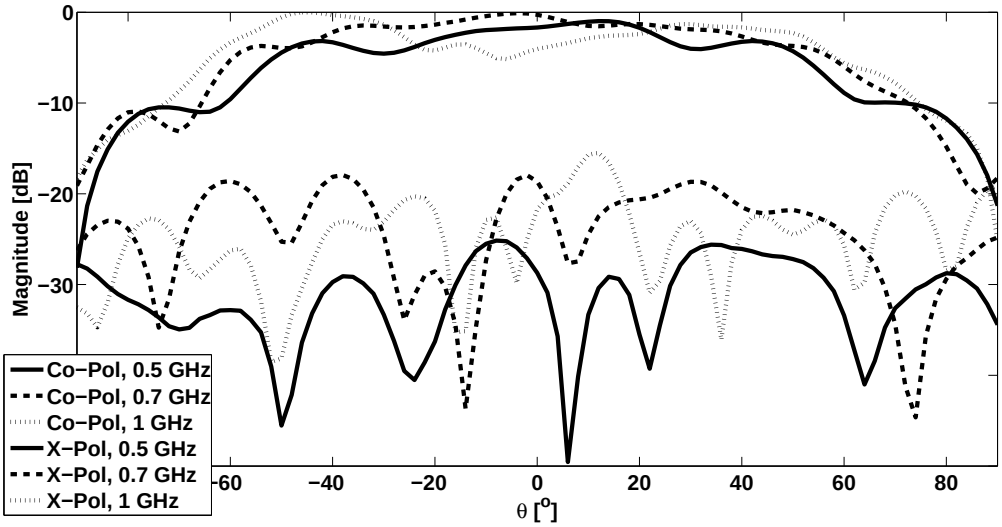

Figure 3.36: E-plane cut of the embedded element pattern for a center element in a 16x16 elements array.

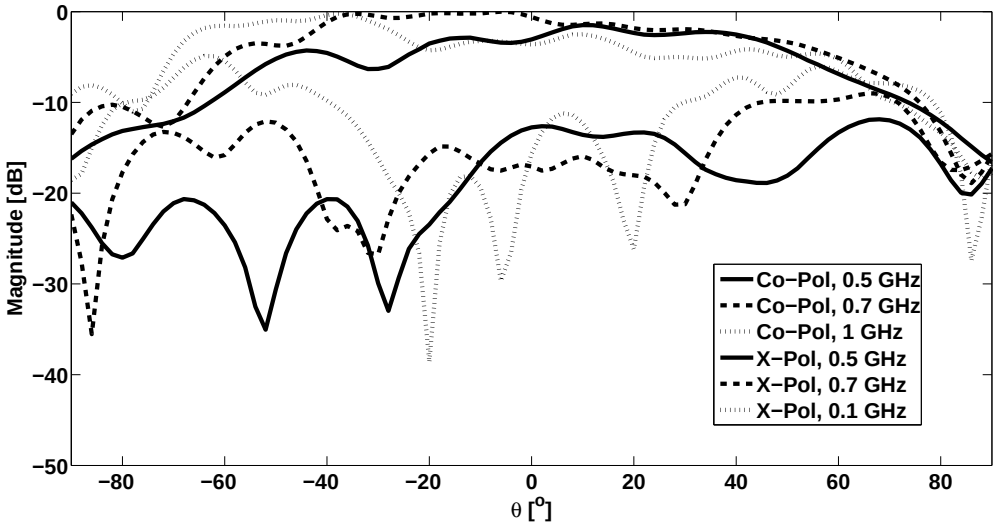

Figure 3.37: D-plane cut of the embedded element pattern for a center element in a 16x16 elements array.

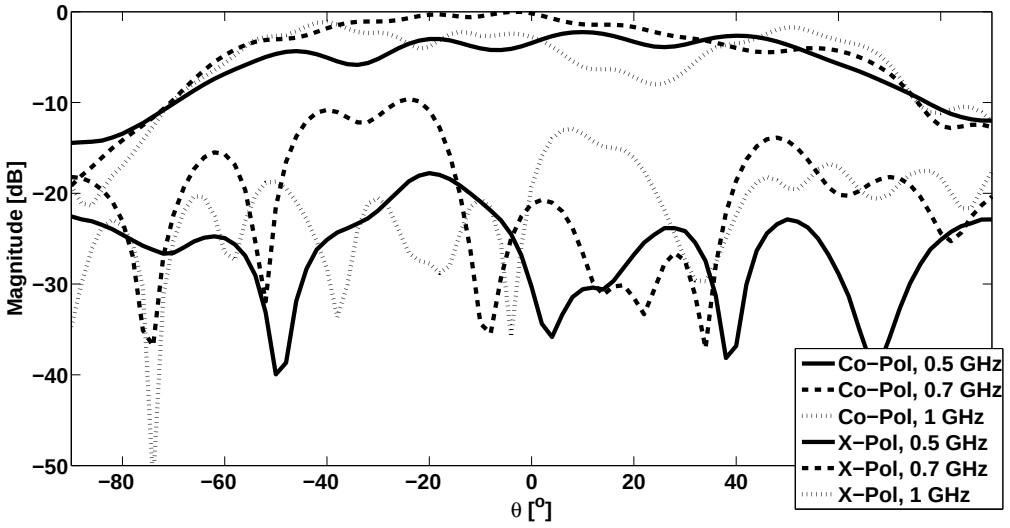

Figure 3.38: H-plane cut of the embedded element pattern for a center element in a 16x16 elements array.

3.5.4 Conclusions

The difference between the simulated (infinite array) and measured (finite array) active reflection coefficient is significant. The finite array simulation showed a better agreement implying that the finite array effects are significant. The common-mode active reflection coefficient for broadside is almost 0 dB for most part of the frequency band. This means that the receiving cross section for the common-mode is approximately zero for broadside.

3.6 Conclusions and future work

An infinite dual-polarized array of Vivaldi elements, each fed with a differential transmission line, has been designed to meet the specifications of the SKA telescope. The present design prevents the need of a reflector ground plane and satisfies the following main requirements:

- low-cost using inexpensive materials;
- differential feeding of the tapered slot antennas; and
- pitch as large as possible in order to have a minimum number of antennas and DLNAs per square metre.

The effects of the different geometrical parameters of the feeding structure were studied for a B2B configuration, In particular, the transition from the differential transmission line to the slot of the antenna was optimized. The requirements were fulfilled for broadside scan with the array printed on a very thin substrate or even without substrate. The desired scan range from -45^o to 45^o in both the E- and H-plane was obtained for an antenna pitch of 165 mm and 359 mm of total length.

Finally, a model optimized for the construction purposes, was built and a differential measurement process was undertaken. The differential measurement of the system showed good results.

As a result of this effort, two prototypes (FLOWPAD^3 and FLOTT) have been built and measured to be used as front end technology for the 2PAD project, demonstrator for SKADS. It will be then considered as a candidate for the final design of the SKA telescope. Furthermore, one technical report for the SKADS project [41], two contributions to workshops [42, 43] and two conference proceedings [44, 45] have been published. The experience gained in the design of FLOWPAD^3, was also helpful in the design of FIDA^3.

In future, several lines of work will be considered:

1. To elaborate upon the relationships between the common-mode and the differential-mode scan impedances and their relationships to high-Q anomalies associated with differential technology for this particular design.

2. To study the effect of the finiteness of the array. Even if the array is regarded as infinite due to the large number of elements present in each station of the telescope, it is important to analyze the effect of different realizations of the array, e.g. if this is regarded as a collection of tiles, what is the effect of connections between tiles. It will be also necessary to quantify the edge effects for large stations. This should be done by simulating infinite-by-finite arrays

and large finite arrays, making use of numerical-method-based codes such as [19, 18]. This information is especially valuable for calibration purposes. The results of such an analysis would useful to elaborate on the necessity of e.g. dummy elements in the outside of the array in order to reduce the effect of the finiteness of the array.

3. To characterize the cross-polarization patterns of the array for all angles and scan angles. The next phase of the SKA project will be focused on developing calibration systems, which in most cases will require a very accurate knowledge of the cross-polarization patterns.

4. An analogue ultra-wideband beamforming network will be necessary if the conversion to digital happens at a later stage. Undesired anomalies could arise from specific designs of the LNAs and the beamforming network.

In this chapter, the use of low-cost materials and fabrication procedures for differentially-fed array antennas, was a key parameter. In the next chapter, the designs presented will be focused on a differentially-fed structure with no dielectric at all. Also, helped by the experience gained designing FLOWPAD^3, I will study in depth the narrow band anomalies caused by mutual coupling and I will propose a low-noise solution to dissipate them.

Chapter 4

Dielectric-Free Differentially-Fed Tapered Slot Antenna Array

In the previous chapter, I presented a novel low-cost differentially-fed array antenna for the SKA. In this chapter I will focus on a differentially-fed prototype with no dielectric and I will study the narrow band anomalies associated to mutual coupling in this type of structures.

Next-generation radio astronomy, e.g. the SKA, will aim for very versatile multi-application and multi-beam instruments which, in the case of the SKA, will use the so-called aperture arrays [9] as core collector technology. To realise the ambitious scientific objectives of the SKA new technologies are required to provide very large collecting area (in fact greater than one square kilometre) antenna technology, which is very wide band, dual-polarized and can be mass-produced at reasonable cost. For the mid band frequency of the SKA (300 - 1000 MHz), the antennas will be placed in a dense regular configuration, where the different elements are electrically connected taking advantage of the mutual coupling and of close inter-element spacing to deliver a fixed effective aperture across the band, wider beams that result in a faster survey speed and easier beamforming, and absence of grating lobes.

This chapter contains the design of a dielectric-free ultra-wideband dual-polarized differentially-fed tapered slot antenna array, which is part of the Spanish effort, represented by the Yebes Astronomical Centre (part of the National Astronomical Observatory of Spain) and the *Universidad Carlos III de Madrid*, to build a prototype tile of antennas (1 m^2) as a potential candidate for the SKA mid-frequency band array. The prototype is called FIDA^3(FG-IGN Differential Active Antenna Array). The results of a parametric study of the proposed structure are presented. Arrays of "bunny-ear" antennas are examined and the capabilities and limitations of differential antenna technology are discussed. Other state-of-the-art designs are considered here, e.g. [30, 32, 44], however, the main advantages of this array are the reduction in losses and cost compared to arrays based on dielectric structures.

Furthermore, the use of differential technology allows us to connect to differential amplifiers in a straight-forward manner. As the focus is on radio astronomical applications, the absence of a balancing-feed circuit not only reduces the first-stage noise contribution associated to losses in the feed and the bandwidth limitation, but also leads to a further cost reduction. The main disadvantages, precisely due to its differential nature, are the anomalies which may occur in the scan impedance. Common-modes are supported by the antenna structure when a third conductor is present, such as a ground plane. It is demonstrated that anomalies may occur in the differential-mode scan impedance. Knowledge of both types of scan impedances, differential- and common-mode, is required to design differential LNAs properly and to achieve optimal receiver sensitivity. These anomalies are computed numerically, as far as there are no analytical approaches available due the complexity of the electromagnetic interactions involved in the mutual coupling mechanism, and then studied in order to understand their origin. A compromise solution is proposed based on the partial suppression of the undesired common-mode currents through a (low-loss) balancing-dissipation technique. A fully steerable design up to +/- 45^o in both principal planes is achieved.

The contents of this chapter have been published or made public in one contribution to a workshop [42], as well as in three conference proceedings contributions [50, 51, 52] and one journal paper [53].

4.1 Introduction

Tapered slot antenna arrays continue to be of great interest for ultra-wideband applications since the time they were introduced by Lewis et al. [54], in particular, the widely employed exponentially-tapered slot antennas (Vivaldi antennas, [55]). In recent years, a growing interest has emerged from the radio astronomy community in aperture arrays. The SKA will comprise a number of such antenna arrays, thereby facing one of the biggest technological challenges in radio astronomy for the 21^{st} century. The mid-frequency band, which ranges from 0.3 to ∼1 GHz, is intended to be covered by a dense array of millions of cheap dual-polarized elements that can scan up to +/- 45^o. The array design represents a challenging problem for which different technologies are being considered [56]. This chapter presents the benefits, the drawbacks, and a design example of a TSA array, which will be distinct from other studies published thus far [30, 31, 32] namely, the antennas are differentially-fed. In these, tapered slot antennas have already proven their beneficial use in dense array environments where strong mutual coupling takes place compared to other ultra-wideband elements such as spiral or log-periodic antennas. The use of TSAs in dense arrays allows for the reduction of the inter-element spacing down

to the point of electrical connection between co- and cross-polarized elements. The separation between elements (i.e. width of the elements) in arrays of TSAs can be as small as to cover a 3:1 band scanning up to +/- 45^o in a dense array configuration, with the advantages mentioned above. On top of that, TSAs are end-fire radiating elements, which is a benefit for the application being considered here, where only waves coming from the sky are of interest. The designs contained in this chapter evolved after a 4 months internship in the Netherlands Institute for Radio Astronomy (ASTRON), where I worked on the design of low-cost solutions for radio astronomy applications (see chapter 3). Before that, I designed several single elements as potential candidates for dense aperture arrays, namely wideband dipoles, optimized Vivaldi antennas and ultra-wideband baluns, e.g. [57, 58, 59]. With the experience gained in these preliminary designs and the stay in ASTRON, I selected a "bunny-ear" antenna as the best candidate for the present application.

Fig. 4.1 exemplifies five different types of TSA elements. Fig. 4.1A illustrates an exponentially tapered aperture fed by a microstrip line printed on a relatively expensive and potentially lossy substrate. Such an antenna-feed transition acts as a balancing mechanism (balun) for the differential TSA element, and is only required if a direct connection to a non-differential transmission line has to be realized [31]. Fig. 4.1B represents a bilateral Vivaldi element composed of three metal layers [30]. Fig. 4.1C shows a differentially-fed unilateral TSA element. However, it still requires a relatively expensive substrate. Fig. 4.1D illustrates a modified case compared to Fig. 4.1A, where the metal sheet used for the exponential taper of the aperture is no longer printed on a dielectric substrate, but realized by relatively thick metallic plates that are composed of e.g. aluminium [31]. Finally, an example of a differentially-fed TSA element, which is solely composed of thick metal sheets, is shown in Fig. 4.1E. This so-called "bunny-ear" antenna [60], which does not require a (lossy) dielectric substrate or additional balancing feed board, may represent an inexpensive and suitable candidate for the SKA project when aiming for differential technology. The expensive and noisy feed board is no longer required if an LNA is directly attached to the antenna and is realized in differential technology (coplanar strips for instance), or if the transition to single-ended technology has been realized within the LNA.

An important contribution to the design of differentially-fed array antennas that has been published by the SKA community thus far is the Australian “checkerboard” array [35], meant to be used as a focal plane array comprising a stack of a PCB, a foam layer, and a ground plane. The PCB consists of an array of self-complementary rectangular conducting differentially-fed pairs of patches with the appearance of a checkerboard printed on an electrically-thin dielectric substrate. The array is differentially-fed at the ground plane, with two-conductor transmission lines feeding

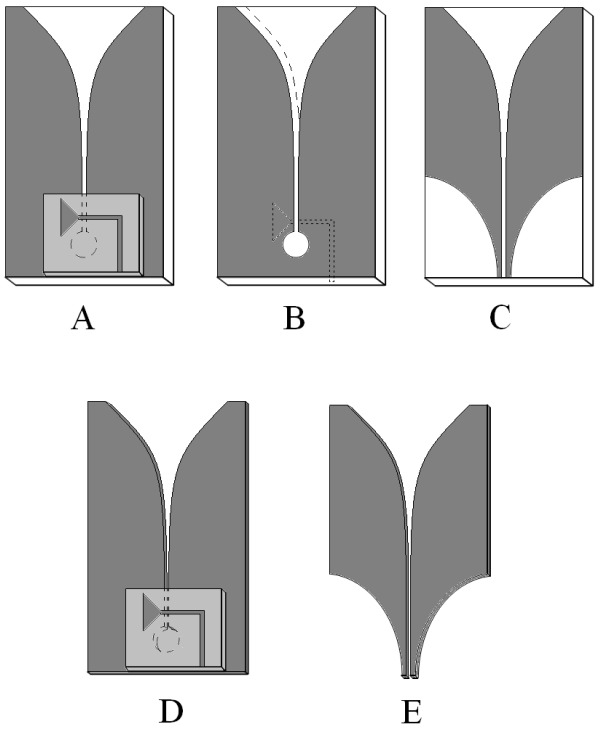

Figure 4.1: Types of TSA elements: A. Printed on a dielectric substrate with microstrip feed; B. Printed on a dielectric substrate with a stripline feed; C. Printed on a dielectric substrate with a differential feed; D. One layer of thick metal with a localized microstrip feed; E. One layer of relatively thick metals with a differential feed.

the signals between these points and the gaps between the corners of neighbouring patches of the array [61]. The conducting surfaces of the connected-patch array are topologically equivalent to those of the tapered slot array studied in this chapter. This equivalence has been detailed in section 4.3. Another array concept, which has been made and is currently being evaluated using integrated active receivers, is the dual-polarized array of differentially-fed tapered slot antennas with dual cavities explained in chapter 3.

In section 4.2, a parametric study of an infinite-by-infinite array of "bunny-ear" antennas is conducted, and used to analyze the effect of different antenna geometries on the scan impedance. The antenna elements are arranged on a square grid as shown in Fig. 4.2. By using results from references [14, 62] and by using a commercial full-wave simulator based on the Finite Element Method, named HFSS [17], it is now possible to design these complex structures and to analyze the mutual coupling effects which determine the wideband performance of the array. The closely-spaced elements exhibit strong mutual coupling effects which are still not modelled rigorously, so that full-wave simulations and design strategies are necessary [30, 32]. As explained in chapter 2, analytical approaches to mutual coupling on complex structures have not been developed, others than those for simple antenna elements as

e.g. the equations for arrays of thin dipoles in [12].

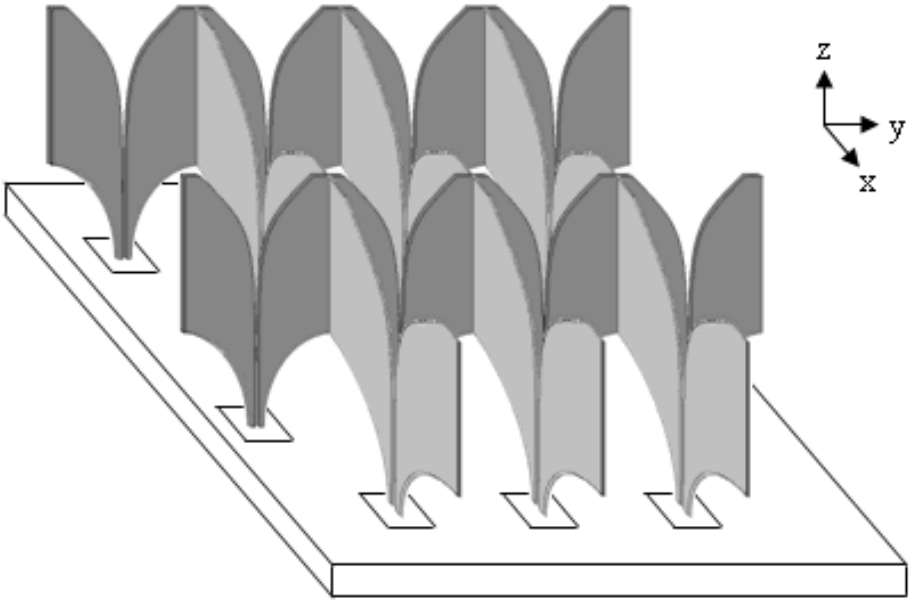

Figure 4.2: Portion of a differentially-fed TSA element array with a metallic ground plane. The elements for one of the polarizations are in dark grey and the for other in light grey. The ground plane is in white. This represents a part of a larger array.

The differential scan impedance anomalies are analyzed in section 4.3, which arise because of destructive mutual coupling interference effects. Generally, one can distinguish between several kinds of anomalies that may appear in the scan impedance [12, 15, 50, 63, 64, 65, 66, 67, 68, 69, 70]. A new type of impedance resonance for arrays of differentially-fed TSA elements has been identified and is shown to be similar to the resonance effect observed in [61]. This anomaly occurs because of the presence of a third conductor nearby the differential feeding line. This could be the back metallic plane, which is used as a reflecting surface and a virtual ground for the differential feeding lines. Without precautions, a common-mode current may then be supported by the feed structure, and even dominate over the differential-mode current for certain frequencies and array excitations/scan angles. As a result; a strong mismatch on the differential port is observed (see Fig. 4.3 for the port excitation setup), leading to a surge in the radiated power, and in turn, causes a scan blindness for the differential mode to occur. It is demonstrated that this impedance mismatch, which also leads to a noise mismatch in receiving array antennas, can be improved by means of a (low-loss) balancing-dissipation technique, and therefore the resulting array noise figure is studied as well.

In section 4.4, a design example is presented of a dual-polarized array, which is

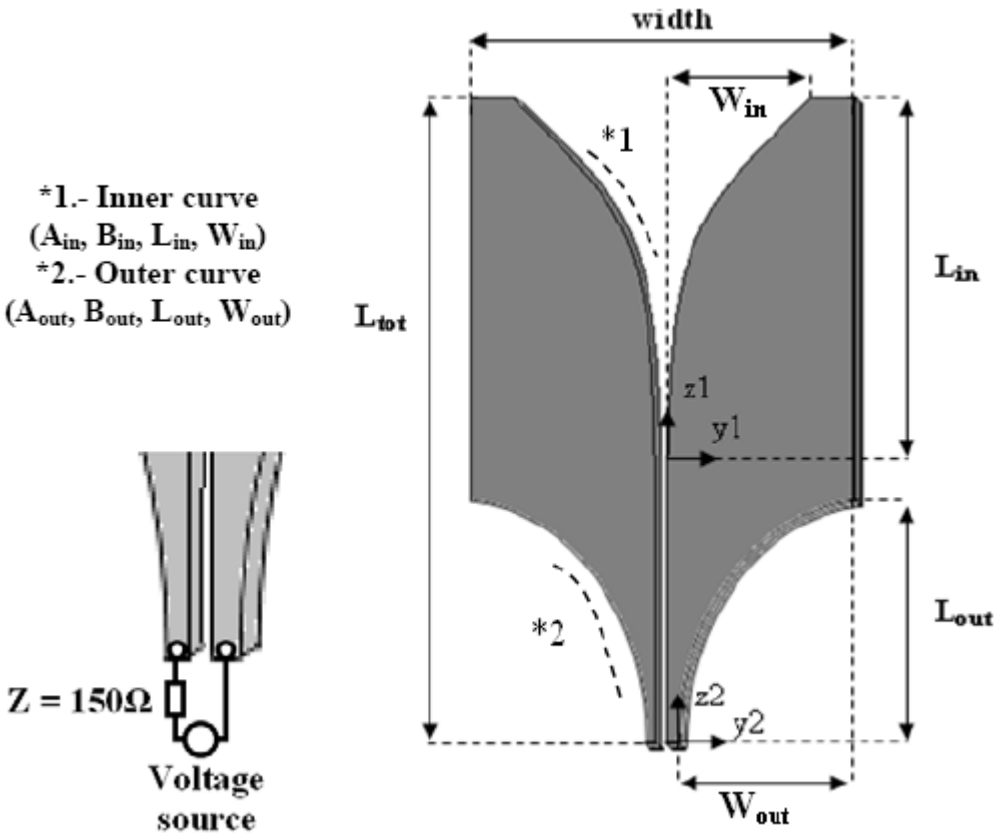

Figure 4.3: "Bunny-ear" element geometry. The antenna is excited by a voltage source between the coplanar strips of the differential feed line at the bottom of the antenna as indicated in the figure (bottom left).

steerable up to +/- 45^o in both principal planes and operates over a frequency band ranging from 300 MHz up to 1 GHz. Finally, the most relevant aspects of the study are summarized and the future work is presented.

4.2 Parametric study of the TSA element

The "bunny-ear" element in Fig. 4.3, inserted in an infinite-by-infinite array as in Fig. 4.2, is subject to a parametric analysis, i.e. the most important geometrical parameters of the antenna element are analyzed independently of each other. The large number of elements arranged in a regular grid expected to form each SKA-AAhi station, justifies the analysis in terms of infinite-by-infinite arrays. As indicated in Fig. 4.3, the antenna is excited by a voltage source which is attached to the end of the differential transmission line, and is located in the same plane as the ground plane. With reference to [32], it is known that for a stripline-fed bilateral Vivaldi antenna, the length of the inner curve, L_{in}, and the opening rate of the inner curve, B_{in}, have a pronounced effect on the scan input impedance of the array. The element width defines the E- and H-plane spacing and has a strong effect on the frequency at which

the mismatch anomaly occurs. At present, no techniques are known to suppress this type of resonance, so that it inevitably fixes the upper limit of the usable bandwidth. However, to some extent, the resonance can be shifted up in frequency by a decrease of the aperture height or width of the elements. Furthermore, an increase in the ratio of the aperture height to the antenna width will produce an enlargement of the bandwidth, though a narrower scan pattern in the H-plane is to be expected when the aperture height is increased. As for the presently proposed differential antenna, the additional aperture length, L_{out}, and opening rate, B_{out}, of the outer curve are analyzed. The outer curve aims to realize a gradual transition from coplanar strip to slotline technology such as to achieve an ultra-wideband antenna performance. Both the inner and the outer curves are described by the equations 4.1 to 4.9. The slot and strip widths have only minor influences on the scan impedance, as opposed to the aforementioned parameters [32]; therefore these parameters are chosen to be invariant in this study. Note that two sets of axes are being used, one for the inner curve (z1-y1), and another one for the outer one (z2-y2).

The inner curve is described by:

$$z_1 = A_{in} \cdot \left(e^{B_{in} \cdot y_1} - 1\right) \tag{4.1}$$

$$A_{in} = \frac{W_{in}}{e^{B_{in} \cdot L_{in}} - 1} \tag{4.2}$$

$$width/2 - W_{in} = 4.5\,mm \tag{4.3}$$

$$L_{tot} = L_{in} + 21\,mm \tag{4.4}$$

The outer curve is described by:

$$z_2 = A_{out} \cdot \left(e^{B_{out} \cdot y_2} - 1\right) \tag{4.5}$$

$$A_{out} = \frac{W_{out}}{e^{B_{out} \cdot L_{out}} - 1} \tag{4.6}$$

$$W_{out} = \frac{width - slot\_width}{2} - strip\_width \tag{4.7}$$

$$slot\_width = 1.5\,mm \tag{4.8}$$

$$strip\_width = 4\,mm \tag{4.9}$$

The difference between half the antenna width and half the aperture width (W_{in}) is fixed to 4.5 mm for assembly purposes. The 21 mm offset between the length of the inner curve (L_{in}) and the total height of the antenna (L_{tot}) is kept constant. The exact value of these parameters, as well as the slot width and the strip width, only have a minor effect on the general performance of the array. The first one is chosen to allow for space to attach the neighbour antennas, i.e. the clamps to hold the elements firmly one to another. The rest of them are chosen from a range of values which will allow the input impedance to fluctuate around the desired value of 150 Ω.

The initial geometrical parameters of the array are shown in Table 4.1. For each of the following parametric analysis, only one of the parameters is swept, while fixing the other parameters in accordance to Table 4.1. Furthermore, all results in this chapter are obtained by exciting only one of the polarizations.

Table 4.1: Initial geometrical parameters of the array.

Width	L_{in}	B_{in}	L_{out}	B_{out}
175 mm	300 mm	0.005 mm^{-1}	60 mm	0.08 mm^{-1}

4.2.1 Width of the element

The effect on the antenna input impedance, when reducing the width of the element, is visualized in Fig. 4.4 and Fig. 4.5. From the VSWR plot we can conclude that the strong impedance anomaly in the upper part of the band is downshifted in frequency when the element width is enlarged, thereby limiting the usable band and giving rise to the strong mismatch visible in the VSWR (source-reference impedance is 150 Ω). This effect is also observed when the array is scanned in both the E- and H-planes.

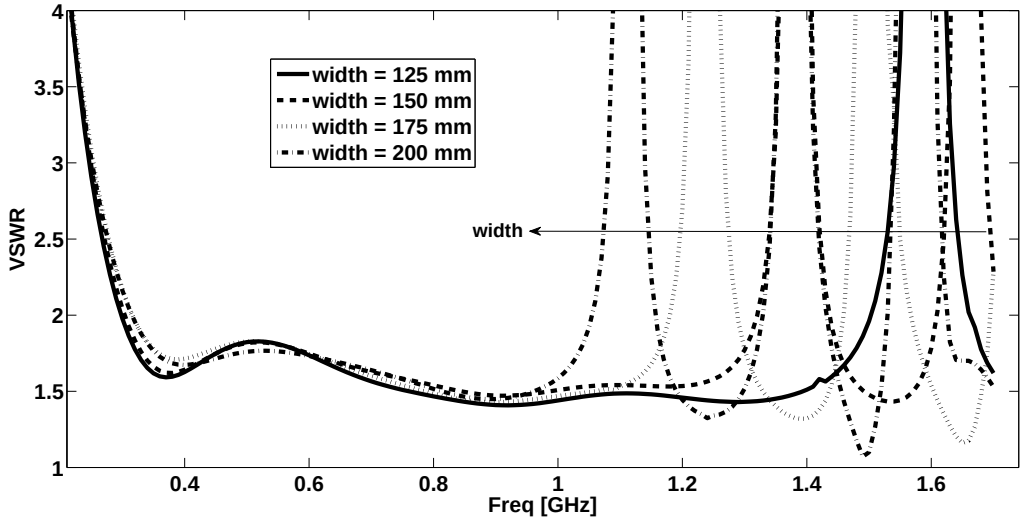

Figure 4.4: VSWR against frequency for a scan angle of 0° for various antenna widths.

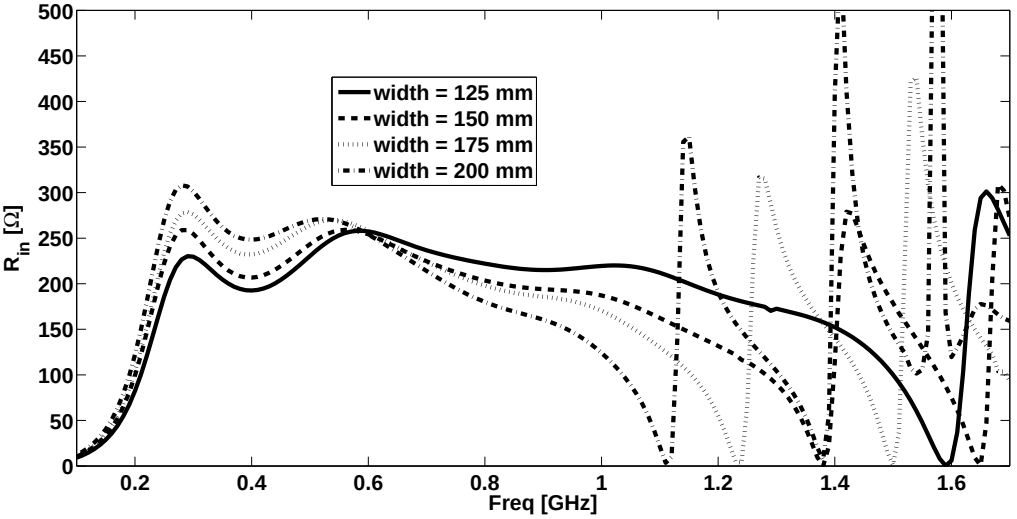

(a) Resistance

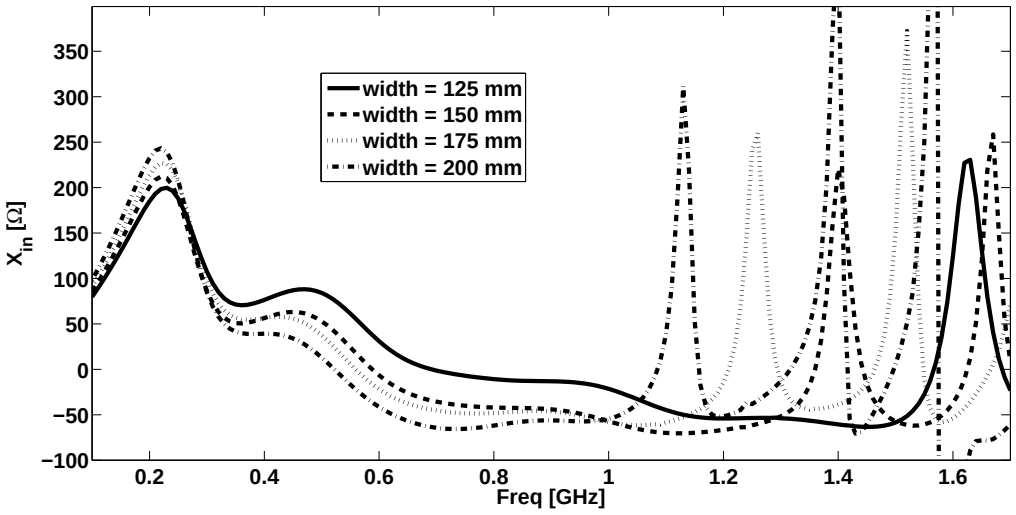

(b) Reactance

Figure 4.5: Scan impedance against frequency for a scan angle of 0° for various antenna widths.

4.2.2 Length of the inner curve (L_{in})

A reduction of the taper length of the inner aperture will result in a narrowing of the impedance bandwidth while its centre frequency shifts towards higher frequencies as shown in Fig. 4.6 and Fig. 4.7.

The use of longer tapers leads to smaller fluctuations of the scan impedance, and a smaller reactance as well, particularly at lower frequencies, thereby improving the lower usable frequency. However, the penalty is that the impedance anomalies in the upper part of the band move slightly down in frequency. A similar trend is observed when the array is scanned to 45^o in both principal planes.

In conclusion, the bandwidth of this type of arrays can be enlarged by increasing the length-width ratio of the inner taper of the antenna element, albeit only to a certain extent.

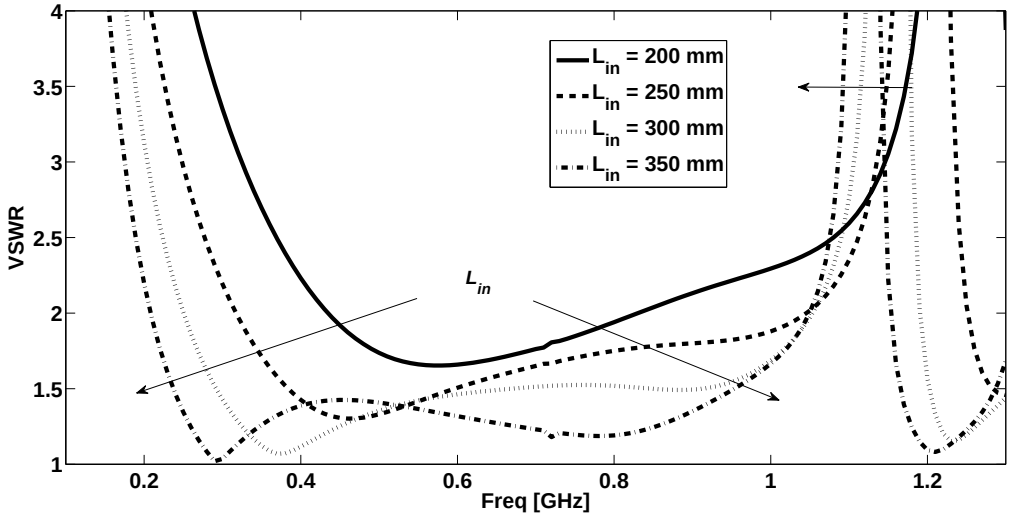

Figure 4.6: VSWR against frequency for a scan angle of 0^o for various antenna taper lengths.

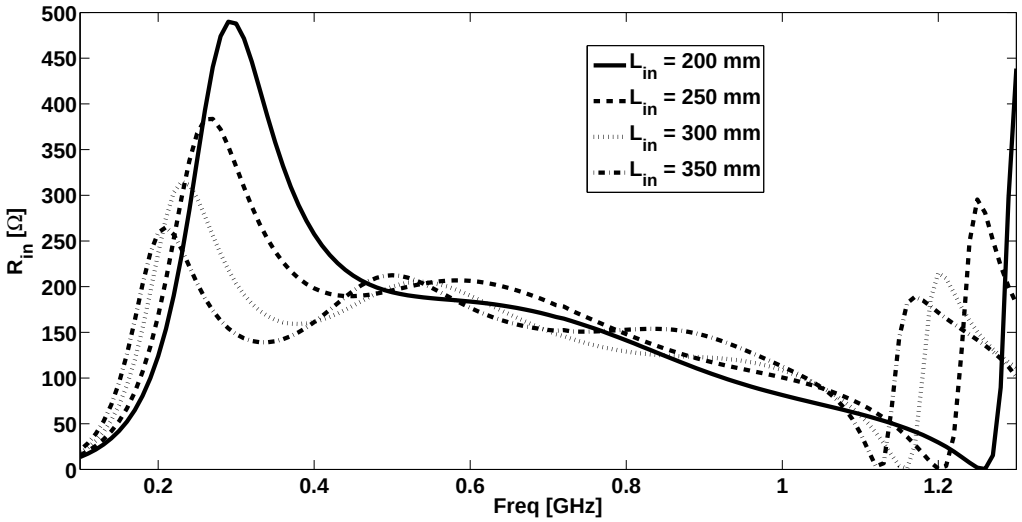

(a) Resistance

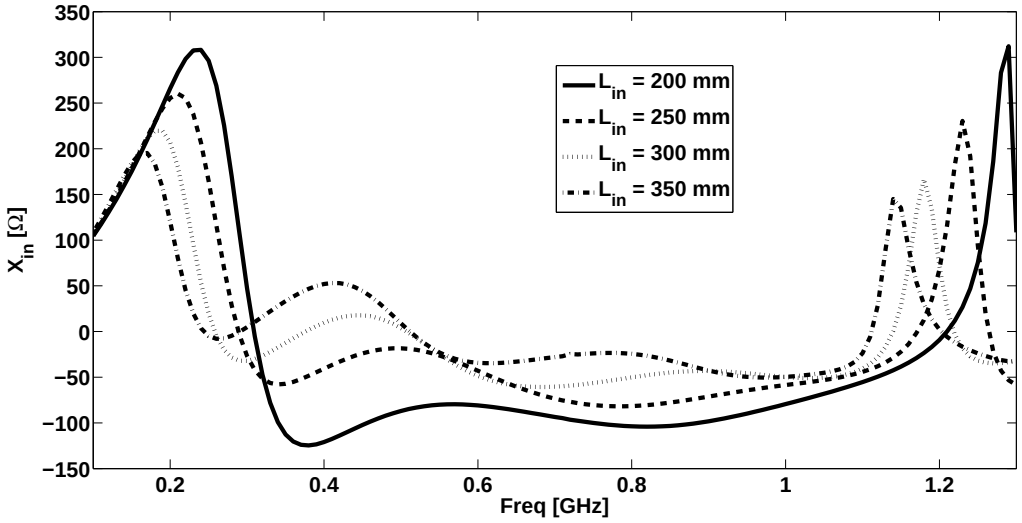

(b) Reactance

Figure 4.7: Scan impedance against frequency for a scan angle of 0° for various antenna taper lengths.

4.2.3 Opening rate of the inner curve (B_{in})

The opening rate of the inner curve of the antenna is mainly affecting the matching level in the middle of the frequency band, though it also has an effect on the lower limit of the usable bandwidth (see Fig. 4.8).

As shown in Fig. 4.9, larger opening rates lead to stronger fluctuations in the scan impedance around their mean values. These mean values flatten-out for larger opening rates, especially at the upper part of the frequency band, and therefore result in better VSWRs. At the lowest end of the band, around 400 MHz, the in-band hump in the VSWR increases with increasing B_{in} and the maximum usable frequency also reduces for larger opening rates, so that it is necessary to find a

compromise value for the opening rate of the inner curve. A similar behaviour is observed when the array is scanned up to 45^o in both principal planes.

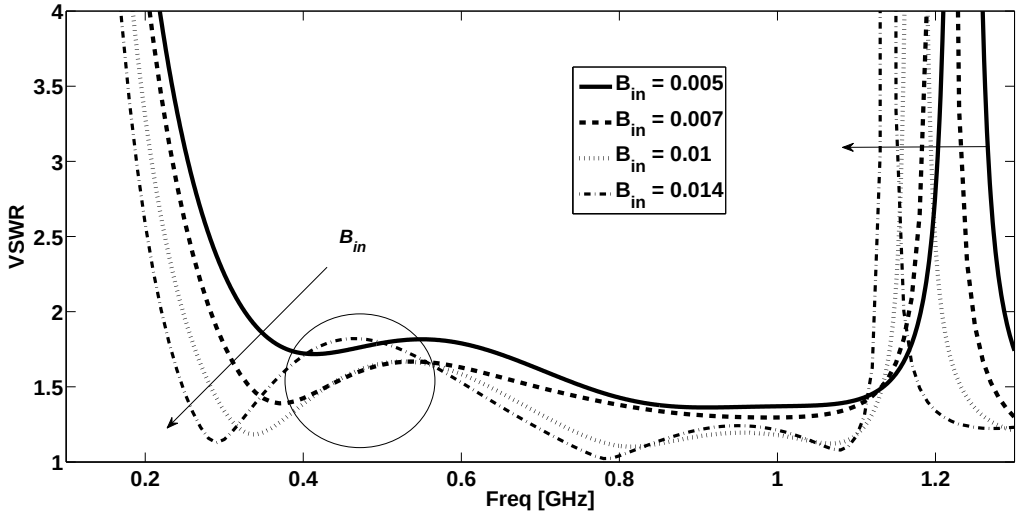

Figure 4.8: VSWR against frequency for a scan angle of 0^o for various antenna opening rates of the inner curve.

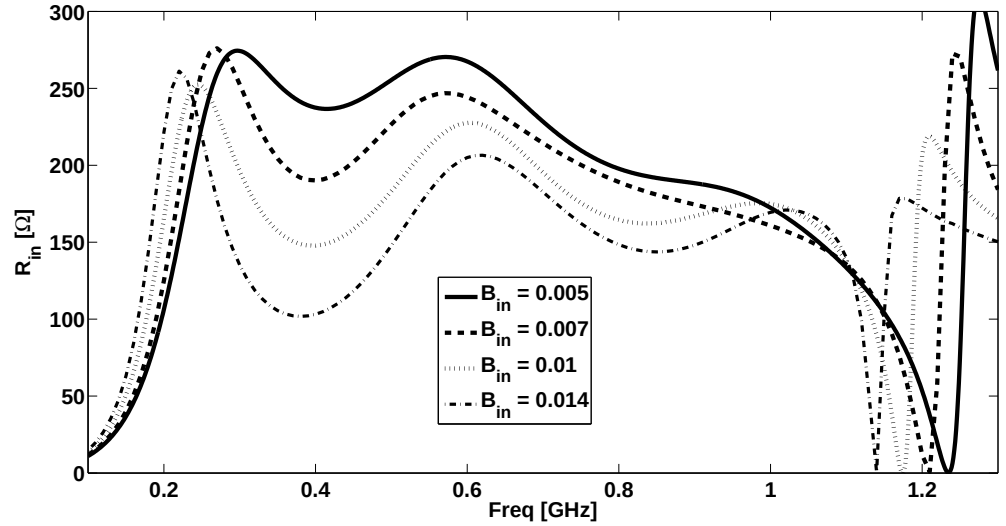

(a) Resistance

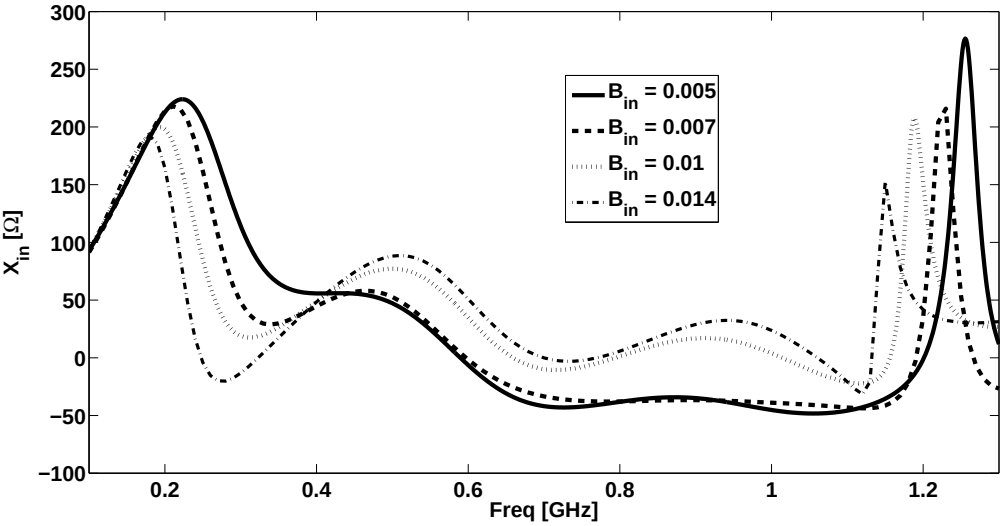

(b) Reactance

Figure 4.9: Scan impedance against frequency for a scan angle of 0° for various antenna opening rates of the inner curve.

4.2.4 Length of the outer curve (L_{out})

Results of scan impedance studies, and the occurrence of impedance anomalies, have been reported for the conventional stripline-fed bilateral Vivaldi antennas when the array is scanned off-broadside [30, 32]. To my best knowledge, no results have been reported for arrays of "bunny-ear" antennas where the effect of the outer curve on the scan impedance has been analyzed. It will be shown that several impedance effects are attributed to a specific design of the outer taper which need to be accounted for when designing and optimizing "bunny-ear" arrays.

The tapered outer curve is an important part of the differential feeding system as its length controls the smoothness of the transition from coplanar strip to slot-

line technology and, in turn, influences the scan impedance of the antenna array elements. We can observe in Fig. 4.11 that an increase in taper length leads to an increase in the input resistance, whereas the input reactance has virtually not changed, except at very low frequencies. Basically, only the matching level has changed as shown in Fig. 4.10, and the bandwidth has changed accordingly.

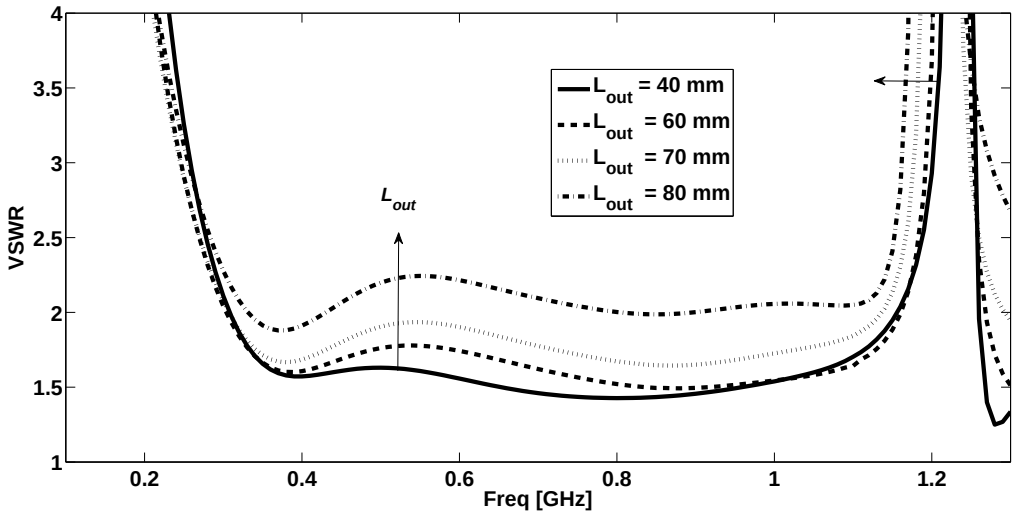

Figure 4.10: VSWR against frequency for a scan angle of 0° for various antenna lengths of the outer curve.

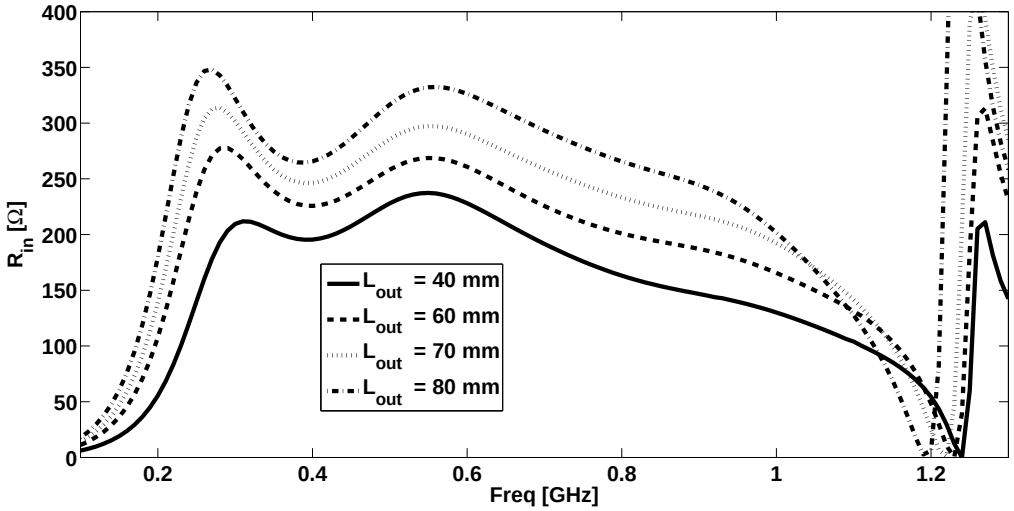

(a) Resistance

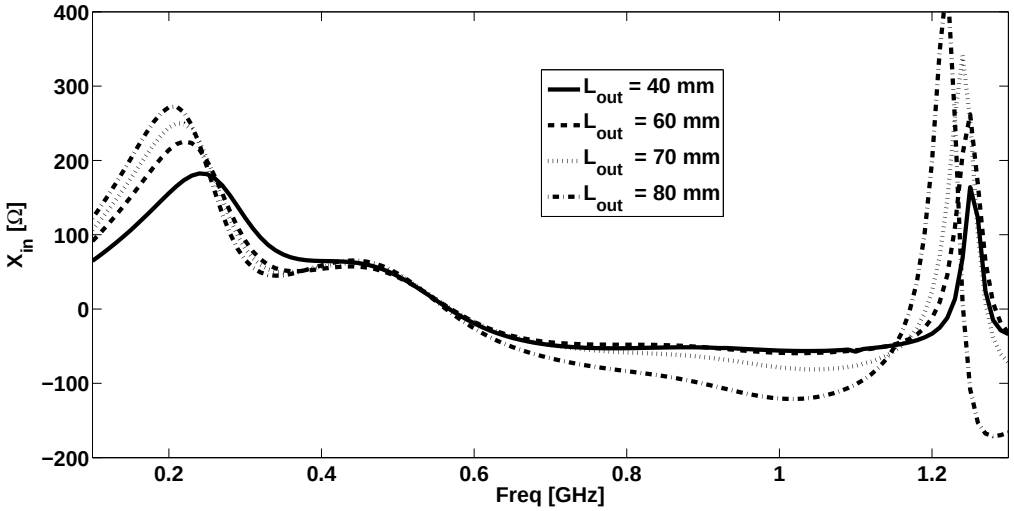

(b) Reactance

Figure 4.11: Scan impedance against frequency for a scan angle of 0° for various antenna lengths of the outer curve.

It is important to remark that for symmetric arrays of tapered slot antennas, typically only the E- and H-plane scans are of primary interest, since the D-plane scan impedance behaves, at least to first order, as a simple average of the E- and H-plane scan performances as described in [32] and confirmed here by Fig. 4.12 and Fig. 4.13 for arrays of "bunny-ear" antennas. Note that the scan angle is measured from the normal to the array.

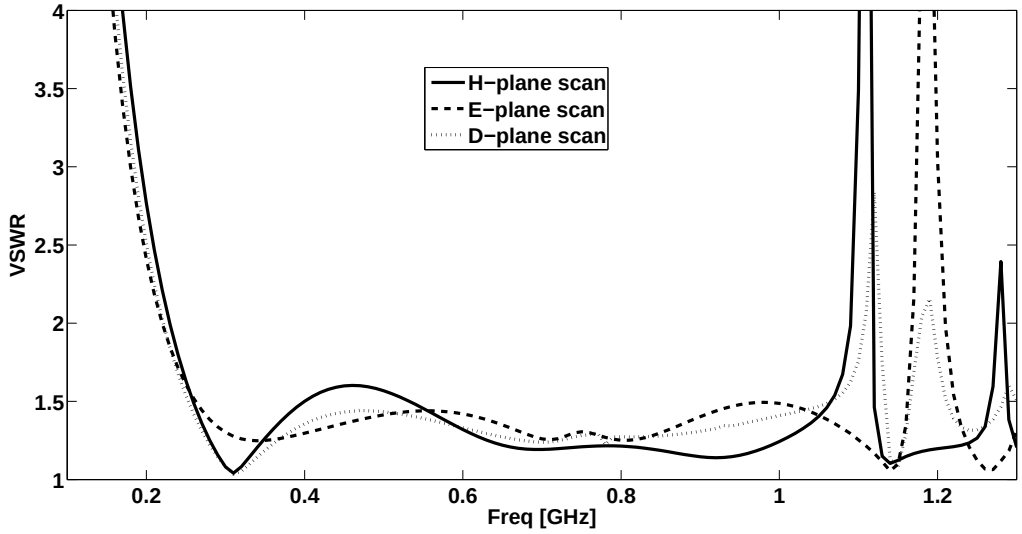

Figure 4.12: VSWR against frequency for a scan angle of 22.5^o in different planes.

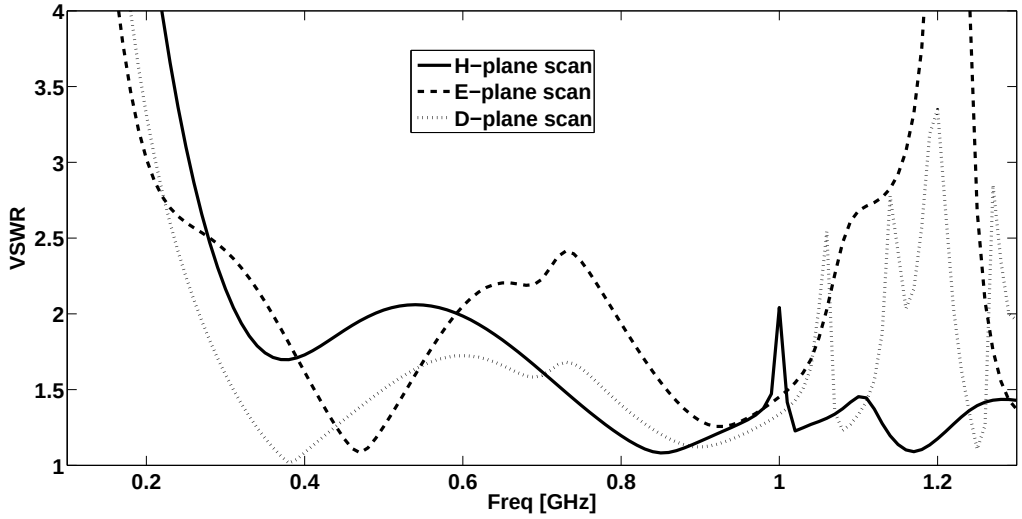

Figure 4.13: VSWR against frequency for a scan angle of 45^o in different planes.

Fig. 4.14 illustrates that when the array is scanned up to 45^o in the E-plane, an impedance anomaly (anomaly 1 in Fig. 4.14) appears within the band of interest and is strongly dependent on the length of the outer curve. It was found that the origin of this anomaly is related to the fact that the array can support a common-mode current. A more detailed explanation of its origin and suppression is given in section 4.3. So far, one can see how the length of the outer curve affects the position of the anomaly as it moves towards lower frequencies for larger taper heights.

The VSWR results are shown in Fig. 4.16 for the case that the array is scanned to 45^o in the H-plane. An impedance resonance appears in the upper part of the frequency band, thereby reducing the usable bandwidth. As in the case of anomaly 2 in the E-plane scan of Fig. 4.14, the location of this H-plane scan anomaly turns out to be virtually invariant for taper heights, as opposed to the case of anomaly

1 in the E-plane scan of Fig. 4.14. Anomaly 2 in the high part of the band is due to the appearance of the endfire grating lobe and is observed in the present unit cell computation because it corresponds to the frequency and angle at which a higher-order Floquet mode starts propagating.

Apart from the anomalous impedance effect, the trends observed in the scan impedances (see Fig. 4.17) are very similar to the broadside-scanned array case, i.e., the resistance can be raised in-band by increasing the length of the outer taper, whereas the reactance remains almost the same. The mid-frequency hump of the VSWR in Fig. 4.16 also increases with the height of the outer curve, and is in accordance with the increase in the input resistance.

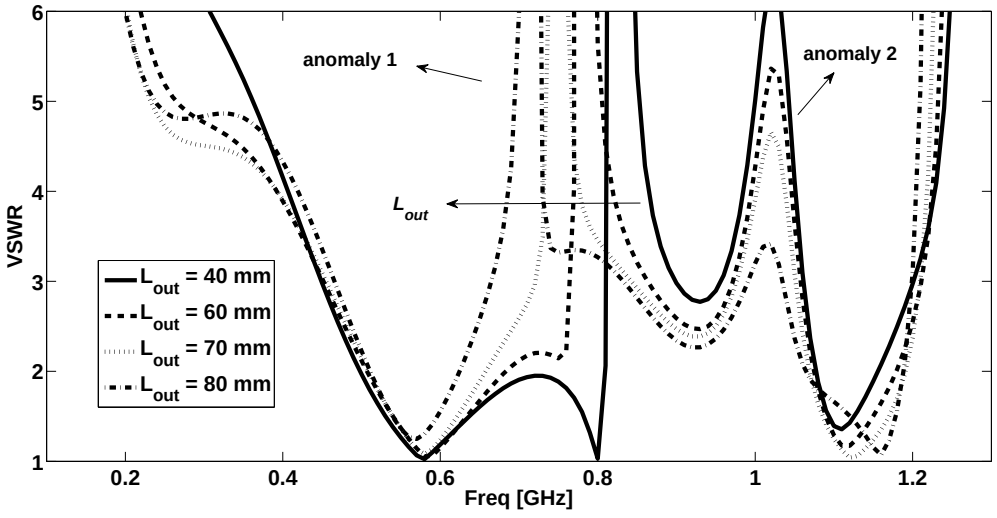

Figure 4.14: VSWR against frequency for a scan angle of 45^o in the E-plane for various antenna lengths of the outer curve.

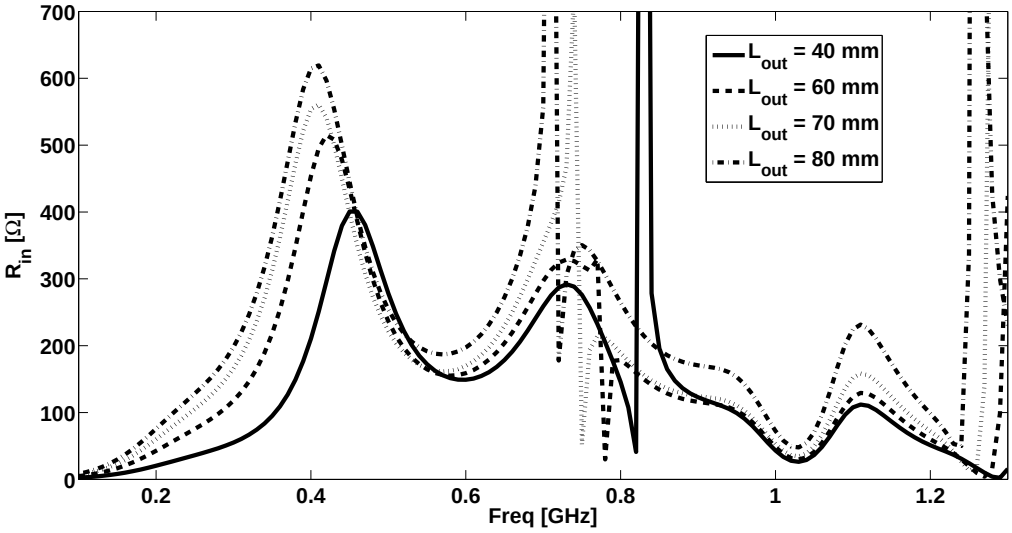

(a) Resistance

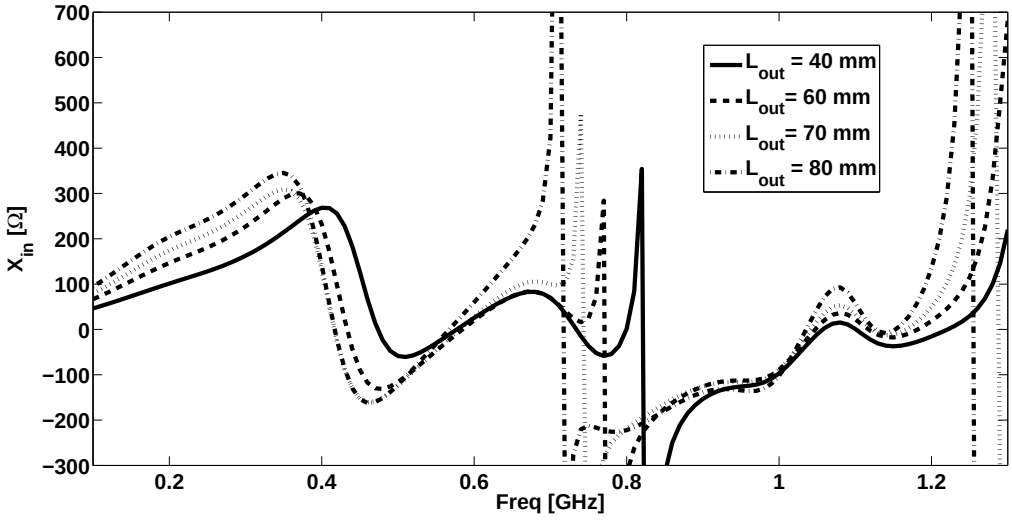

(b) Reactance

Figure 4.15: Scan impedance against frequency for a scan angle of 45^o in the E-plane for various antenna lengths of the outer curve.

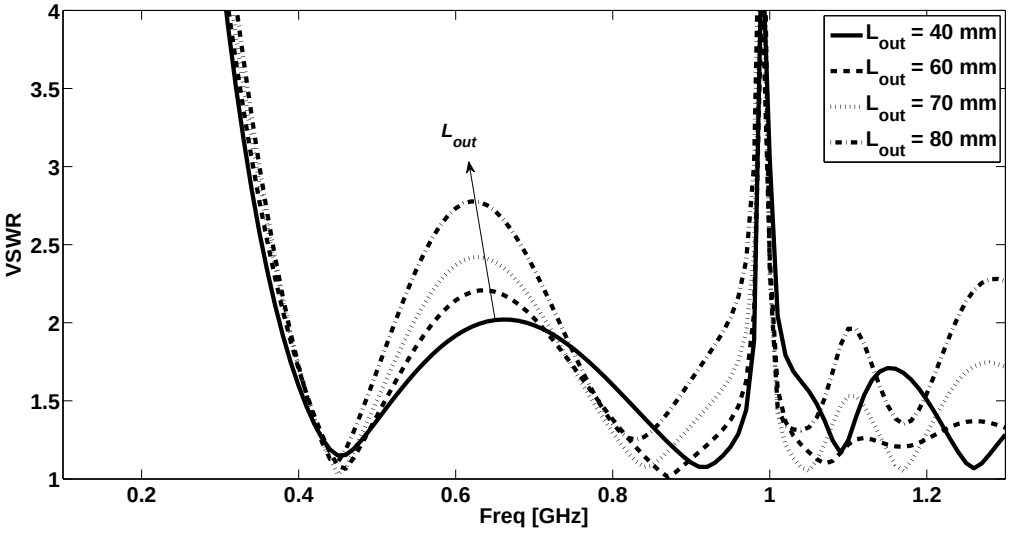

Figure 4.16: VSWR against frequency for a scan angle of 45^o in the H-plane for various antenna lengths of the outer curve.

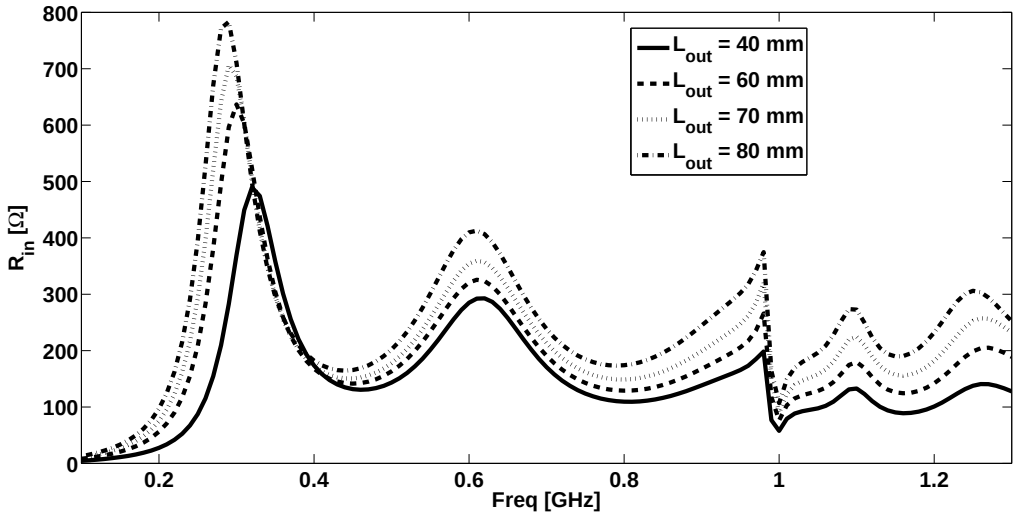

(a) Resistance

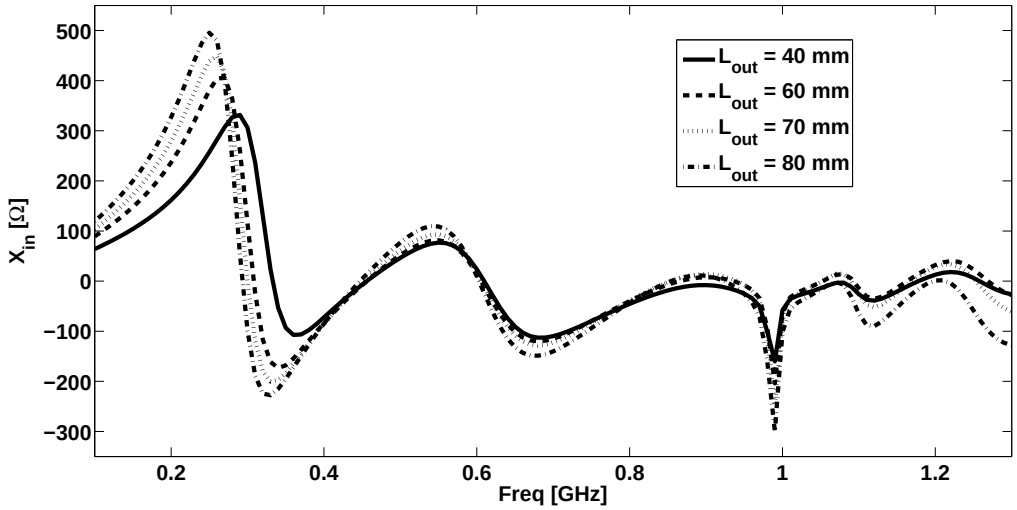

(b) Reactance

Figure 4.17: Scan impedance against frequency for a scan angle of 45^o in the H-plane for various antenna lengths of the outer curve.

4.2.5 Opening rate of the outer curve (B_{out})

The effects on the impedance characteristics of the array are only weakly dependent on B_{out}. Furthermore, variations of the opening rate of the outer curve also have a minimal effect on the impedance anomalies, as opposed to a variation of L_{out}. The respective results are therefore not shown.

4.3 Scan impedance anomalies associated to differential array technology

The presently proposed "bunny-ear" element exhibits a few E-plane scan impedance anomalies that are typically found for other Vivaldi elements as well [12, 15]. Apart from these types of resonances, a number of additional impedance anomalies exist that have been identified before and that are attributed to a particular realization of the TSA elements. Among them, (i) the impedance resonance that appears when a surface excited wave travels along the facets of a substrate (printed TSAs), which then destructively interferes with the phasing of the array; or, (ii) the impedance resonances that appear due to gaps between disjoint antenna elements/tiles that tend to radiate, thereby severely disrupting the impedance characteristics [63]; or, (iii) the impedance resonances that occur for H-plane scanned bilateral TSAs, which arise due to a voltage difference between the bilateral fins of the TSAs, and that can be eliminated by plated-through vias in the elements [30]; or, (iv) the impedance resonance that arises in triangular grid arrays of phase-steered linearly-polarized TSA arrays [64]. The presently employed "bunny-ear" antennas are dielectric-free, are electrically interconnected along their outer edges, and also unilateral and dual-polarized, so that the previously mentioned impedance resonances are not observed. However, here a type of impedance resonance which can specifically be attributed to differentially-excited arrays is identified. To examine this type of scan impedance anomaly, the geometrical parameters as listed in Table 4.2 are used.

Table 4.2: Parameters of the array for revealing the scan impedance anomaly.

$Width$	L_{in}	B_{in}	L_{out}	B_{out}
175 mm	250 mm	0.005 mm^{-1}	73 mm	0.07 mm^{-1}

The VSWR is shown in Fig. 4.18 for three different E-plane scans. Anomalous impedance effects occur for off-broadside scan angles in the middle of the band when exciting the antennas with a differential generator. It is remarkable that these resonances disappear in the absence of a ground plane and shift down in frequency with an increase in scan angle. It is important to note that the position of the strong impedance anomalies in the upper part of the band also shift down for increasingly larger scan angles, in both the E- and H-planes, though this effect is less pronounced as compared to the effect of increasing the element width, which reduces the operational bandwidth significantly.

In [15], anomalies appear in the middle of the band for E-plane scanned single-polarized arrays of bilateral TSAs, which are due to the presence of parallel plate modes in between the TSA plates. This type of resonance was also found to occur

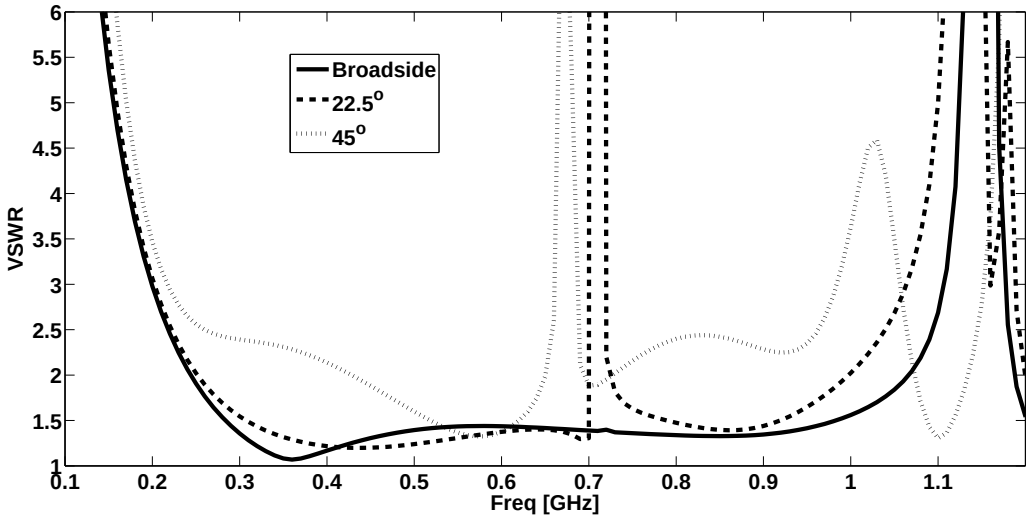

Figure 4.18: VSWR for an E-plane scanned dual-polarized array.

for an E-plane scanned single-polarized array of "bunny-ears". As shown by Wunsch and Schaubert [65], these resonances can be suppressed by placing metallic cross walls at the locations where normally cross-polarized elements are placed.

In [66], one justifies the presence of an impedance anomaly that was found to occur because of the undesired radiation from the differential feed lines used to excite an array of dipole antennas. These anomalies are not observed for the present design.

In [67] a similar impedance anomaly for a planar array of symmetrical crossed dipoles has been identified and analyzed rigorously for the fields that are incident from grazing angle (in the E-plane). However, the polarization of the incident E-field vector is not the same as in the present work, where the array grid has been oriented perpendicular to the E-plane scans. Nonetheless, the anomalies seem to have a common origin with the one explained in this work, where it is explained how currents couple to each other due to the presence of neighbouring elements and how this leads to the undesired increase in the reflection coefficient.

In the work of Hay and O'Sullivan [61], an anomaly was found for a finite array of connected patches with features also observed in the present differentially-fed "bunny-ear" arrays[1]. Fig. 4.19 shows the topological equivalence between the two structures where p is the geodesic path length along the edges of the conducting surfaces between the feed points of the elements of orthogonal polarizations. In [61] it is demonstrated that the frequency at which a differential-mode resonance occurs can approximately be predicted by the geodesic path length p being half a wavelength. In the present study, the geodesic path length p equals half a wavelength

[1] When awaiting for the *IEEE* revision of the journal paper where most of this study is contained [53], the authors' attention was called to a paper by Hay and O'Sullivan [61] published after the original submission of [53] where an equivalent situation is studied albeit for a different type of structure.

at 615 MHz, so the prediction is reasonable since the resonances are observed around 650-700 MHz (the exact value depends on the scan angle cf. Fig. 4.18). Another property of this resonance is that it is characterized by anti-phase common-mode currents on the feed conductors of connected orthogonally-polarized elements. In the following it is shown that this also occurs for the present structure.

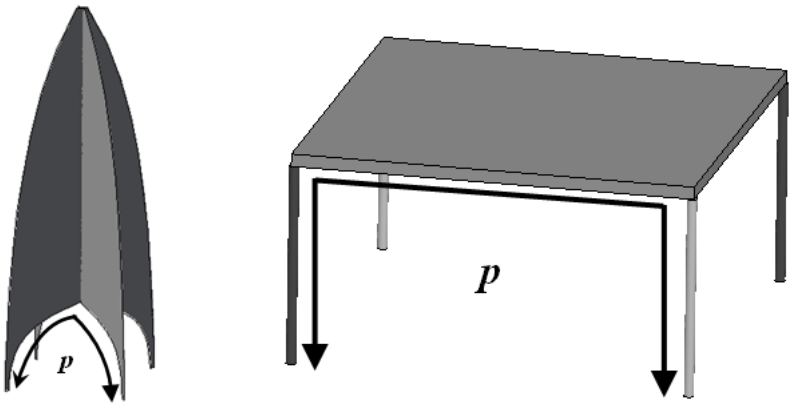

(a) TSA elements (b) Patches

Figure 4.19: Topological equivalence between the connecting surfaces of (a) the TSA elements and (b) the patches in [61]. Each drawing represents 4 half elements (2 per polarization). The geodesic path length along the conducting surfaces between the feed points of the elements of orthogonal polarizations is p.

By removing the ground plane, only the two conductors are retained (the two arms of the antenna) as well as the balanced feed lines. It was observed that, for the present frequency range and for off-broadside scan angles, where the electrical symmetry is broken, only evanescent common-mode currents are supported along the differential feed lines. However, in the presence of a third conductor, such as a ground plane, a common-mode signal can be supported by the feeding structure which may lead to severe differential-mode scan impedance resonances. From Fig. 4.18 one can observe for what frequencies impedance anomalies occur, and how these are dependent on the scan angle.

The surface current distribution on the antenna elements has been analyzed for a number of scan angles/frequencies, thereby revealing the presence of common-mode currents on the differential feed lines. It has been confirmed that both odd- and even-modes can exist on ground-plane-backed "bunny-ear" arrays, and these modes are excited differently, depending upon the frequency and scan angle. To analyze the various modes of the currents, a series of plane waves were forced to be incident to the open-circuited array while the induced current distributions were monitored. Fig. 4.20(a) shows the current distribution at 500 MHz, where it can clearly be observed that the odd mode dominates over the even mode. The even-mode current distribution in Fig. 4.20(b) is strongly pronounced for an incident plane wave at 22.5^o

at a frequency of 710 MHz, which is the frequency where a scan impedance anomaly occurs on transmit for the differentially-fed array scanned to 22.5^o in the E-Plane (see Fig. 4.18). Fig. 4.20 therefore suggests that when the differential-mode scan impedance is at resonance, a common-mode current is supported by the structure, which may be excited strongly depending upon the type of excitation source used on transmit, or incident plane-wave field applied on receive. The presence of such a common-mode current at the anomalous frequency was also observed for an array of disconnected balanced antipodal Vivaldi antennas [68].

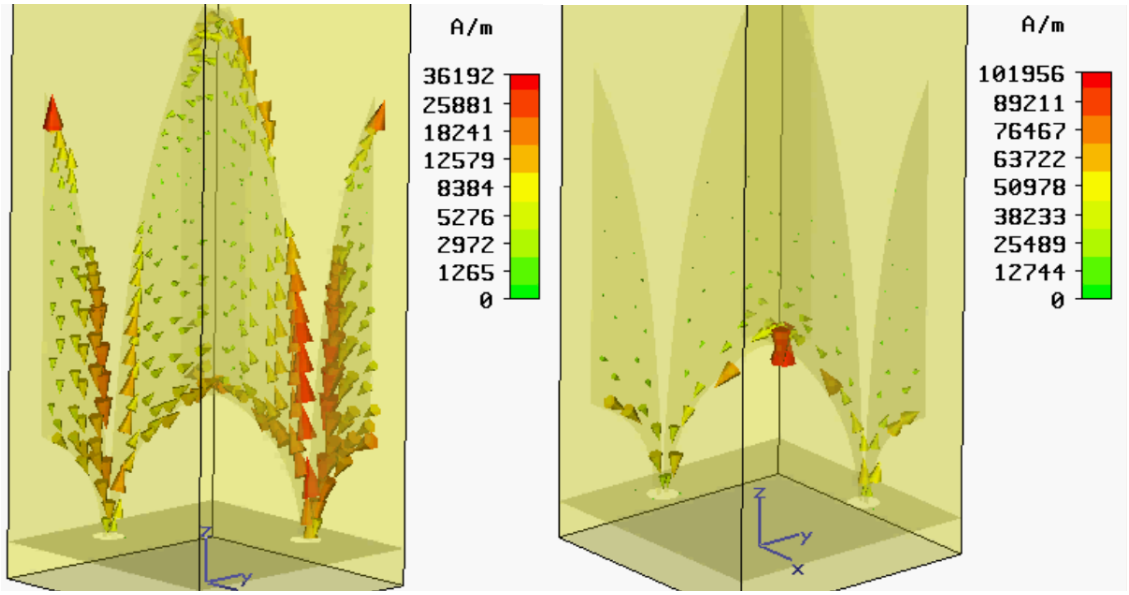

(a) Currents at 500 MHz (b) At the anomaly frequency

Figure 4.20: Distribution of the surface currents for the unit cell at (a) 500 MHz and (b) at the anomaly frequency with an incident plane wave at 22.5^o.

At this moment it is not clear how differential LNAs can be optimally noise matched to both types of scan impedances, given the fact that they are strongly related to each other. Despite the fact that a SKA-like station ($>$ 100,000 elements [38]) would largely behave as an infinite planar array, the common-mode anomaly in Fig. 4.18 could also appear at broadside, due to a slight asymmetry brought about by the finiteness of the array. An example is the case of a large array of disjoint subarrays, or a focal plane array with offset beams (non-symmetric excitations). Anomalies may also appear as observed by Schaubert, Craeye, and Boryssenko when introducing other types of asymmetries in the structure, e.g. [69, 70].

To mitigate the common-mode problem, i.e. to eliminate the resonance in the differential-mode scan impedance, it is essential to analyze first the propagation of the corresponding surface currents through the structure at resonance. Fig. 4.20(b) illustrates that the common-mode current is confined to the bottom region of the "bunny-ear" antennas instead of along the tapered slot as for the differential-mode

current, and that the phase progression of the common-mode current starts at one arm of the antenna and ends in the arm of the orthogonally connected antenna. This specific problem is only present in dual-polarized arrays like the ones in Fig. 4.2. Note that these characteristics were also observed for an array of connected patch antennas [61].

In this section a technique to avoid these impedance anomalies, while keeping the orthogonally-polarized elements in place, is presented. The comprise solution is based on using two resistors per element, each of them connected between one of the feeding lines and the GND plane, thereby dissipating a small part of the common-mode currents (see Fig. 4.21). Even though the proposed solution may seem very noisy for a radio astronomical application, it will be shown that the noise increment is only minor and therefore not of a big concern. The use of reactive elements has not shown to yield the desired change in the scan impedance characteristics.

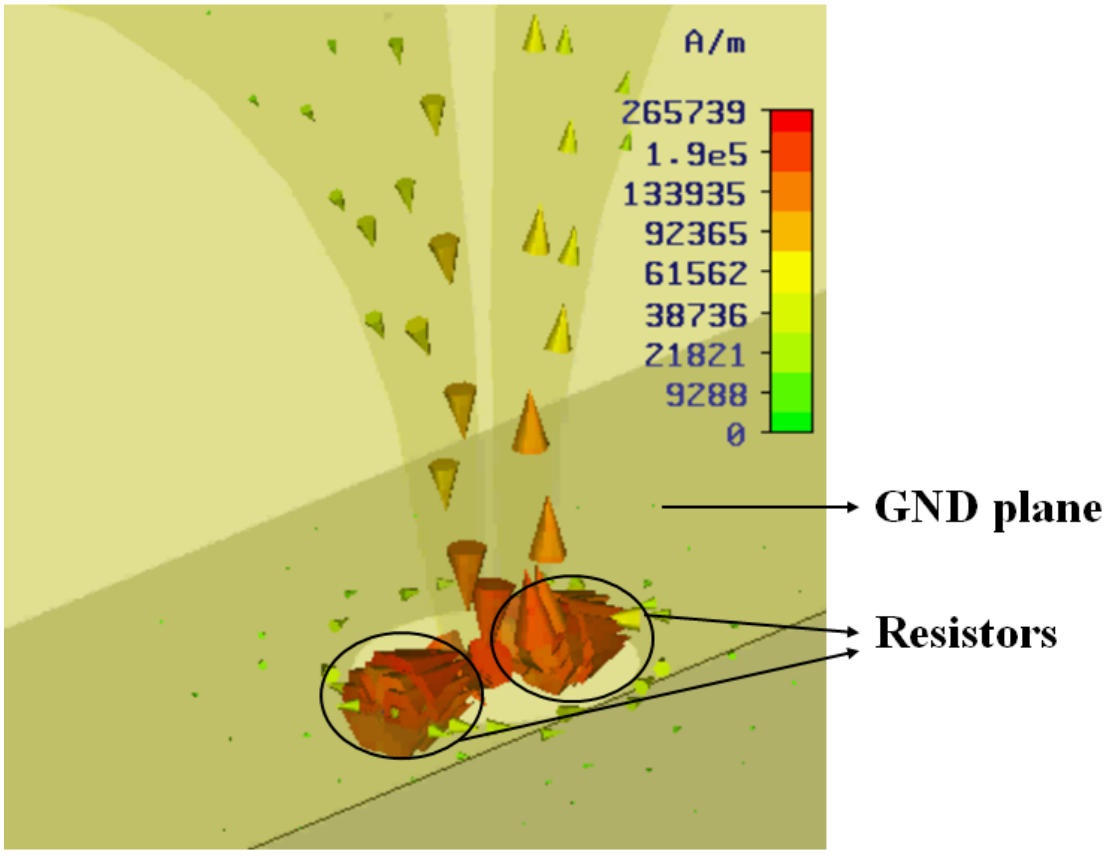

Figure 4.21: Distribution of the surface currents for the unit cell after placing two resistors of 3 kΩ from each arm of the antenna to the ground plane. The current is shown at the anomalous frequency of Fig 4.20(b).

Fig. 4.21 visualizes the two resistors that have been used to partly suppress the even mode current, thereby allowing the odd mode to dominate. The propagation path of the current reveals that it is sufficient to place the resistor in only one of the polarizations. However, in order to preserve the symmetry of the array they are

applied to both polarizations.

A parametric study was undertaken to examine the effect for various resistor values on the the antenna input impedance. For this purpose, the VSWR was computed and is plotted in Fig. 4.22 for a 45^o E-plane scan. Clearly, the differential VSWR increases when low-valued resistors are used since then the differential generator becomes almost short-circuited. The differential impedance match readily improves upon raising the resistor level by only tens of ohms. In fact, the even-mode currents keep sufficiently suppressed up to 3 kΩ, while still a good overall matching level can be realized (VSWR $<$ 2.5). The differential scan impedance anomaly appears for resistor values larger than that, implying that the structure can support even-mode currents with significant amplitude. The case of raising the resistor values to infinity is equivalent to the case of removing the resistors (open circuit), so that the original anomalous differential VSWR is obtained allowing both the common-mode and the differential-mode currents to propagate. The common-mode current is more strongly suppressed than the differential-mode current since the resistors are seen in series for the differential-mode excitation, whereas they are in parallel for the common-mode excitation (factor 4 difference, for DC). The best trade-off is reached when the resonance in the differential scan impedance becomes sufficiently suppressed while the overall impedance characteristics remain almost unaffected. This optimum resistor value was found to be near 3 kΩ.

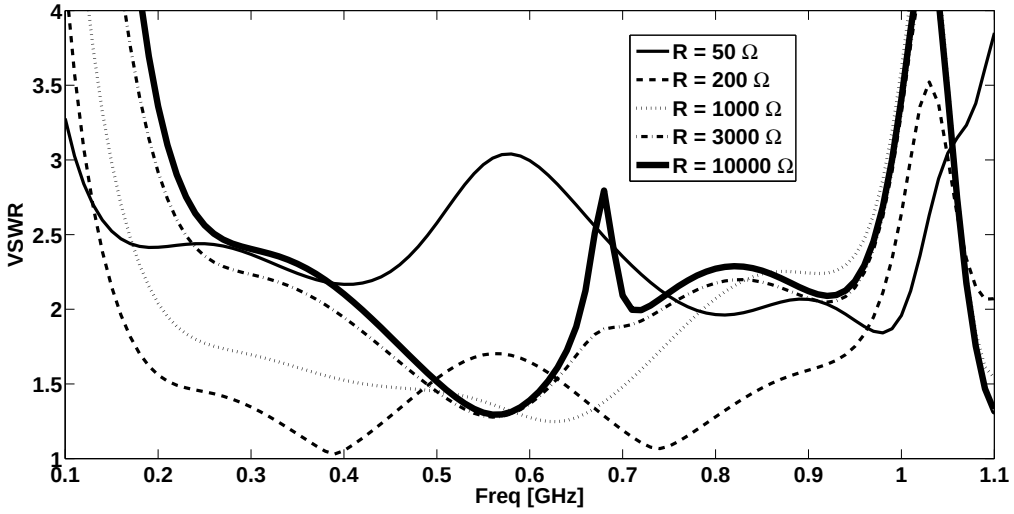

Figure 4.22: VSWR for a 45 ^{o} E-plane scan for R = 50 Ω to R = 10 kΩ.

The differential VSWR for three different E-plane scans is presented in Fig. 4.23, both for 1 kΩ and 3 kΩ resistors. The H-plane scans are not shown, because these are only weakly dependent on the resistors. Note that for 3 kΩ resistors, the matching level in the band remains acceptable, even for large scan angles, and the results are very similar to those obtained for a resistor value of 1 kΩ.

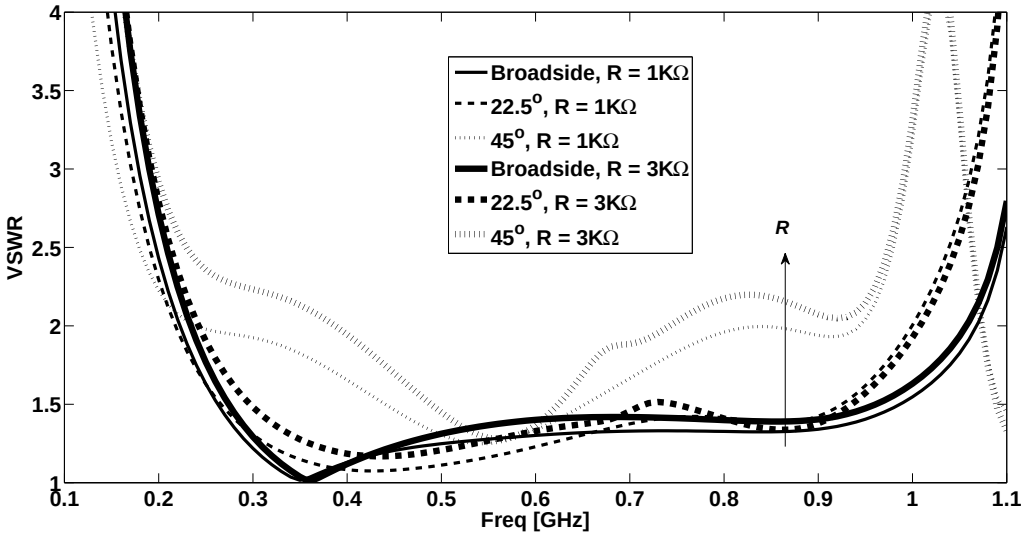

Figure 4.23: VSWR for an E-plane scan, for R = 1 kΩ and 3 kΩ.

A thermal noise study of the proposed method is of interest when the lumped resistors are placed across the antenna conductors in front of the amplifying circuits[2].

The antenna impedance matching degrades by increasing the resistor values beyond a certain point as the effect of the lumped resistors decreases (Fig. 4.22), i.e., on transmit, a lower power is delivered to these resistors because of a low power transmission factor from the differential antenna port to the resistors. Likewise, on receive, only a small part of the thermal noise that has been generated by these resistors will be observed at the antenna port, due to this low transmission factor. In the following, the power absorption and associated noise temperature contribution will be accounted for through the radiation efficiency η_{rad} of the unit cell.

For receiving (phased-array) antennas, it is common to define the system sensitivity as the ratio of the effective aperture area A_{eff} to the total system noise temperature T_{sys}:

$$\frac{A_{eff}}{T_{sys}} = \frac{ab \cdot cos(\theta) \cdot \eta_{rad}}{\eta_{rad} \cdot T_{sky} + (1 - \eta_{rad}) \cdot T_{amb} + T_{LNA}} \tag{4.10}$$

The sensitivity formula, Eq. 4.10, is in accordance with Eq. (22) in [71], except that η_{rad} is here the radiation efficiency of the unit cell. It is important to mention that the sensitivity is herein referred to the input of the LNA (output of the antenna). The effective area is defined through the antenna's available output power which is the available incident power to the unit cell area reduced by the radiation efficiency. By definition, perfect polarization match and conjugate match terminated array

[2]The two loads in Fig. 4.21 may be realized by the input impedance of two single-ended LNAs which are used to form a differential balanced LNA, and like that, its noise temperature contribution is accounted for by the S-parameters and noise properties of the LNAs (antenna is regarded lossless).

elements are assumed so that, in the absence of grating lobes, the effective area of a unit cell is given by the numerator of Eq. 4.10, where θ is the direction of incidence measured from the normal to the array plane and ab is the physical size of the unit cell (cf. [26]).

Apart from a power loss, the sensitivity also decreases due to an increase in the total system noise temperature caused by a decrease in the radiation efficiency. The temperature T_{amb} is the physical antenna temperature, which equals (for non-cooled antennas) the typical ambient temperature of 290 K, and T_{LNA} is the noise temperature of the amplifier in the active scenario (with the source impedance of the LNA equal to the scan impedance), and T_{sky} is the noise temperature contribution of the sky. For generality, both T_{sky} and T_{LNA} are set to 0 K in order to be able to quantify the noise increase due to only the absorption losses of the antenna.

Fig. 4.24 demonstrates how the sensitivity per unit cell area increases when the value of the resistors increase. It is remarkable to observe that the sensitivity does not exhibit a resonance as e.g. observed in the VSWR port characteristics in Fig. 4.22, even not for 10 kΩ resistor values. This is due to the fact that the radiation efficiency itself is free of resonances since it only quantifies the relative dissipated power loss which may not change much when the port impedance is at resonance. On the contrary, T_{LNA} is expected to increase as a result of a noise mismatch to the anomalous differential source/antenna impedance, but this effect is dependent on the specific LNA design which is not discussed in this chapter.

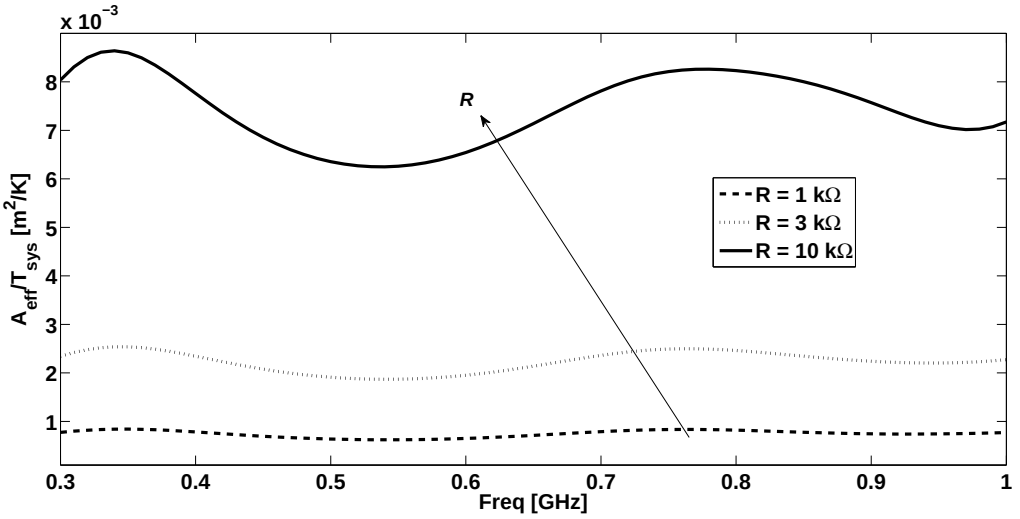

Figure 4.24: System sensitivity per unit cell for a 45^o E-plane scan for three resistor values. The unit cell area is $ab = 30.6\text{x}10^{-3}$ m^2.

In addition to the sensitivity curves, the noise temperature contributions for resistor values of 1 kΩ, 3 kΩ and 10 kΩ are presented in Fig. 4.25 for completeness. To be consistent with the noise temperature specifications used for the SKA, as well as with Y-factor measurements for antennas, it is common to refer the system noise

temperature in front of the antenna system (the sky), while the system sensitivity is a ratio and therefore independent on the chosen reference point. The corresponding noise temperature formula is in Eq. 4.12. It is concluded that a compromise is necessary, i.e., increasing the resistor value leads to a lower noise temperature (Fig. 4.25) but degrades the impedance match (Fig. 4.22). A good compromise was found for a resistor value of 3 kΩ, for which both a low noise temperature (Fig. 4.25) and a resonant-free E-plane scan impedance is realized which has a good matching level (Fig. 4.23). Fig. 4.25 demonstrates that the use of 3 kΩ resistors leads to a minor increment of the total system noise temperature, i.e. not more than 10 K, which is reasonable considering the 7 K ($\sim$ 0.1 dB loss) that has been specified for the aperture array antennas in [45].

$$T_{LNA} = T_{sky} = 0K \tag{4.11}$$

$$T_{sys} = \frac{(1 - \eta_{rad})}{\eta_{rad}} \cdot T_{amb} \tag{4.12}$$

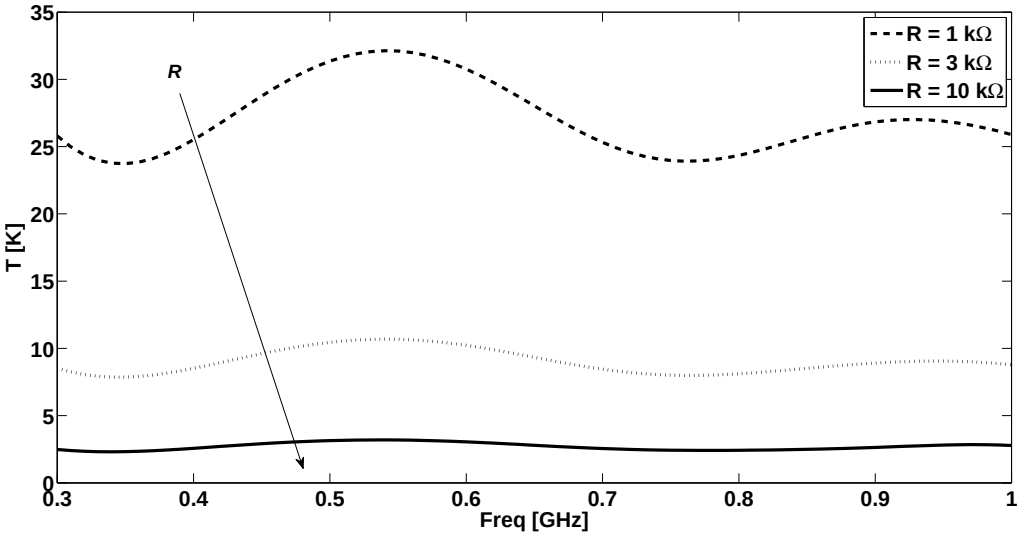

Figure 4.25: System noise temperature for a 45^o E-plane scan for three resistor values.

4.4 Design example

With the knowledge acquired in the parametric analysis of section 4.2, and by applying the impedance anomaly elimination technique proposed in section 4.3, a dual-polarized array from 300 MHz to 1 GHz has been designed and optimized to cover a scan range up to 45^o, thereby meeting the specifications of the SKA [38]. In order to minimize the cost, the element width is chosen to be as large as possible so that

the number of amplifiers per square metre is minimized while in-band grating lobes are prevented from occurring.

The final geometrical parameters of the structure are shown in Table 4.3, and the final results for several E-plane and H-plane scans are plotted in Fig. 4.26 and Fig. 4.27. A resistor of 3 kΩ has been used to obtain these results. No E-plane impedance anomalies are present and the VSWR is lower than 2.5 over the entire operational frequency band, as well as for all scan angles up to 45^o.

Table 4.3: Parameters of the optimized array.

Width	L_{in}	B_{in}	L_{out}	B_{out}
168 mm	350 mm	0.008 mm^{-1}	77 mm	0.055 mm^{-1}

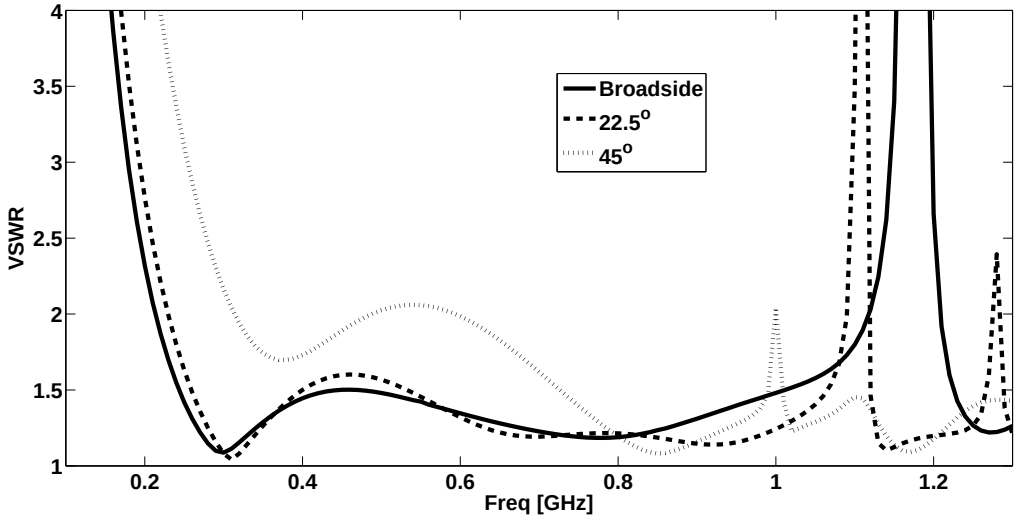

Figure 4.26: Differential VSWR for various scans in the H-plane.

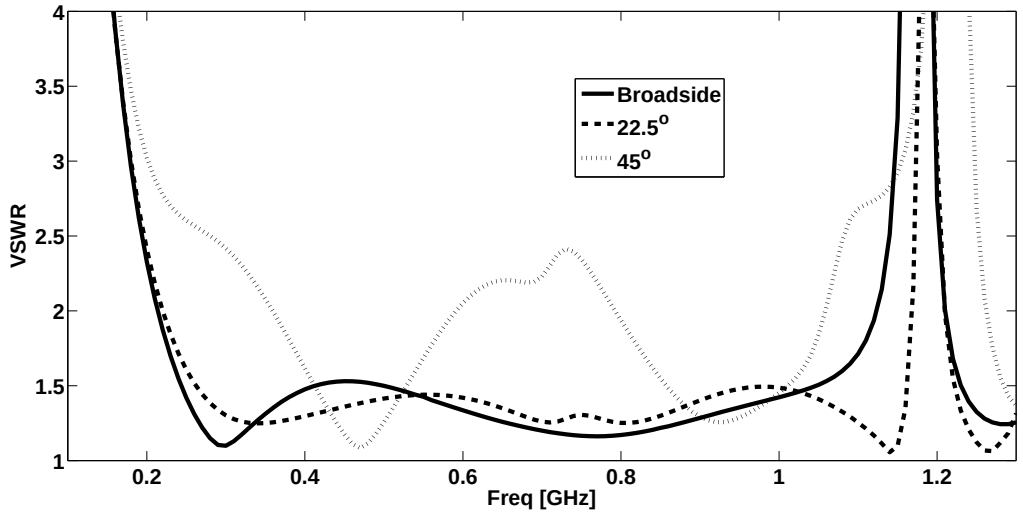

Figure 4.27: Differential VSWR for various scans in the E-plane.

4.5 Prototype

As a result of the studies presented in this chapter, a prototype of FIDA^3 (see Fig. 4.31) has been built and measured. Fig. 4.28 shows a view of the tile. The Aluminium antennas are supported by a FR4 frame which holds them in the right position. The amplifiers are placed under the metallic ground plane and connected to the antennas through a circular hole in the plane.

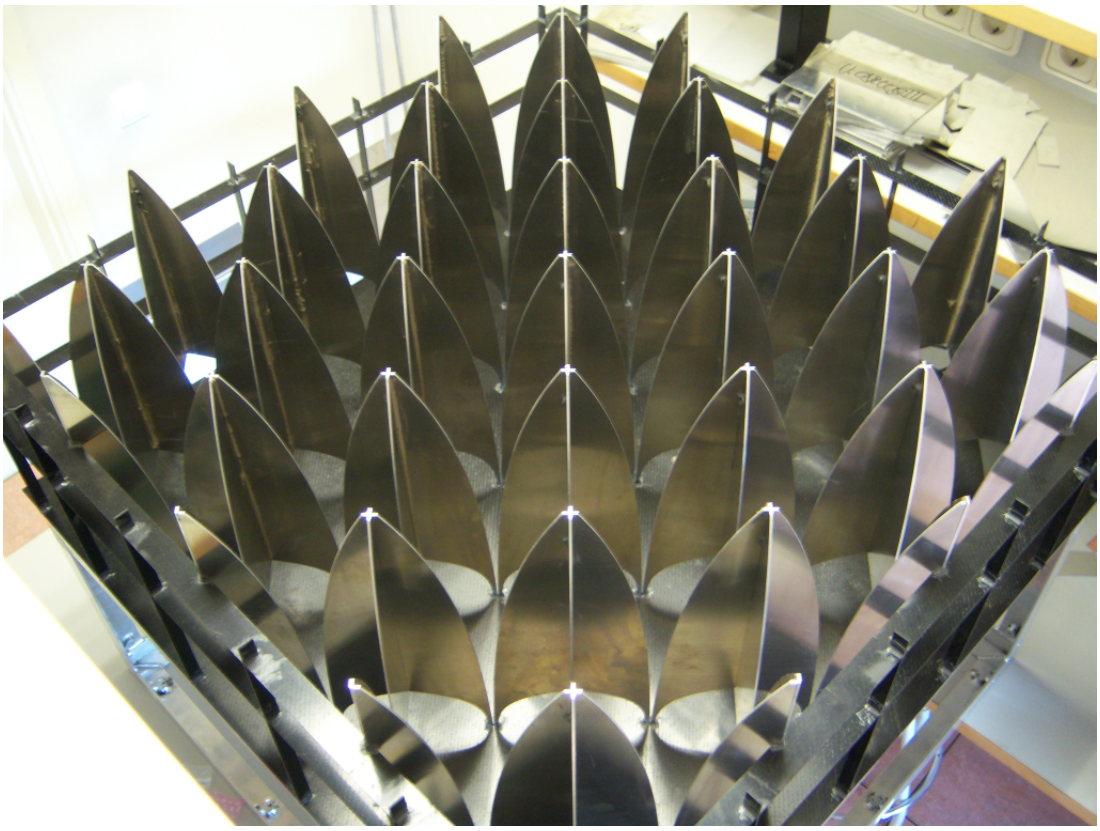

Figure 4.28: Tile of FIDA^3.

The results for an E-plane and H-plane scan of the finite tile are presented in Fig. 4.29 and Fig. 4.30. It is apparent how even for such a small array, the infinite-by-infinite array design has delivered a good performance.

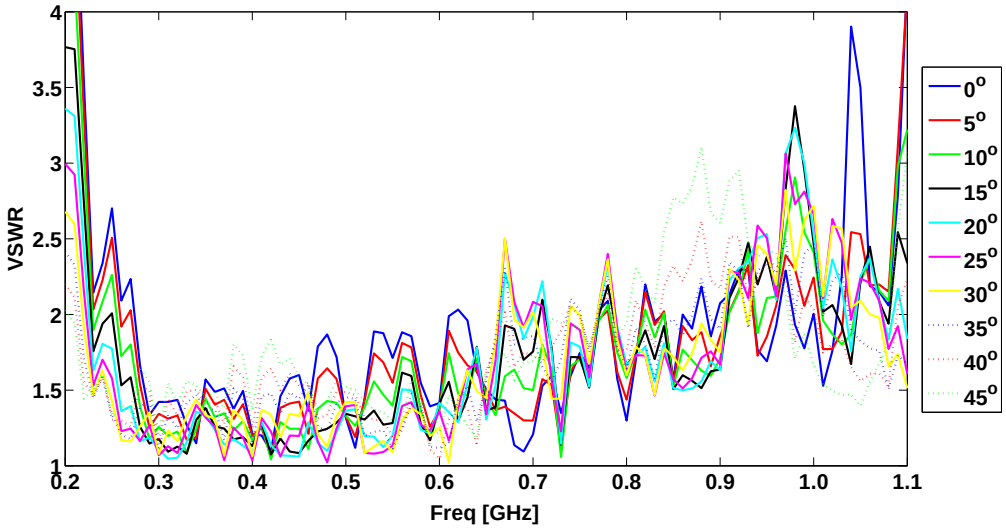

Figure 4.29: Measured differential VSWR of the central element for various scans in the E-plane.

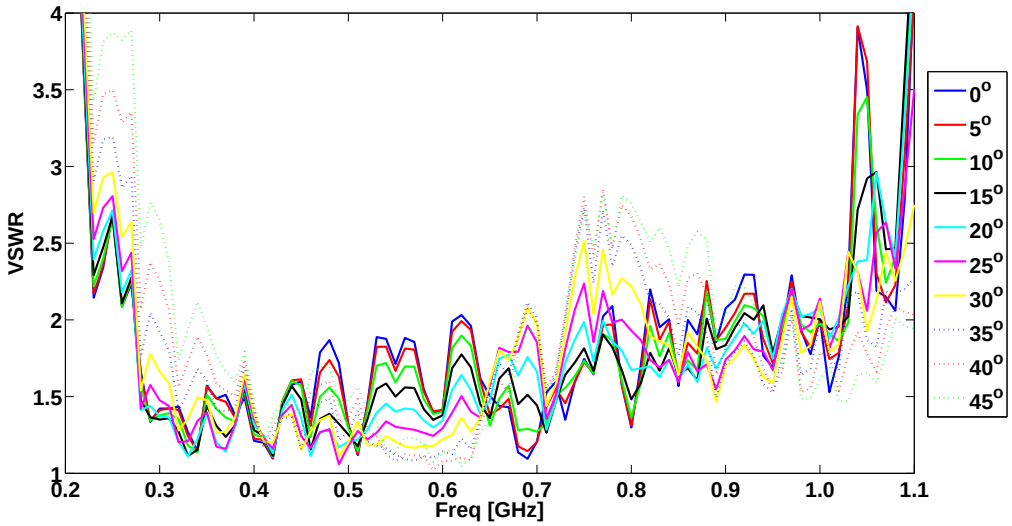

Figure 4.30: Measured differential VSWR of the central element for various scans in the H-plane.

The work related to the the design and construction of differential LNAs for the FIDA[3] prototype have been carried out by the student of the *Universidad Carlos III de Madrid* Oscar García Pérez. Fig. 4.32 has been extracted from a presentation by Oscar given in ASTRON at the end of his internship there, summarizing the properties of 3 different DLNA prototypes.

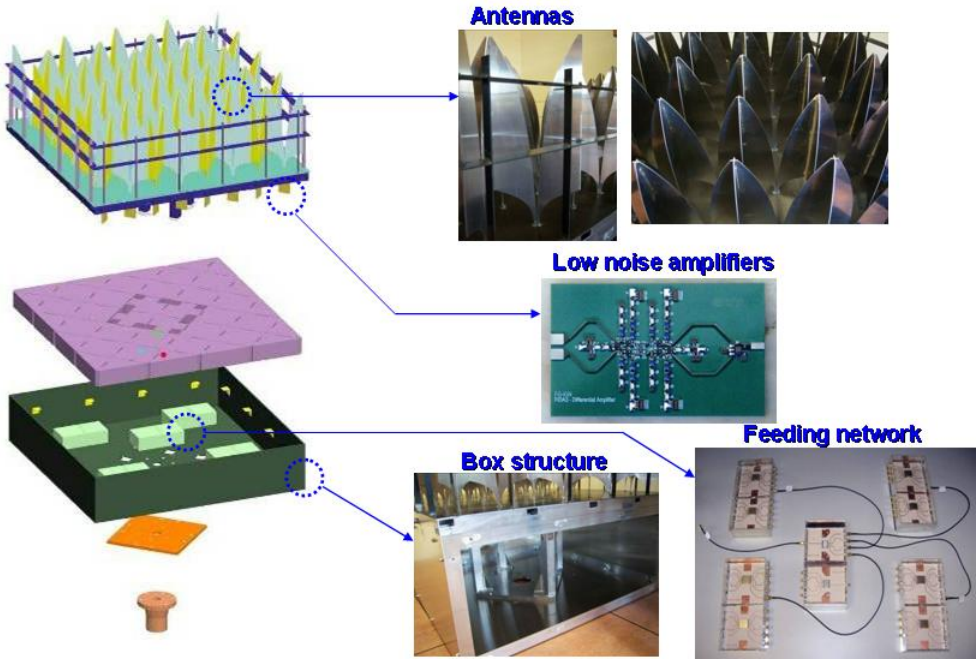

Figure 4.31: Prototype scheme.

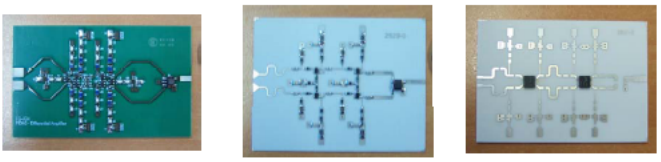

Prototype	FIDA3 LNA	Prototype 1	Prototype 2
Bandwidth	300MHz-1000MHz		
Source impedance	150Ω (diff.)		
Gain	>27dB	>26dB	>36dB
Noise temperature	**<53K**	**<40K**	**<30K**
Noise resistance (R_n)	<23Ω *	<13Ω *	<8Ω *
Input reflection	**<-1.8dB**	**<-6dB**	**<-1.1dB**
Output reflection	<-13.0dB	<-6dB	<-5.5dB
Common mode rejection	>23dB	>23dB	>24dB

* simulation

Figure 4.32: LNAs prototypes.

During the noise measurement of the FIDA[3] amplifiers, it was found that the noise was higher than expected (see Fig. 4.33). This was due to the mismatch between the antenna elements and the amplifiers because of a failure in the pair LNA-antenna design process. In an array environment, the presence of other antennas and its loads has an effect on the active input impedance of every antenna. Because the amplifier input impedance is, in effect, the load impedance of every antenna, this must be carefully design along with the optimum noise impedance of the amplifier. If the input impedance of the amplifier is not taken into account in the design process, the active input impedance of every antenna in the array will be different to the

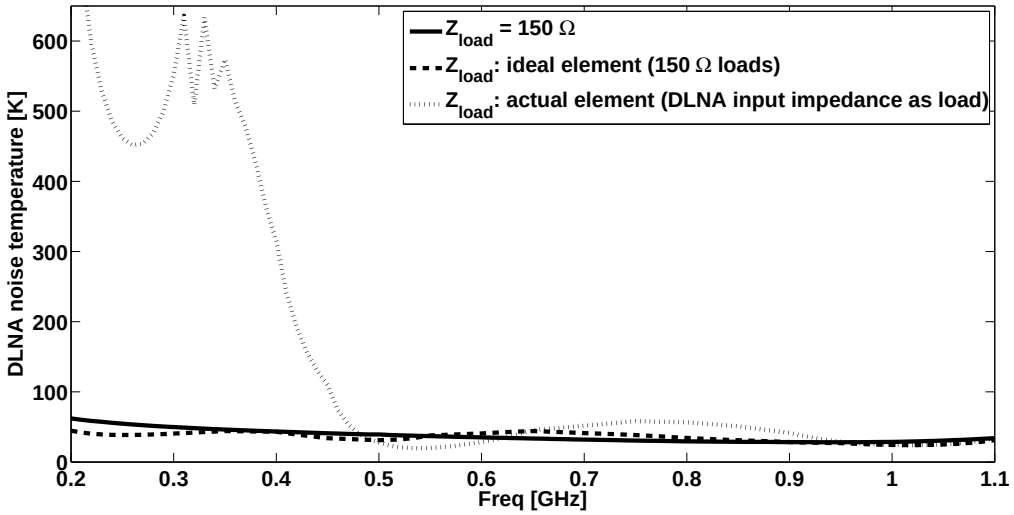

Figure 4.33: Noise temperature of the DLNA.

simulated active input imepedance (it is typically assumed a fixed load impedance for every antenna of the infinite-by-infinite array). Therefore, the minimum noise will not be achieved as the optimum noise impedance of the amplifier was calculated assuming a different antenna impedance. This was solved and differential amplifiers with noise temperature lower than 52 K in the whole band have been measured.

4.6 Conclusions and future work

A dual-polarized array of differentially-excited elements ("bunny-ear" antennas) has been analyzed through a parametric study in order to demonstrate the effect of various antenna element geometries on the scan impedance characteristics of an infinite-by-infinite array.

In addition, an E-plane differential-mode scan impedance anomaly has been identified, which is caused by an even-mode that is supported by the differentially-fed antenna array in the presence of a third conductor, such as a ground plane. It has been shown that the impedance resonance can be suppressed by a (low-loss) balancing-dissipation technique using a pair of resistors. The associated reduction in system sensitivity has been analyzed and shows that the increment of the corresponding antenna noise temperature is less than 10 K for 3 kΩ resistors at room temperature (290 K).

When passive resistors are used to prevent the differential-mode scan impedance anomaly from occurring, a compromise is necessary between: (i) the reduction in effective area as well as an increase in system noise temperature due to a reduced radiation efficiency, and; (ii) the realization of a resonant-free differential antenna impedance (source impedance) for achieving an optimal noise match between the

differential LNAs and the antenna elements. The latter depends on the specific LNA design which has not been discussed in this chapter.

A final optimized antenna design has been presented meeting the specifications of the SKA project while keeping the potential manufacturing cost as low as possible. The operational frequency band ranges from 300 MHz up to 1 GHz, the array is dual-polarized, and steerable up to +/- 45^o.

The major contribution of the designed array, compared to the available technology, is that it is dielectric-free and differentially-fed, which, despite the associated anomalies, allows the connection of the antenna elements to the LNAs/beamforming network directly, which themselves are realized in differential technology. The losses and bandwidth limitations associated with the use of a balun and the necessary dielectric layer/layers are therefore eliminated, improving the overall performance of the radio telescope by increasing the sensitivity (namely reducing the noise budget) while reducing the cost. Note that, at room temperature, the improvement in system noise only occurs if the noise added by the balun is more than the noise added by the second transistor needed for a differential LNA, which is typically the case.

As a result of this effort, a prototype tile (FIDA^3) has been built and measured and it has been delivered to the SKADS project as part of the Spanish contribution to the development of state-of-the-art technology for the SKA telescope. It will be then considered as a potential candidate for the final design of the telescope, which will be fully operational soon after 2020. Furthermore, one contribution to a workshop [42], as well as three conference proceedings contributions [50, 51, 52] and one journal paper [53] have been published.

In future, several lines of work will be considered:

1. To elaborate upon the relationships between the common-mode and the differential-mode scan impedances, as well as the optimal matching conditions that apply to differential antenna and LNA designs. Numerical simulations and measurements of prototypes should indicate what is the relation between both modes and how this has an effect on the matching with the rest of the receiving chain. Also, alternative methods to remove the scan impedance anomalies present in here should be explored.

2. To Study the effect of the finiteness of the array. Even if the array is regarded as infinite due to the large number of elements present in each station of the telescope, it is important to analyze the effect of different realizations of the array. For example, if this is regarded as a collection of tiles, what is the effect of connections between tiles. It will also be necessary to quantify the edge effects for large stations. This should be done by simulating infinite-by-finite arrays and large finite arrays, making use of numerical-method-based codes

such as [19]. This information is especially valuable for calibration purposes. The results of such an analysis would useful to elaborate on the necessity of adding, for example, dummy elements in the outside of the array in order to reduce the effect of the finiteness of the array.

3. To characterize the cross-polarization patterns of the array for all angles and scan angles. The next phase of the SKA project will be focused on developing calibration systems, which in most cases will require a very accurate knowledge of the cross-polarization patterns.

4. An analogue ultra-wideband beamforming network will be necessary if the conversion to digital happens at a later stage. Further undesired anomalies could arise from specific designs of the LNAs and the beamforming network and these must be properly characterized as in the present study.

In this and the previous chapter I focused on the design of dense array antennas to cover the high frequency band of the aperture array proposal for the SKA (300 MHz to 1 GHz). In the next chapter, I will elaborate on the design of sparse arrays for low-frequency radio astronomy (frequencies from 70 to 450 MHz).

Chapter 5

Ultra-Wideband Aperture Array Element Design for Low-Frequency Radio Astronomy

21^{st} century Radio Astronomy at frequencies below 1 GHz will be dominated by arrays of thousands or millions of elements in configurations which are dense or sparse, regular or random, delivering data to powerful digital back-ends. High performance, specified by parameters such as the effective aperture and system noise temperature, will be crucial to achieve the ambitious survey speeds and sensitivities demanded by astronomers. In this chapter the different trade-offs and difficulties in the design of ultra-wideband array antenna elements for these radio telescopes at frequencies below 500 MHz are analyzed. Bandwidths of 7:1 are desired while using low-profile elements to keep the overall cost within the budget.

The contents of this chapter have been published or made public in three conference proceeding contributions [72, 73, 74]. As well, one journal paper has been sent for publication [75].

5.1 Introduction

Next-generation radio telescopes, such as the SKA, are currently being designed using aperture arrays [9]. The use of phased antenna arrays in radio astronomy is not new. One such a radio telescope, designed and built in Cambridge UK, and coupled to fast receivers, was the essential technology which led to the discovery of pulsars by Hewish and Bell. Only now, however, are computer and processing technologies becoming available which will enable us to realize an instrument on the scale of the SKA. One particular science objective is to study the formation of the earliest galaxies which ionized the cold neutral hydrogen pervading much of the

Universe at that time. This point in the evolution of the Universe is called the epoch of re-ionization, and it occurred at a sufficiently early time that the signals from the intrinsic 21-cm line of neutral hydrogen are "redshifted" into the frequency range from 70 MHz to several hundred MHz when observed today. One part of the SKA design therefore calls for an ultra-wideband antenna array able to operate from 70 to 450 MHz. There are clear cost savings if this frequency range can be covered using a single antenna element design.

The chapter is structured as follows. In Section 5.2 the main trade-offs and limitations in the design of ultra-wideband antenna elements for aperture arrays are discussed. Section 5.3 focuses on the system noise for a single receiver chain of an aperture array, and in Section 5.4 the current state-of-the-art in large array characterization is summarized. Section 5.5 comprises a design study of an ultra-wideband bow-tie antenna element in an aperture array environment, emphasizing those characteristics important for the SKA. The conclusions to this chapter and the future lines of work can be found in Section 5.7. I did the work presented in this chapter in the Cavendish Laboratory, University of Cambridge, UK, after I started my work there in 2007.

5.2 Trade-offs and limitations.

5.2.1 Current and planned instruments

As explained in section 2.4.2, there are several new-generation instruments planned or in current use for radio astronomy which have phased antenna arrays. Some examples are LOFAR [76], the MWA [77] or the LWA [78]. The SKA-AAlo [8] will be the next big step in low-frequency radio astronomy. Despite the advantages of aperture arrays, several drawbacks are also present which are analyzed here. Aiming for ultra-wideband array performance (up to bandwidth ratios of 7:1) in impedance and radiation pattern (stable embedded antenna element patterns with beam widths up to 90 degrees), requires the array designer to have a specific knowledge of the radio astronomy application.

5.2.2 System noise

The noise signal generated in an array antenna element from galactic radiation dominates over the noise generated by the front-end amplifier for frequencies below 200 MHz (this is discussed in more detail in Section 5.3). The sensitivity of a low-frequency radio telescope can be adopted as the primary figure of merit which, for the instruments mentioned above, is the ratio of the effective aperture to the system noise temperature (A_{eff}/T_{sys}) [38]. The overall array gain, G, (directly related to

the effective aperture by the formula $G = 4\pi\ A_{eff}/\ \lambda^2$) is dominated by the number of elements in each array, while the embedded antenna element gain is constrained by the desired beam width which must be large enough to see much of the sky above the instrument. The system temperature is also affected by the impedance mismatch and any losses between the element and the amplifier, as well as by the sky noise at lower frequencies.

5.2.3 Mutual coupling

The effects of mutual coupling between closely-located elements may bring about undesired effects in the performance of the array [12]. Typically one sees the appearance of narrow-band anomalies which vary with the array geometry and type of antenna element. The anomalies appear only in certain pointing directions (scan angles) and frequencies. Several authors have addressed this problem in phased arrays of one and two polarizations for different types of elements, for example dipoles [67] and tapered slot antennas [15, 69], and several mathematical models have been proposed with formal explanations for each particular case [15, 64]. These include the presence of surface waves in a substrate cancelling the principal array mode [14], the energy transfer between common and differential modes of operation [61, 53], and the cancellation of the principal array mode by a horizontally-travelling wave created in the array structure [15]. The anomalies have an effect upon the active reflection coefficient and the system noise temperature. In radio astronomy applications, cosmic signals are averaged over bandwidth and time. It is important therefore need to analyze the effects of the anomalies in each particular application, as to remove them completely is usually expensive both in terms of performance and cost [65].

5.2.4 Array beam

The array beam (or *station beam* for an interferometer) has a major influence on the usefulness of the instrument. Not only does it need to be accurately characterized at every possible zenith angle, mode of operation, and frequency in order to be able to calibrate the array, but it must also provide a smooth and stable instrument response as the angle changes, so as to be able to track an object for long periods. Side-lobes must be taken into account as the sky distribution is not uniform. For example, a weak side-lobe pointing directly at the Sun will surely wreck the observations of a weak radio source in the main beam. One can decide whether to accept a certain level of side-lobes within a restricted range of angles, or whether to have them spread out more-or-less uniformly across the whole sky. Array beams are formed digitally in most cases using the signals digitally sampled from individual antenna

elements, but partial or total analogue beam forming are also being considered by the radio astronomical community. The expected effects, which depend on the array configuration, are: 1) In regular close-packed arrays (i.e. element separations up to half a wavelength or slightly larger as shown later in the chapter) the effects of mutual coupling are strong but confined within narrow frequency bands and ranges of scan angle. 2) Regular sparse arrays (in which the average spacing between elements is of the order of and greater than a wavelength) still suffer from the negative effects of mutual coupling, but less so as the inter-element spacing increases. Side-lobes are also more troublesome. 3) Non-periodic sparse arrays (e.g. random sparse arrays) also normally suffer from the effects of side-lobes, but because of the irregular grid, the effects are distributed across the parameter space, increasing the noise overall, but still providing a useful sensitivity at all zenith angles [79]. 4) Thin-sparse arrays use a sampling function to remove certain elements in the array to improve the side-lobe level in specific cases. However, such arrays are still based on regular grids so the effects of the side-lobes are more pronounced in certain frequency bands and angles.

5.2.5 RFI (Radio Frequency Interference)

Radio frequency interference is a major problem in low-frequency radio astronomy, especially for applications such as measuring interplanetary scintillations in which a short integration time is essential, and renders some bands, such as the FM band, unusable in practice. Solutions based on post processing are dominant in solving this problem [80]. In some circumstances, however, the presence of RFI can be useful, for example as a calibration signal, but it must always be taken into account when designing aperture arrays for radio astronomy. (One might, for example, decide to realize a design in which the anomalies caused by mutual coupling all fall into frequency bands excluded for use for radio astronomy by continuous RFI.) It is relevant to note that some RFI occurs naturally, such as the broad-band interference from electric discharges. These pose a significant threat to the successful scientific exploitation of a given instrument and should be taken into account at the earliest stages of design and choice of site.

5.2.6 Characterization

As explained in Section 5.4, the large area associated with instruments of this type suggests that infinite array simulators may provide useful guidance in the design process, neglecting the edge effects present in any practical realization. Several commercial simulation packages are available for regular arrays [16, 17]. However, when the array is not regular these packages can, at best, provide only an approxi-

mate guide as to what to expect. Therefore, great efforts are being made to develop codes capable of simulating arrays of arbitrary size and sparseness, with the aim of obtaining full electromagnetic characterization of arrays with dimensions of hundreds of wavelengths [19]. In this chapter, existing commercial software has been used taking into account where the simulations are likely to have been adversely affected.

5.2.7 Limited budget

Every project to build a new radio telescope has a limited budget. The largest arrays of many thousands of elements require the design of low-profile ultra-wideband antennas which are inexpensive, easy to build, and easy to maintain. The choice of cheap but resistant materials is crucial, so also is the proper design of protection systems, such as radomes and lightning protection.

5.3 System noise in low-frequency radio telescopes

The system noise temperature of the SKA must be minimized in order to achieve the desired sensitivity. The specifications for the SKA are shown in Table 5.1 [8]. At the low-frequency end of the band (sub 200 MHz), the minimum value of T_{sys} is limited by galactic radiation [81]. The reason for this is that the system noise temperature is the sum of contributions from the front-end amplifier, losses in the antenna element and in the connection between the array antenna element and the amplifier, and the noise generated in the array antenna element from the sky.

Table 5.1: SKA specifications for sensitivity at a zenith angle of 45 degrees.

Frequency	*Sensitivity*	T_{sys}
100 MHz	4000 m^2/K	Sky noise limited
800 MHz	10000 m^2/K	Receiver noise limited (~36 K)
1 GHz	10000 m^2/K	Receiver noise limited (~35 K)

In the designs discussed in Section 5.5, a model of the system noise accounting for the contribution of all three sources have been assumed, given by

$$T_{sys} = T_{ant} + T_{LNA} \tag{5.1}$$

where

$$T_{ant} = \eta_{rad} \cdot T_A + (1 - \eta_{rad}) \cdot T_{amb} \tag{5.2}$$

It is assumed that the antenna element is connected directly to the amplifier input terminals. In this case, the noise temperature from the antenna at the input to the

amplifier, T_{ant}, can be subdivided into the noise created by the physical temperature of the lossy parts of the antenna, T_{amb}, and the noise received from the sky and surroundings, T_A. These two noise temperatures are weighted by the attenuation factor, η_{rad} (the radiation efficiency). T_{LNA} is the amplifier noise temperature and it is highly dependent itself on the match between the antenna and the amplifier. This equation can be regarded as an equivalent single receiver chain model for the array case.

5.3.1 Antenna noise temperature, T_A

The antenna noise term, T_A, is a convolution of the array beam with the sky at a specific frequency, and can be simply understood by the following equation:

$$T_A = \frac{\iint\limits_{4\pi} |F(\nu,\theta,\phi \mid \hat{r_0})|^2 \cdot T_{sky}(\nu,\theta,\phi) \cdot sin\theta \cdot d\theta \cdot d\phi}{\iint\limits_{4\pi} |F(\nu,\theta,\phi \mid \hat{r_0})|^2 \cdot sin\theta \cdot d\theta \cdot d\phi} \tag{5.3}$$

For an array, the radiation pattern is given by the $|F|^2$ term which can be calculated using the appropriate software (e.g. CST [16], HFSS [17], MATLAB [82], etc.) The sky temperature distribution is given by the term T_{sky} To get a general idea of overall array performance, a generalized spectral model can be used for the sky brightness. Medellin [83] describes such a model using radiative transfer theory which gives the sky temperature distribution as a function of frequency and zenith angle, θ. Whilst this type of sky model is useful, a more appropriate option when considering specific array designs is to use the measured sky brightness. There are currently a number of sky surveys including the 178 MHz survey of Turtle and Baldwin [81], the 408 MHz of Haslam et al. [84], the 1.4 GHz of P. Reich and W. Reich [85, 86] and the 2.3 GHz of Jonas, Baart and Nicolson [87] which are suitable for the frequency range of the SKA. The advantage of using the measured sky is that given scenarios can be tested, such as those where bright sources pass over the side-lobes of the beam.

5.3.2 Receiver noise temperature, T_{LNA}

The noise generated within the receiver chain (including the beam forming network), T_{LNA} , originates mainly within the first amplifier to which the array antenna element is connected. If this is of sufficiently high gain, noise generated further down the receiver chain can be ignored. At low frequencies, it is easy to ensure that amplifier noise should be much smaller than the noise coming from the sky, as the latter increases sharply with decreasing frequency, as shown in Fig. 5.1. In this situation, both the antenna and amplifier performance can be relaxed, whilst still keeping an

acceptable value of T_{sys} . For a receiver chain comprising an antenna connected to an amplifier, the noise temperature, T_{LNA}, may be modelled with the following equation [88] (a detailed description of how to compute T_{LNA} accounting for the beam-forming network can be found in [89]):

$$T_{LNA} = \left(\left(F_{min} + \frac{R_n}{\mathbb{R}\left(1/Z_{ant}\right)} \cdot \left| \frac{1}{Z_{ant}} - \frac{1}{Z_{opt}} \right|^2 \right) - 1 \right) \cdot T_{amb} \tag{5.4}$$

Here, F_{min} is the minimum noise figure of the amplifier, R_n is the noise resistance of the transistor, Z_{opt} is the impedance to which the amplifier should be connected for minimum noise, Z_{ant} is the impedance of the antenna element (the active impedance if the antenna element is in an array environment) and T_{amb} is the ambient temperature, typically 290 K. Note that the input impedance of the amplifier must be also carefully designed, even though it is not explicitly visible in the above equation, because every element in an array is, in practice, loaded by the input impedance of the amplifier.

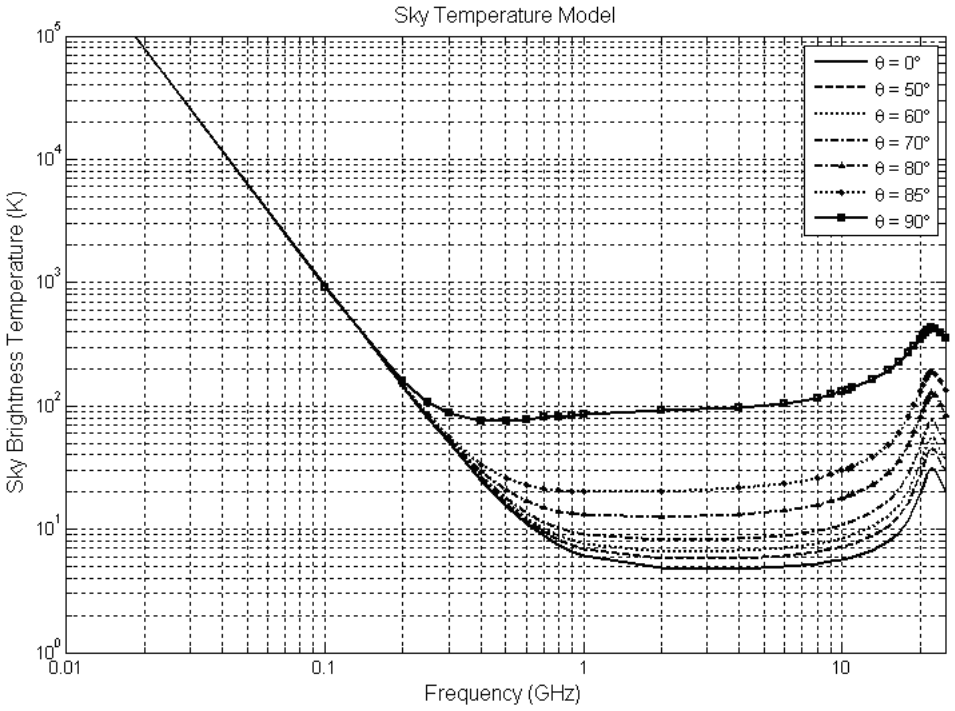

Figure 5.1: Sky temperature model based on [83].

5.4 Characterization of ultra-wideband arrays for low-frequency radio astronomy

Analyzing large phased arrays with dimensions of hundreds of wavelengths is a challenge and, in practice, may be a limiting factor in the design of the new generation of radio telescopes. The commercial packages available, based on classical numerical methods such as the Method of Moments (MoM), Finite Differences in Time Domain (FDTD), or Finite Element Method (FEM) [10, 90] are limited with respect to the maximum number of elements they can handle at once.

For these astronomical super stations, an infinite array analysis would be possible, but this would ignore the truncation effects at the edges of the array [12] and would assume that the array had a regular configuration of identical elements. As stated in Section 5.2, the use of irregular configurations may be the choice for the SKA-AAlo, but currently it is still not possible to do a full wave simulation of this type of array, unless the antennas are 'canonic elements' whose characteristics can be described with an equation [12]. Even in that case, as soon as a ground plane is added, or the elements are more complex than a thin wire, a computational challenge arises, both in computing times and memory requirements. In this section, that part of the state-of-the-art in the simulation of massive arrays known by the me is summarized; the landscape in computational electromagnetics applied to large problems is widening everyday.

In principle, a conventional frequency-domain FEM formulation can be used, no matter what size of array is contemplated; however, this would result in a system with millions of unknowns, and a supercomputer would be required to solve it. Domain decomposition methods, such as the dual primal Finite-Element Tearing and Interconnecting method for electromagnetic analysis (FETI-DPEM) [91, 92], can significantly speed up the simulation of large arrays. In FETI-DPEM, the computational domain is divided into non-overlapping sub-domains, where a partial solution of the field is evaluated using a direct FEM solver. The tangential continuity in the interfaces between sub-domains is assured by using Lagrange multipliers. An iterative algorithm can then be used to solve the reduced-order interface problem.

Time-domain formulations can also be used, and these are of particular interest when analyzing broadband structures, though it is not as straightforward as for the frequency-domain formulations described above. Typically, in time-domain simulators, direct solvers of the equation system are preferred since, despite having to solve the equation matrix in every time step, one can potentially re-use the factorization of previous steps. However, in the case of extremely large problems, this factorization may use up too much memory and require too great a processing speed. A domain decomposition technique is therefore used in small sub-domains,

which then can be solved in parallel. There are also other domain-decomposition formulations which do not require solving a global problem [93, 94], such as the Dual-Field Domain-Decomposition (DFDD) time-domain FEM, where each sub-domain is locally evaluated using a pre-factorized matrix and the results are then passed to the neighbour sub-domains to be used in the next computation step. Again, this method takes advantage of arrays where many sub-domains are identical to speed up the computation.

Method of moments-based techniques, which have been widely used to solve medium-sized scattering and radiation problems, may also be usable in modelling large structures such as phased arrays. In the method of moments, the surface to be modelled is divided into sub-domains and the current over each one of these is expressed as a weighted low-level basis function. For large problems, one can take advantage of so-called Characteristic Basis Functions (CBF), also called Macro Basis Functions (MBF), which are high-level basis functions defined over relatively large domains, different from the domains where the low-level functions are defined. The CBFs can be obtained from the currents induced on the low-level sub-domains by a set of excitations and can be expressed in terms of the low level basis functions. The advantage is that now the number of unknowns in the system of equations is dependent on the number of CBFs, much lower than the number of low-level basis functions required in a typical problem. In [95], the CBFs are generated from the fields induced by the exciting wave on a sub-domain (called primary CBFs) and from the mutual coupling between various sub-domains (called secondary CBFs). This approach is dependent on the form of the excitation. But, as detailed in [96, 97], if one uses a spectrum of plane wave excitations to generate the CBFs, the set of functions becomes independent of the excitation. Another way to reduce further the number of unknowns in the system is based on the concept of expansion waves. The idea is to express the incident and scattered fields of an isolated array element in terms of a few expansion functions [98]. Other methods include the Synthetic-Functions approach (SFX) [99], and the Sub-Entire-Domain function method (SED) [100].

The MoM efficiency can be improved further by combining a method such as one listed above to reduce the number of unknowns, with an algorithm to speed up the computations to fill the reduced matrix. An example of this is the Adaptive Integral Method (AIM) [101] or the Adaptive Cross Approximation algorithm (ACA) [18]. ACA is relatively easy to implement and does not require a priori knowledge of each impedance matrix. It is a purely mathematical trick to do block factorization of the rank-deficient sub-matrices. The Fast Multipole Method (FMM) [102] and variations are also being used to speed up the matrix filling, such as the Multi-Level Fast Multipole Algorithm (MLFMA) [103]. Here, the entire volume is decomposed

into first-level cubical regions which generate higher-order regions when grouped. The MLFMA stores only the near-field terms of the coupling matrix while computing efficiently the far-field interactions in an iterative process.

In a recently published book, Zhang and Sarkar [104] develop both parallel in-core and out-of-core EM integral equation solvers to make use of all computer resources. New methodologies and strategies are also presented to increase the efficiency of MoM codes.

Finally, techniques such as sub-gridding [105] allow MoM methods to be applied to non-uniform arrays, e.g. random arrays. The sub-gridding technique uses the smooth behaviour of the interactions between CBFs to interpolate between them and also to compute rapidly the patterns of the non-uniform array once the coefficients have been calculated. In [19], this work is extended providing a powerful tool to simulate large arrays, such as might be used in the SKA. The latest is part of the work I did during my thesis and it is explained in more detail in chapter 6.

5.5 Low-profile aperture array antenna element design

The most important figure of merit for low-frequency radio astronomy instruments is the system sensitivity, defined as A_{eff}/T_{sys} (Eq. (22) in [71]). In the present study, A_{eff} is obtained by simulating the gain of a unit cell of the infinite regular array, G_{cell}, when this is phased to point in a given direction r_0= (θ_0,ϕ_0). (Each unit cell contains a single bow-tie antenna element.) The system temperature, T_{sys}, as described in Section 5.3, accounts for the contributions from the sky brightness, losses suffered before the amplifier, and electronic noise generated by the amplifier. These are also dependant on r_0.

$$\frac{A_{eff}}{T_{sys}} = \frac{(\lambda^2/4\pi) \cdot G_{cell}}{\eta_{rad} \cdot T_{sky} + (1 - \eta_{rad}) \cdot T_{amb} + T_{LNA}} \tag{5.5}$$

Perfect polarization match is assumed. Furthermore, power mismatches are not taken into account in the sensitivity formula as they would affect equally to both numerator and denominator.

In this section, an ultra-wideband low profile bow-tie antenna element as in Fig. 5.2 is analyzed to investigate its viability for use in the SKA. The element is made of Perfect Electric Conductor (PEC) and it is placed a quarter of a wavelength at the highest frequency of interest (166 mm at 450 MHz) above a ground plane to optimize the beam shape of the element [11]. The use of a ground plane avoids uncontrolled and lossy reflections in the actual ground and makes the element sensitive only to the radiation coming from the sky. However, it is important to notice that the

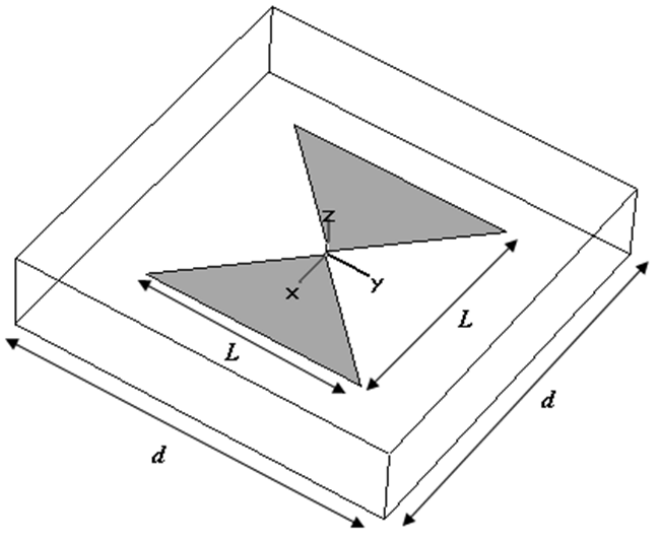

(a) Unit cell

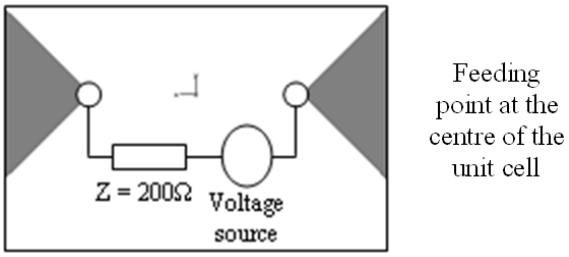

(b) Feeding point

Figure 5.2: Simulated unit cell of the regular array. a) Unit cell. The element type is a Bow-Tie antenna placed 166 mm above a ground plane. b) The model of the feed.

wideband nature of the antenna will now be limited by the presence of the ground plane. The main effect is that the impedance at the low end of the frequency band is reduced. Fortunately, as mentioned before, the presence of the sky noise allows the designer to relax the matching constrain at those low frequencies without losing much sensitivity. A regular infinite phased array of the proposed elements is simulated using the periodic boundaries approach of a commercial software package based on FD-TD [16]. The effects of changing the element size and the inter-element spacing are investigated for 0^o and 45^o scan angles in the E- and H-planes. The broadside scan is analyzed in the first place assuming a fixed element and a variable size of the unit cell (therefore of the inter-element spacing, d). The range of spacings considered is shown in Table 5.2.

The impedance plot is shown in Fig. 5.3, where the trend with increasing d is marked by the arrows.

Of more interest is the result shown in Fig. 5.4, which displays the receiver temperature, calculated using equation 5.4, and the effective aperture of the unit

Table 5.2: Unit cell parameters – analysis of the inter-element spacing, d.

d	L
Set to $\lambda/2$ at frequencies from 70 to 300 MHz in steps of 10 MHz	Fixed to 50 cm ($\lambda/2$ at 300 MHz)

cell, computed using the numerator of equation 5.5. Calculation of the receiver temperature is made on the assumption of an idealized amplifier with the parameters shown in Table 5.3.

Table 5.3: Idealized amplifier parameters.

F_{min}	R_n	Z_{opt}	Z_{amp}
0.2	10 Ω	200 Ω	200 Ω

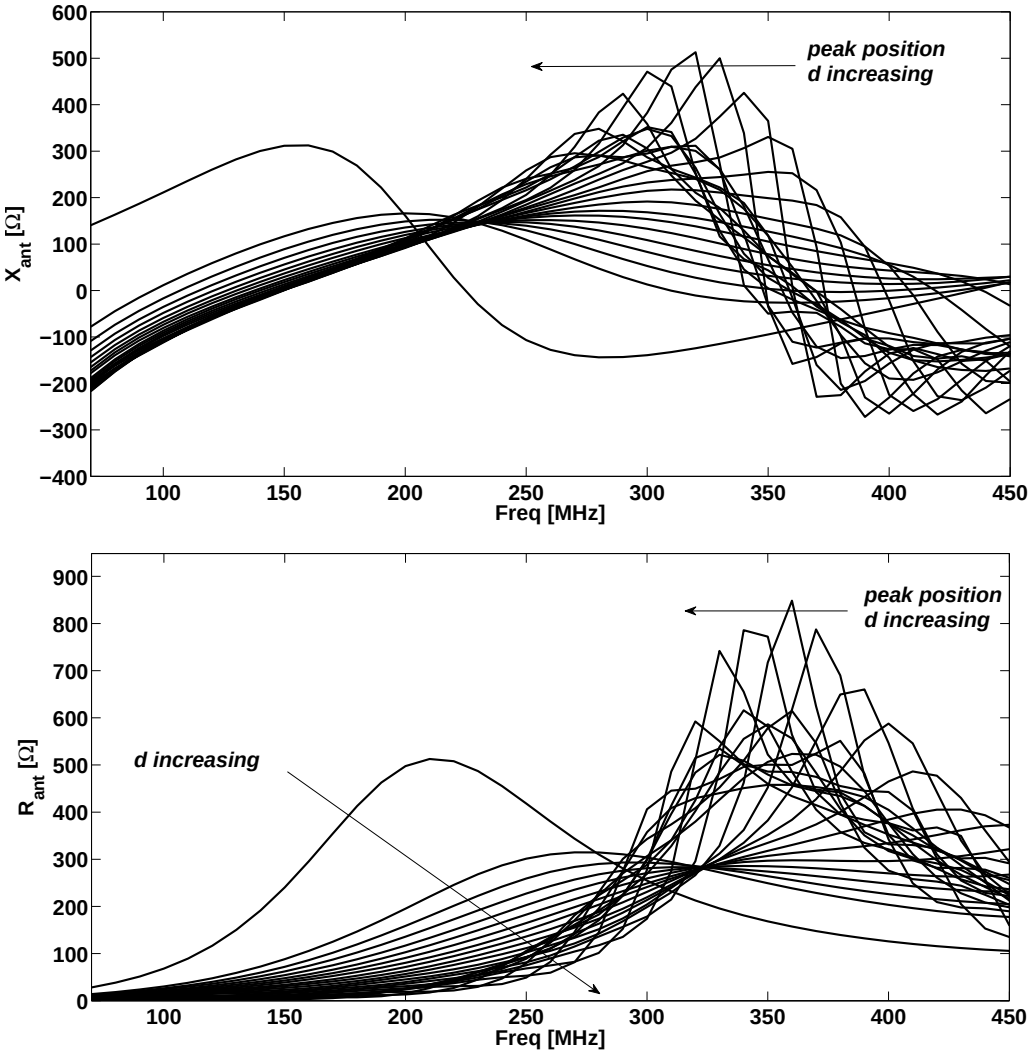

Figure 5.3: Simulated unit cell active impedance at 0^o scan angle. The inter-element spacing, d, is set to be half a wavelength at the given frequency (see Table 5.2).

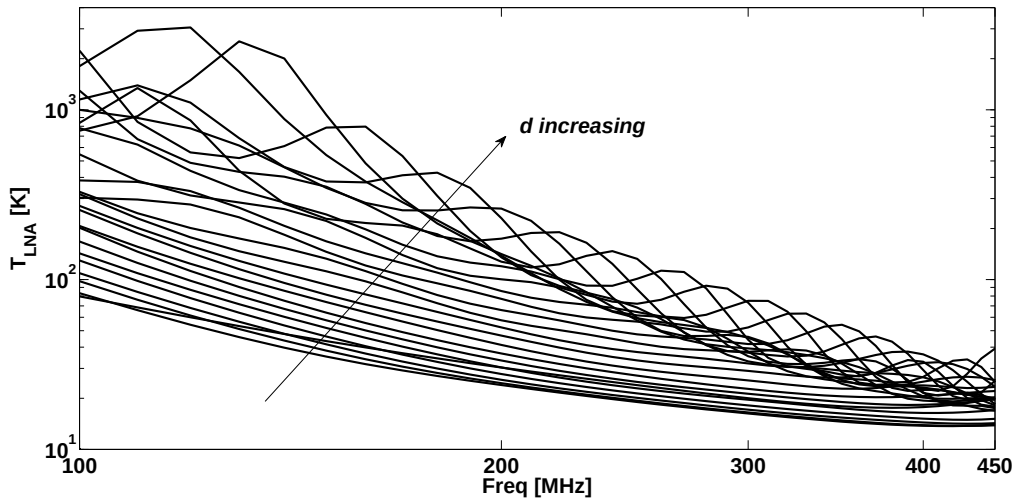

(a) Receiver temperature

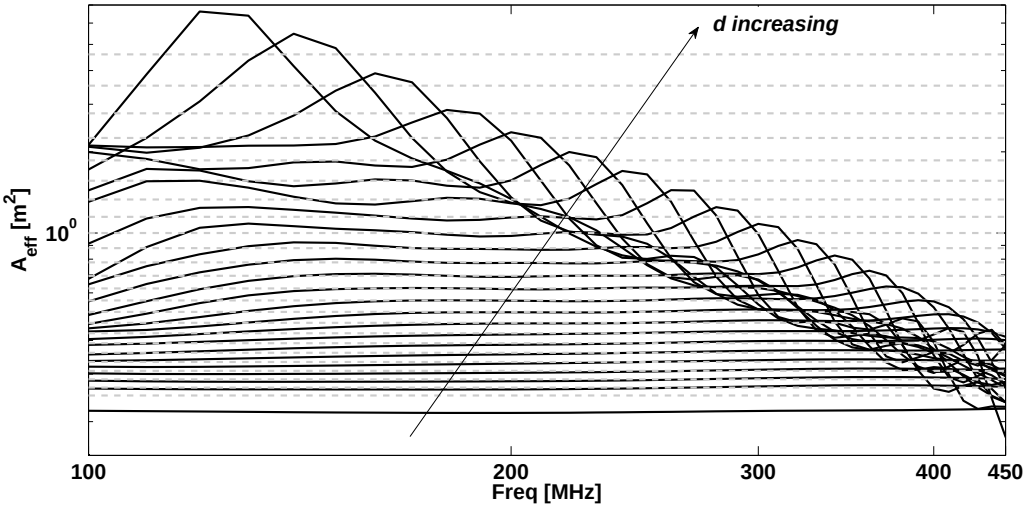

(b) Effective aperture

Figure 5.4: Simulated unit cell (a) receiver temperature and (b) effective aperture (physical size in dashed lines) at 0^o scan angle for different inter-element spacing distances, d.

Fig. 5.4 clearly shows how the receiver noise temperature decreases for arrays where the elements are closely-packed, a beneficial influence of mutual coupling. One can distinguish two clear regions in the effective aperture plot (Fig. 5.4 (b)), the first from low frequency up to that at which the spacing is just below λ. In this region, the effective aperture grows with d, as the physical size of the unit cell is increasing. The second region is for frequencies at and above that at which the spacing is λ. Here, the effective aperture decreases with increasing frequency at a rate approximately equal to half of the square of the wavelength. This effect has already been reported for an array of dipoles [79]. These two regions could be regarded respectively as the dense and sparse regimes of the array. It is important to note that both regions are separated by a small in-between band which sits somewhere in between those

frequencies at which the spacing is $\lambda/2$ to λ. For the present case, in the sparse regime the effective aperture is slightly better than $\lambda^2/2$. In Fig. 5.4 (b) one can observe how, in the dense regime, the effective aperture of the unit cell converges to its physical size, d^2. Also apparent in Fig. 5.4 (b) is the increase in efficiency of the unit cell for more closely-packed configurations. This is because the small bow-tie element is incapable of illuminating the whole of the physical area of a large unit cell. Nevertheless, it is still possible to get a relatively good effective aperture even with a relatively small bow-tie element. In Fig. 5 the appearances of grating lobes are marked with arrows. They show up in the infinite array simulations when the spacing between elements is a multiple of the wavelength due to the appearance of a high order Floquet mode.

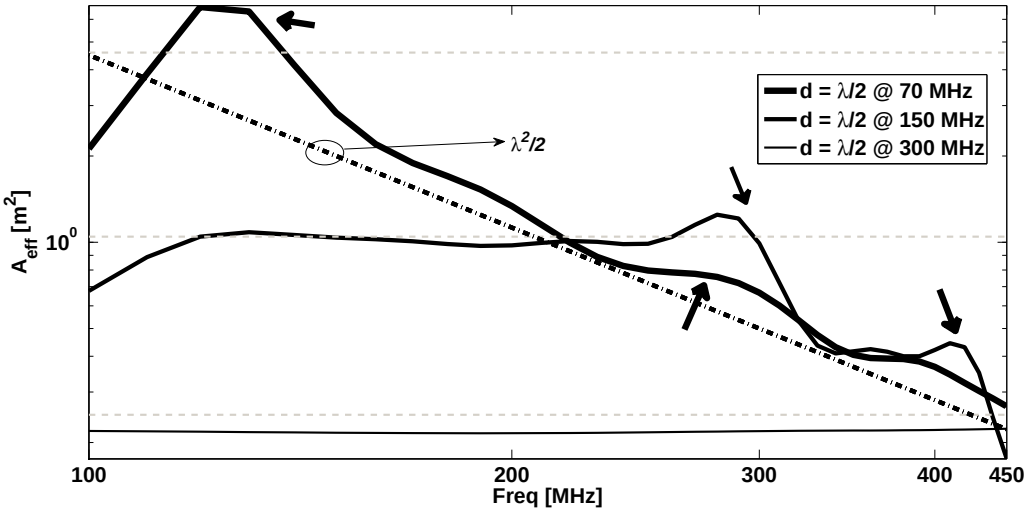

Figure 5.5: Simulated unit cell effective aperture (physical size in dashed lines) at a scan angle of 0^o for different inter-element spacing distances, d.

Finally, the sensitivity at 0^o scan angle is calculated assuming the idealized amplifier parameters of Table 5.3 and a uniform analytical sky brightness following the model given in [83] as in equation 5.6 (the frequency f is in GHz). The choice of a uniform sky model makes sense in the context of the analysis of a unit cell, where the shape of the pattern itself does not strongly affect how much power is collected by the antenna element from the whole sky.

$$T(f) = 1.691 \cdot f^{-2.751} + 4.875 \tag{5.6}$$

From the sensitivity plot in Fig. 5.6 one can conclude that a sparse array, where the effective aperture increases as $\lambda^2/2$ and it is not limited by the physical size of the unit cell, offers better sensitivity at low frequencies than a closely-packed array, despite the higher system temperature. At the high frequency end of the band, the effective aperture of the array has an upper boundary of $\lambda^2/2$. However, the

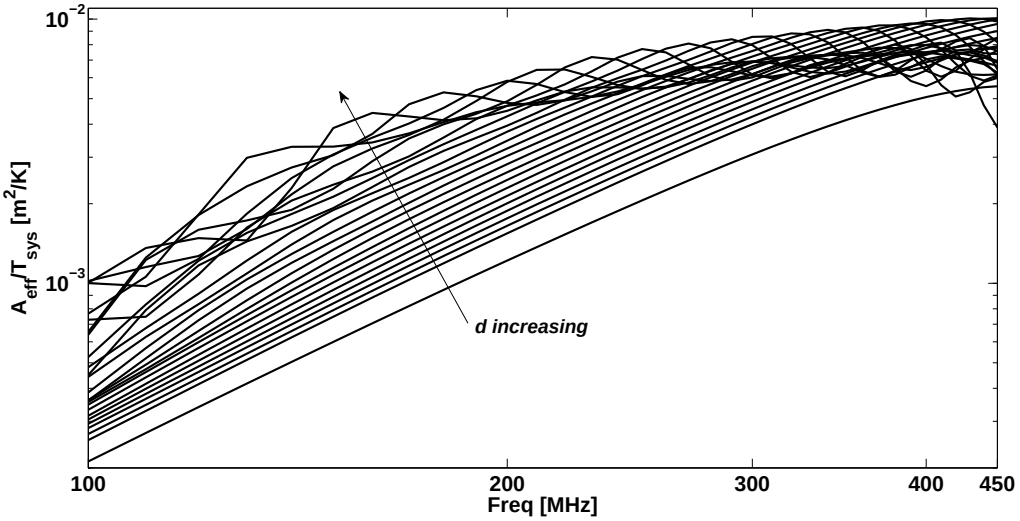

Figure 5.6: Simulated unit cell sensitivity at broadside scan for different inter-element spacing distances, d.

matching is still slightly better for more closely-packed arrays which results in a better sensitivity. This effect seems to be less pronounced than the improvement in sensitivity at low frequencies for the sparse array.

When the array is phased to point the beam at zenith angle 45^o in the E- and H-planes, the unit cell sensitivity shows the same tendency to increase with the inter-element spacing at low frequencies (see Fig. 5.7) but less so than at 0^o scan angle. Furthermore, this antenna delivers a slightly larger sensitivity in the H-plane. When the array is denser, the mutual coupling effects are stronger and in-band anomalies appear, as for the case of a $\lambda/2$ spacing at 300 MHz. The origins and elimination of these anomalies are not considered in this chapter, but in reference [53] and in chapter 4 a summary of possible causes and solutions may be found.

Fig. 5.8 represents the unit cell sensitivity for 3 different sizes of the antenna element (see Table 5.4). An increase in the antenna size results in a larger sensitivity, which is to be expected at low frequencies where the antenna is better matched and the unit cell is fully and uniformly illuminated when the antenna size is comparable to the wavelength. However, when the antenna size is a multiple of $\lambda/2$ and at least a wavelength in size, the antenna pattern displays multiple lobes, which are represented as anomalies in the sensitivity plot (marked by arrows).

Table 5.4: Unit cell parameters – analysis of the antenna size, L.

d	L
$\lambda/2$ at 100 MHz	30 cm / 85 cm / 140 cm

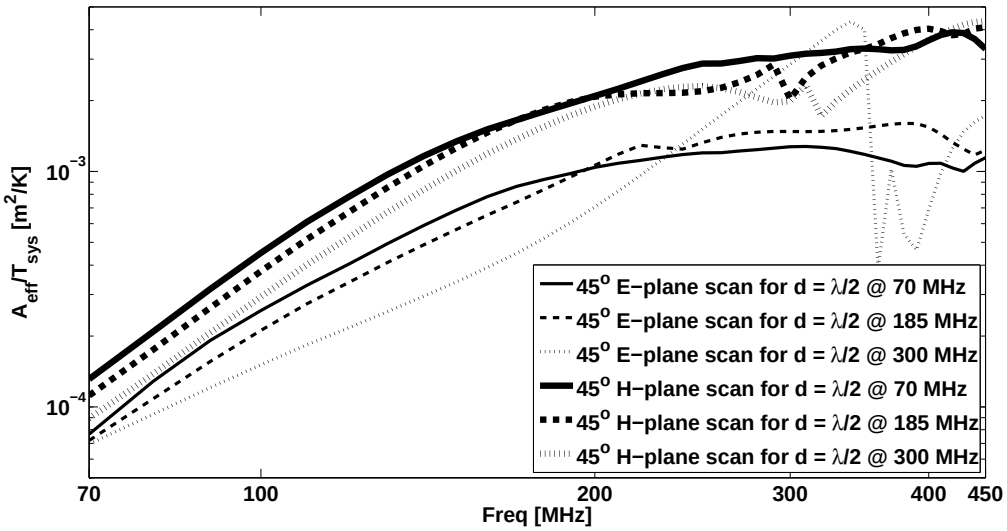

Figure 5.7: Simulated unit cell sensitivity at 45^o scan angle in both E- and H- planes for different inter-element spacing distances, d.

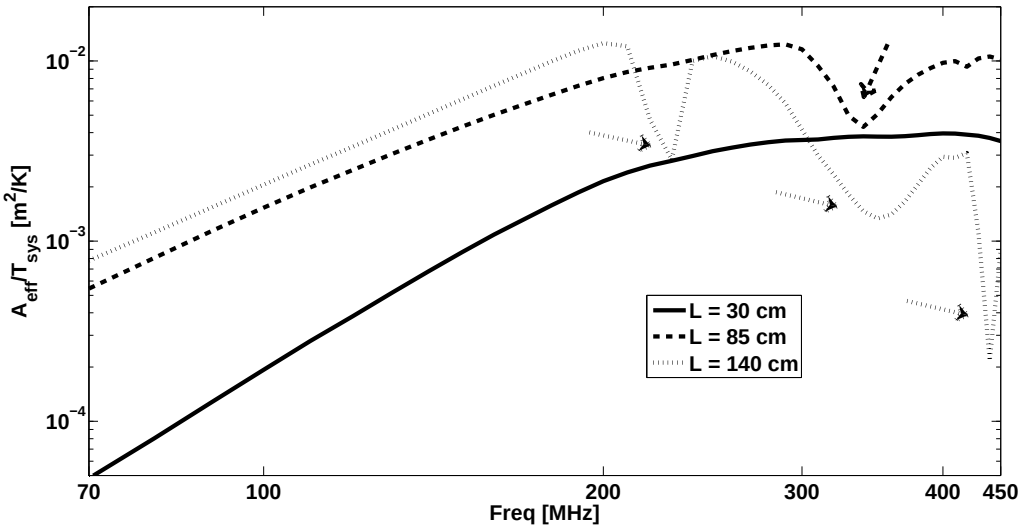

Figure 5.8: Simulated unit cell sensitivity at broadside scan for different antenna sizes, L.

Fig 5.9 shows what happens at 45^o scan angle, where one can see the same effects as for the broadside scan in both the principal planes and again the H-plane is more sensitive than the E-plane. The sparse and dense regimes are well defined and can be easily identified in the plots shown in this chapter.

The sensitivity in the sparse regime is limited by the $\lambda^2/2$ trend of the effective aperture and by the receiver noise, and is dependent on the element type, size and the mutual coupling. On the other hand, the dense regime sensitivity is normally limited by the sky noise, the inter-element spacing and the antenna element size. However, in between these two regions there is room for improvement by modifying the radiating structure. By tilting up the arms of the antenna by an angle α (see

Fig. 5.10), the impedance match can be improved (also at lower frequencies) as now the distance to the ground plane also scales with frequency and the structure naturally has a wider bandwidth. Fig. 5.11 shows how tilting the arms affects the system temperature. The optimum tilt angle appears to be around 30^o.

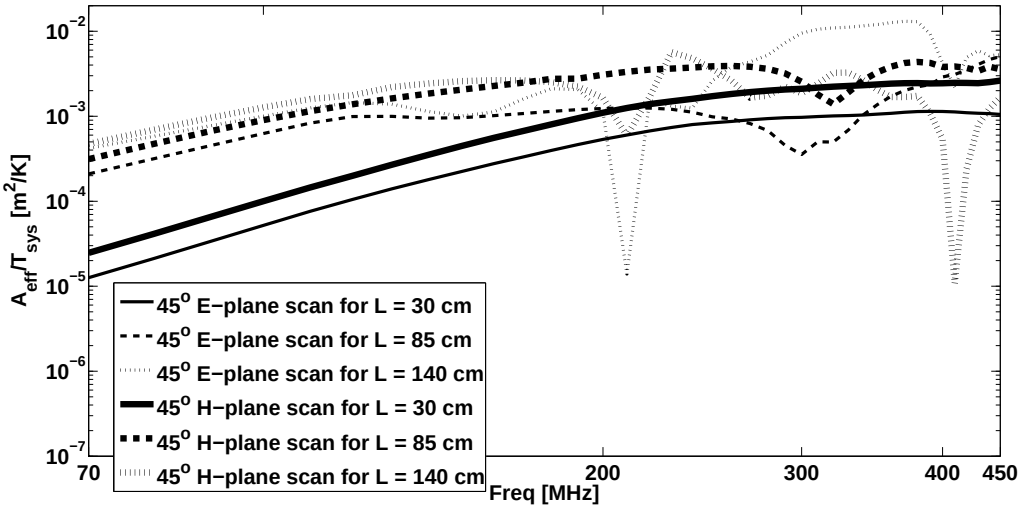

Figure 5.9: Simulated unit cell sensitivity at 45^o scan angle in both E- and H- planes for different antenna sizes, L.

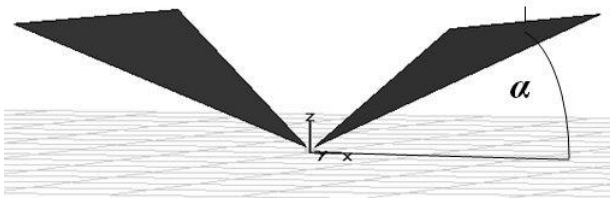

Figure 5.10: Bow-tie antenna element model with tilted arms.

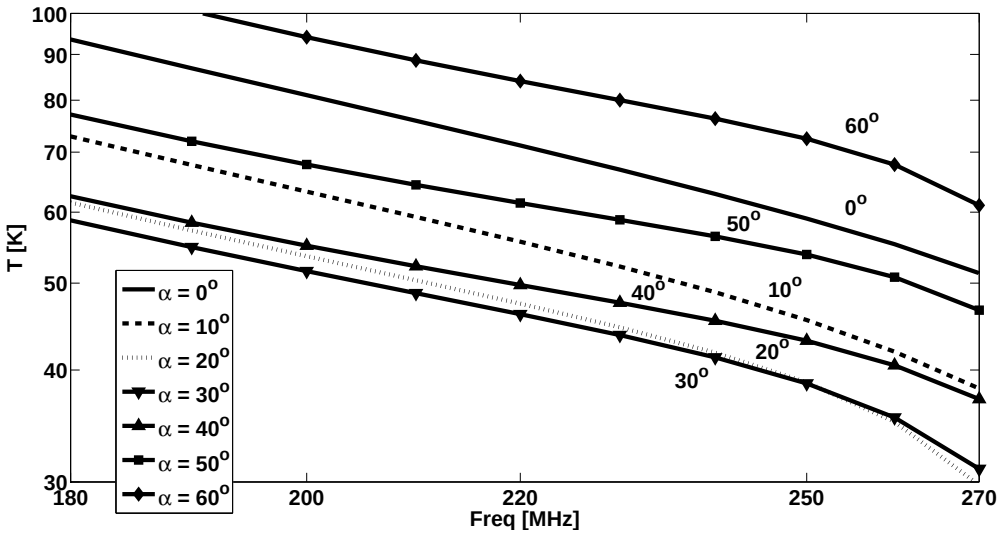

Figure 5.11: Simulated unit cell system temperature at 0^o scan angle for different tilt angles, α.

5.6 Prototype

A model of the proposed bow-tie antenna element, the BLU antenna (Bow-tie Low-frequency Ultra-wideband antenna) has been built and is ready for measurement (see Fig. 5.12). Furthermore, a 400-element scaled version of a SKA-AAlo station is being designed and will be soon built to prove the concept of the bow-tie elements and test different array configurations. This antenna will need to be extended to a dual-polarization configuration.

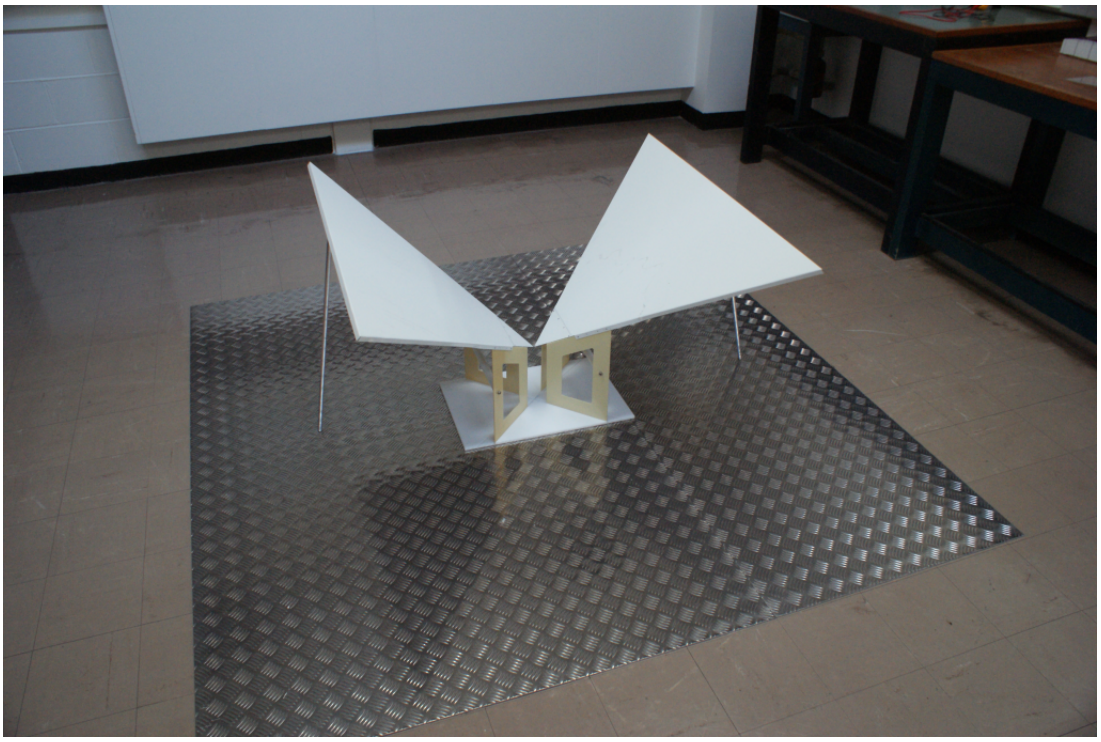

Figure 5.12: The BLU antenna.

5.7 Conclusions and future work

This chapter summarizes the main issues in the design of an antenna element for use in an ultra-wideband large aperture array, such as the SKA-AAlo. The most relevant codes in electromagnetic simulations currently available are described and a design process is presented. This is based on the system noise and the effective aperture of a unit cell in an infinite regular array, which define the instrument sensitivity, taken as the figure of merit for a radio telescope.

An analytical study has been described here of a bow-tie antenna element immersed in an infinite array, as a potential candidate for the SKA-AAlo, and it both refutes some well known facts about antenna theory and gives designers some useful hints on how to design a radio astronomy station. I found that larger elements,

with sizes comparable to the wavelength, are likely to give better sensitivities at low frequencies because of better matching to the amplifier, but at the cost of a more expensive antenna. Furthermore, the worse system temperature delivered by a smaller element can be partially mitigated by taking advantage of mutual coupling and placing antennas in a denser configuration, which improves the sensitivity at the high end of the band. However, at the low end of the band, due to the sky brightness constraint on the system noise, a sparser array delivers better sensitivity. This is due to the larger effective aperture of a sparser array which outperforms the improvement on sensitivity for denser arrays at higher frequencies. Also, a trade-off is necessary when finding the optimum size of the antenna for such an ultra-wideband application, as very large antenna elements display multiple lobes.

A bow-tie antenna element has proved to be a suitable candidate for this type of array, offering the necessary flexibility in a wide band of frequencies. Furthermore, a modification of the basic bow-tie element has been used to improve the system noise without modifying the overall antenna size or the inter-element spacing. With this new degree of freedom, it becomes easier to find a compromise to fulfill the SKA-AAlo requirements.

As a result of this work three conference proceeding contributions have been published [72, 73, 74] and one journal paper has been sent for publication [75].

In future, several lines of work will be considered:

1. A scale version of a SKA-AAlo station will be built and tested. It will also serve as a test bench for analyzing potential antenna elements and grid configurations.

2. The bow-tie antenna will be optimized in terms of cost based on the results obtained in the study described in this chapter. It will also need to be modified for optimal reception of two linear orthogonal polarizations. Then it will be measure and the matching with the LNA will be analyzed in detail.

3. New configurations (other than regular arrays) will be analyzed in a similar way.

In this chapter, I studied regular sparse array antennas for low-frequency radio astronomy. I limited the study to regular configurations due to the limitations in the commercial software packages. In the next chapter I will present a numerical method to simulate large array antennas, such as the ones proposed for the SKA, when they are in irregular configurations.

Chapter 6

On the Characterization of Large Finite Antenna Arrays for Low-Frequency Radio Astronomy

This chapter is oriented to the characterization of very large irregular array antennas for radio astronomy applications. An special-purpose simulation method, which will allow to carry out full-wave simulations, is presented.

The contents of this chapter have been published or made public in two conference proceeding contributions [19, 74].

6.1 Introduction

As it has been mentioned before in this thesis, the new generation of radio telescopes such as the SKA relies heavily on the use of large phased arrays [38]. In the sub 1 GHz frequency regime, the telescope can provide a million square metres of collecting area. Operating from 70 to 450 MHz, the SKA-AAlo will comprise up to hundreds of stations of at least 10,000 elements each. Furthermore, the SKA community is considering the use of irregular sparse configurations instead of the classical regular arrays. The cost of this choice in the design process is evident, as there are no commercial simulation packages which can handle large, sparse, random arrays. This is especially an issue at lower frequencies, where the array is in a dense configuration and the mutual coupling is stronger.

Sparse array configurations are of interest for the SKA because of its larger effective aperture compared to closely-packed arrays [79], where the effective aperture is limited by the physical space allocated to each antenna in the array. Irregular array configurations are also of interest for the SKA. For example, by randomizing the position of the antennas in the array grid, localized undesired effects, such as

grating lobes, may be spread over the parameter space. This will increase the noise ground of the telescope but will avoid blind angles or localized malfunctions of the instrument. Narrow band anomalies caused by mutual coupling are other example of undesired effects which could be mitigated by the use of non-periodic arrays. It is yet to be decided which is more convenient for the SKA.

Unfortunately, it is not possible at present to do a full-wave simulation of a real size SKA stations (up to at least 10,000 elements). In [105], the authors proposed a method for fast computation of the interactions between MBFs (Macro Basis Functions) based in a sub-gridding technique. This work has now been extended ([19]) in order to simulate a real size SKA station.

The method proposed in this chapter and published in [19] attempts to reduce the computational cost needed to solve the full EM problem in such arrays by using the MBF technique [106, 107] and the aforementioned interpolation method [105], proposed by Christophe Craeye and David González-Ovejero (*Université Catholique de Louvain*). This approximation provides a further computational cost reduction and is a first step towards a very fast full-wave simulation tool for very large irregular arrays, not comparable to anything available to my best knowledge. This chapter is part of an ongoing work in collaboration between the University of Cambridge, the *Universidad Carlos III de Madrid* and the *Université Catholique de Louvain*, who started this line of studies.

6.2 The method

The proposed Method of Moments (MoM) simulation for this problem relies on the use of MBFs [106, 108, 109], also called Characteristic Basis Functions [107, 18]. The MBF method consists of reducing the size of the MoM impedance matrix by replacing the original set of elementary basis functions with a new set of functions obtained through the solutions of smaller problems (more information given in section 5.4). Once the MoM matrix size is reduced by means of the MBF technique, the complexity $\mathcal{O}((N\,A)^3)$ for solving the system of equations is reduced to $\mathcal{O}((Q\,A)^3)$, where A is the number of antennas in the array and N and Q ($Q << N$) are the number of elementary and MBFs, respectively. Nevertheless, the impedance matrix filling time remains $\mathcal{O}((N\,A)^2)$, and rapidly becomes the dominant operation in the total solution time. To overcome this limitation, the computation of interactions between macro basis functions is carried out by interpolating exact data obtained on a simple grid; thereby non regular arrays may be easily analyzed as well as optimized. The complexity is now $\mathcal{O}(PN^2 + A^2S)$, where P (typically around some tens or low hundreds) is the number of elements in the grid and S is a small factor related to the interpolation time. It is interesting to notice that this factor no longer depends on

the complexity of the antenna. Therefore, a speed up, by a factor of order A can be obtained for sparse arrays. The performance of the interpolation method is shown in Fig. 6.1, where the embedded element pattern is computed for one antenna in a random array covering 47 elements. The reduced impedance matrix filling time was 77 minutes when only using MBFs and 20 seconds for the interpolation technique (without accounting for the grid generation time) in a standard laptop. The initial target is to obtain the pattern for an example comprising 1,000 bow-tie elements, like the one shown in Fig. 6.2(a), randomly placed in a circular area of radius 30λ (Fig. 6.2(b)), which at this point would represent a reduced version of the aforementioned SKA-AAlo. For the present analysis, the average minimum distance between elements is 1.5λ and the elements size is λ x λ. Each port has been loaded with a 200 Ω series impedance.

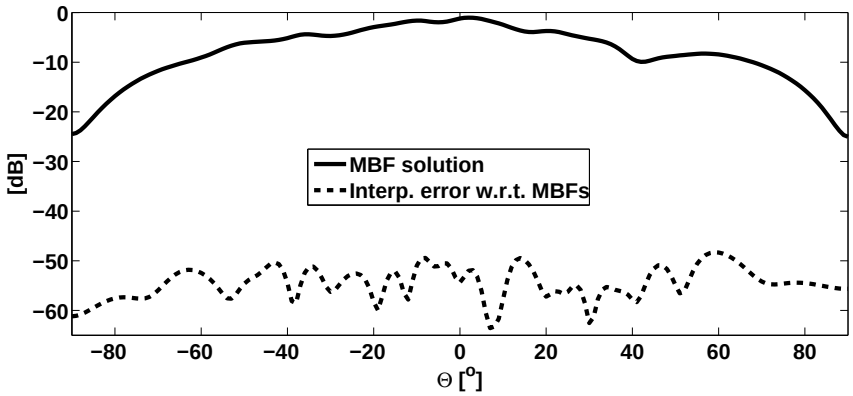

(a) E-plane

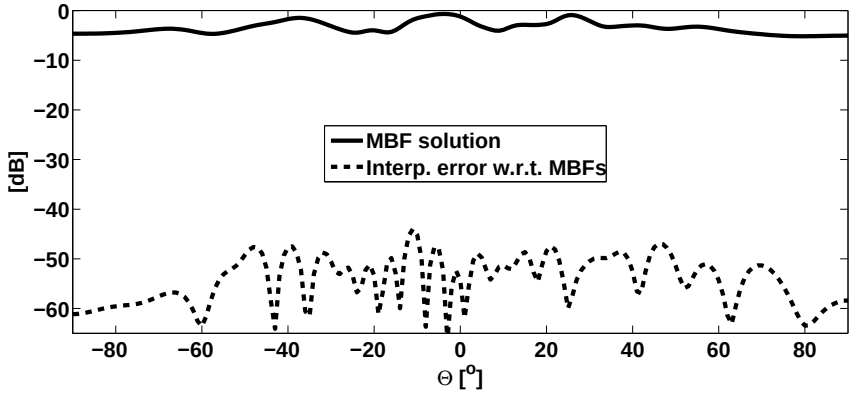

(b) H-plane

Figure 6.1: Embedded element pattern obtained with the MBF approach and error for the interpolation technique w.r.t MBF solution.

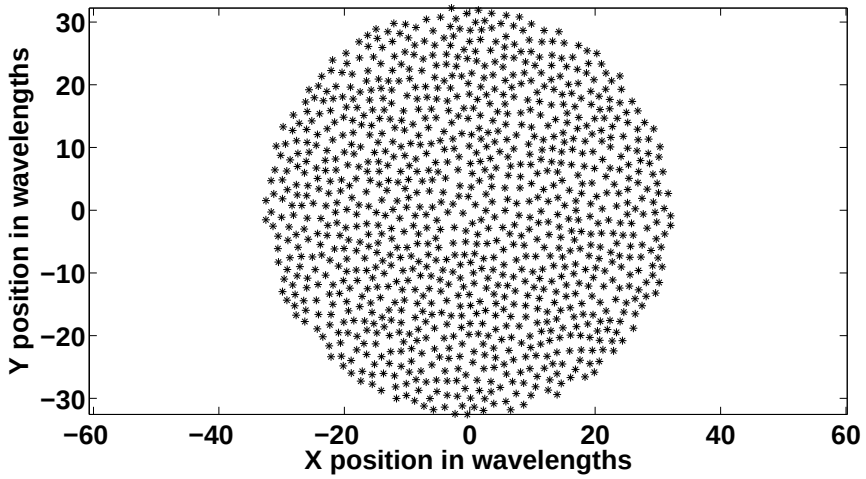

(a) Array layout

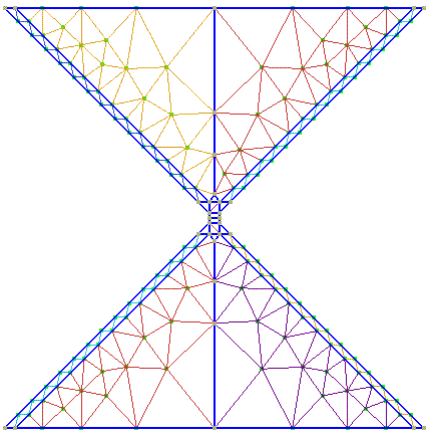

(b) Bowtie mesh

Figure 6.2: Array configuration.

In the exact case, the embedded patterns should model, for each antenna in the array, the field radiated by the element of interest excited while the rest of elements in the array are passively terminated. This computation should involve all the elements in the array, though it is not possible within our memory limits (it is possible to simulate up to ~ 300 elements with a conventional laptop). Nevertheless, a "radius of influence" can be defined for every antenna in the array. The embedded pattern is then computed accounting only for the antennas contained in the circle defined by this radius. Assuming that this approximation is good enough, the complexity in the calculation of the interactions and the solution of the MoM system of equations, can be dramatically reduced. In order to prove the convergence of the method, Fig. 6.3(a) and Fig. 6.4(a) show the normalized embedded element pattern in dB for one of the antennas in the array. Both E-plane and H-plane cuts converge reasonably well for a radius of influence larger than 5λ. Fig. 6.3(b) and Fig. 6.4(b) represent

the differential error between the patterns computed for different radius of influence with respect to the pattern calculated for the largest radius considered (7λ). Again, in both planes, the differential error decreases rapidly and seems to converge after 5λ.

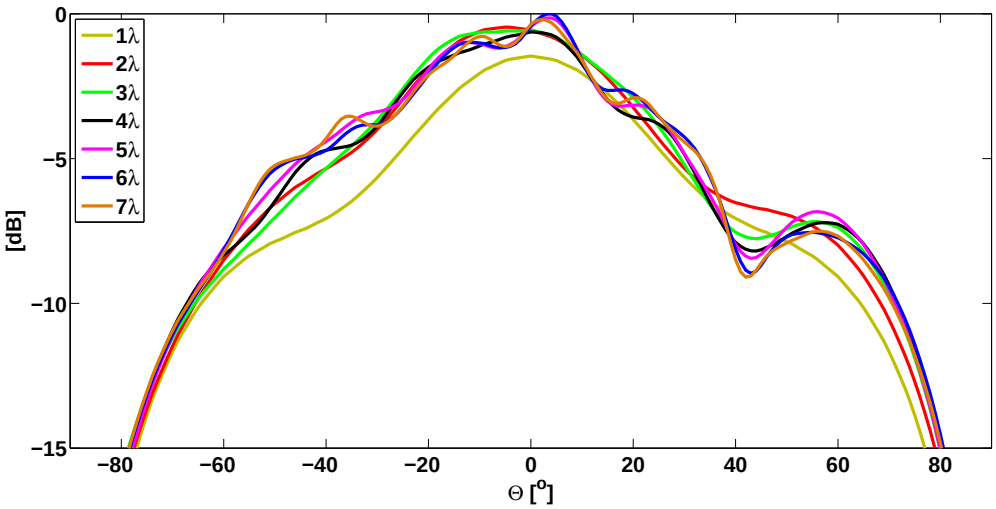

(a) E-plane

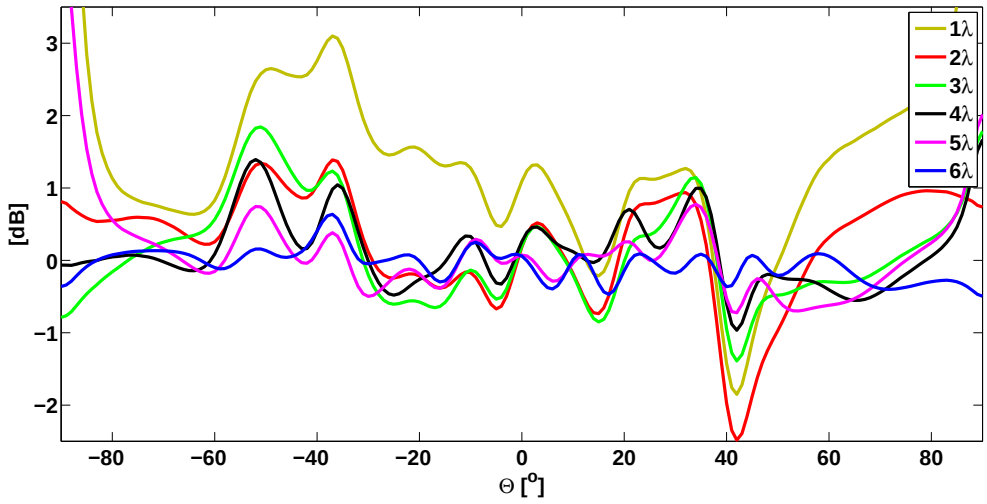

(b) E-plane error

Figure 6.3: E-plane embedded element patterns and errors for different radius of influence.

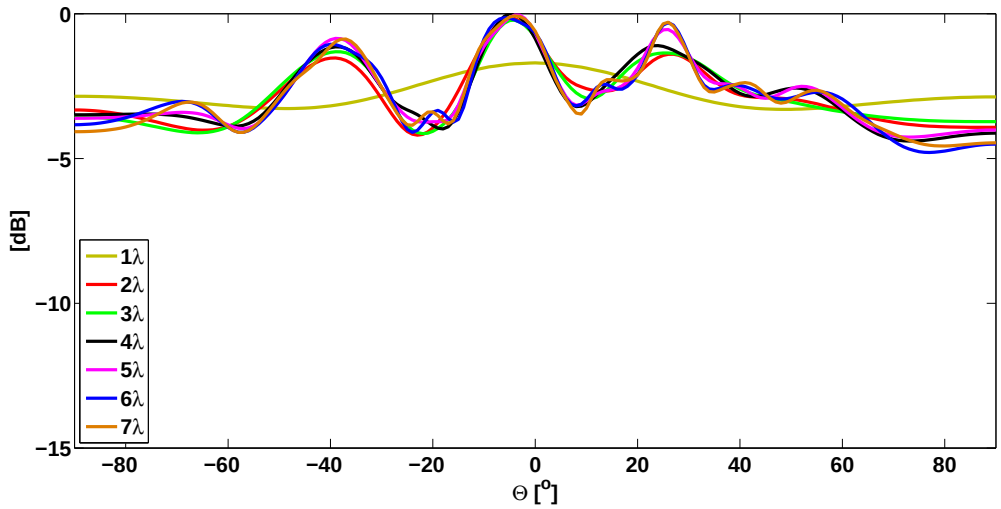

(a) H-plane

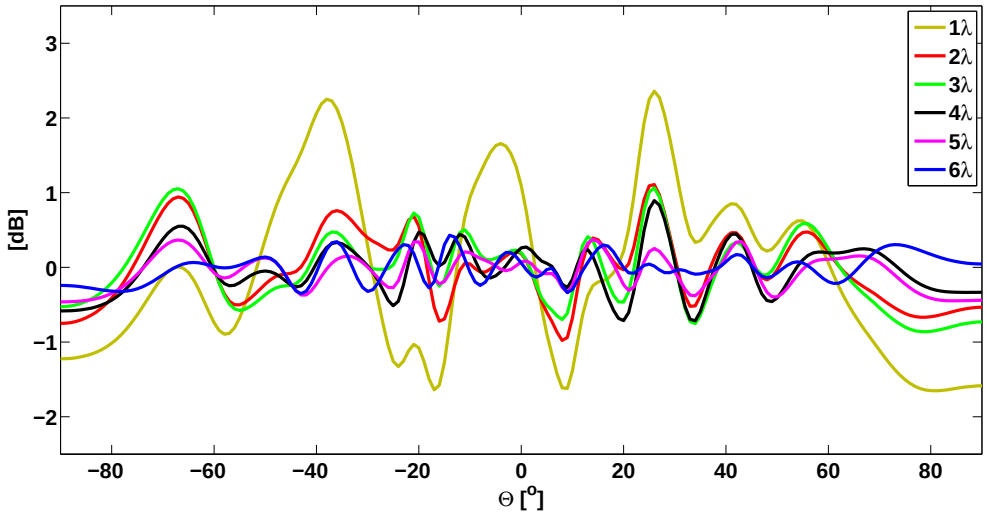

(b) H-plane error

Figure 6.4: H-plane embedded element patterns and errors for different radius of influence.

6.3 Numerical results

The total array pattern for the example array is shown in Fig. 6.5. It was computed using a radius of influence of 7λ. Also the array radiation pattern computed from the single element patterns (dismissing mutual coupling effects) is shown. Despite the apparent similarity between both approaches there is a systematic bias between them. For the present case a difference of 0.45 dB is observed in the broadside direction between both approaches. The convergence of the average embedded element pattern to the single element pattern for an array of 1,000 elements randomly located and placed a distance of $\lambda/4$ to the ground plane is shown in Fig 6.6. From these results it seems that, despite there is a small bias between both cases, the con-

vergence of the average of all the embedded element patterns in a random array to the single element pattern is good. In other words, the randomized mutual coupling effects are being averaged out.

Fully random arrays are not achievable in principle due to the finite size of the arrays and the non-zero size of each antenna element. Depending on the degree of randomization of the antenna positions, the mutual coupling effects are also likely to be randomized out. However, non-periodic grids will still suffer from mutual coupling and its effects won't cancel out. Therefore, numerical methods capable of simulating large irregular arrays of sizes up to hundreds of wavelengths are needed.

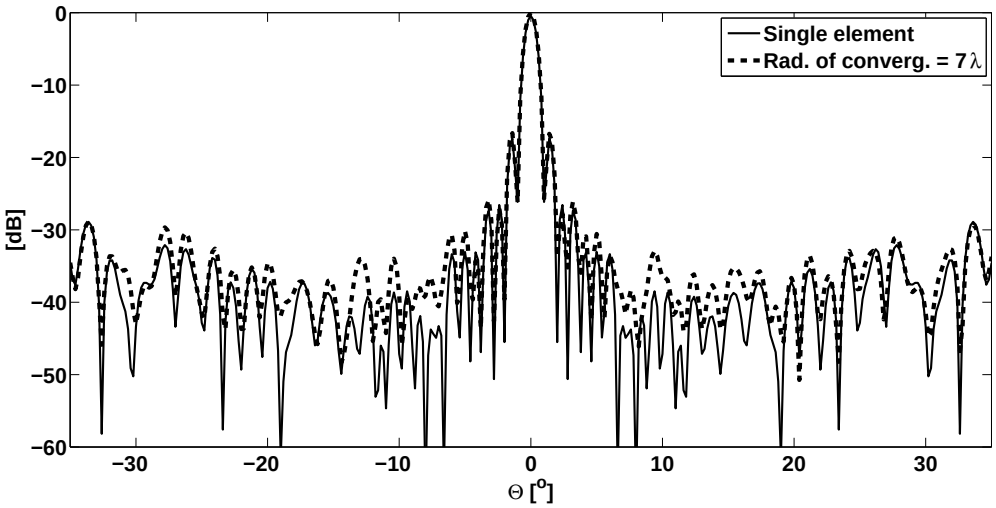

(a) E-plane

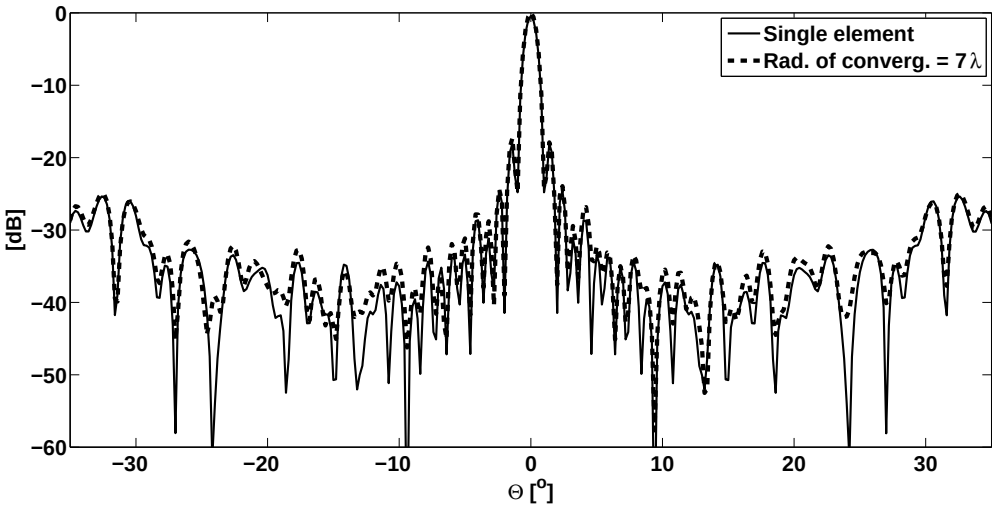

(b) H-plane

Figure 6.5: Array Patterns assuming single element patterns and including mutual coupling up to a 7λ radius.

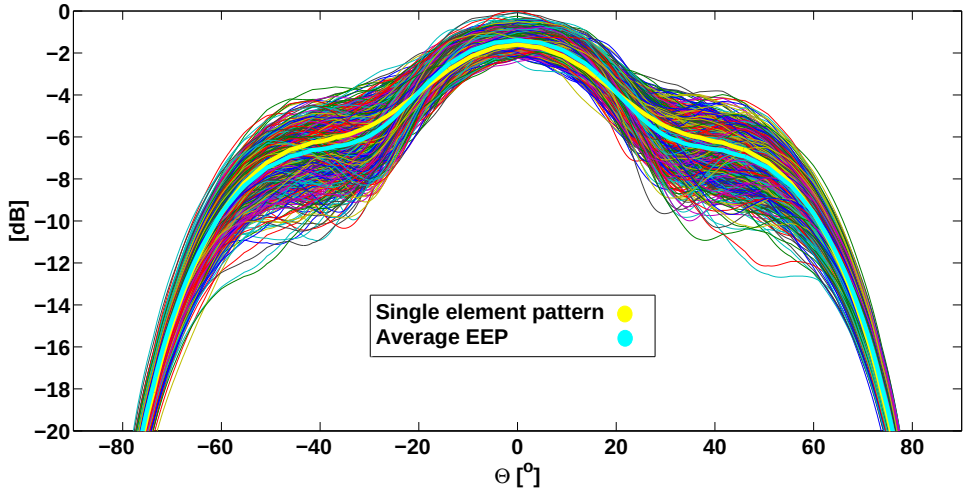

(a) E-plane

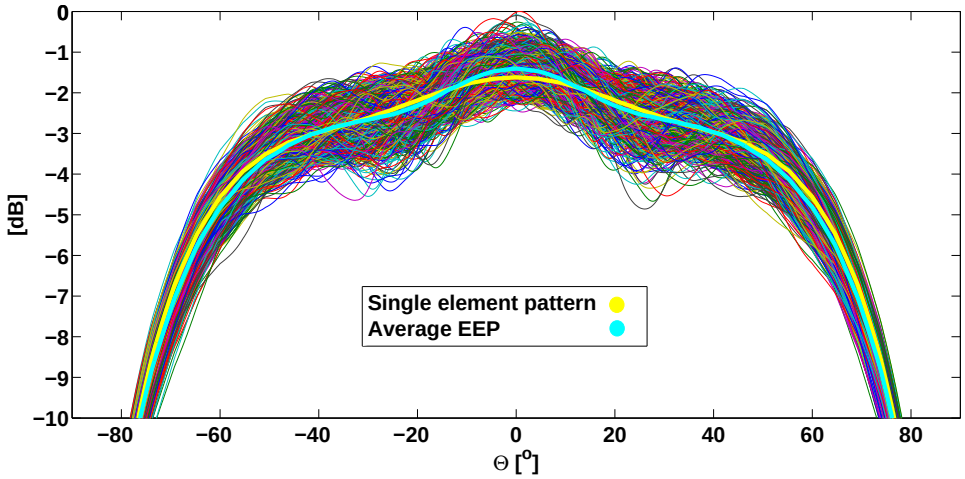

(b) H-plane

Figure 6.6: Average embedded element pattern (EEP) vs single element pattern. The 1,000 EEPs are also shown.

6.4 Conclusions and future work

A numerical method for the full EM simulation of large ultra-wideband arrays has been developed starting from an MoM code. It represents the first step towards the full EM characterization of a SKA-AAlo station. It is specifically applicable to irregular arrays and it is based on an interpolation technique of the interactions between MBFs. The number of interactions that need to be calculated is reduced by defining a "radius of influence" for every antenna. The system can be either solved for each antenna or globally with the help of a sparse matrix solver. The convergence of the method has been proven and it has a great potential for radio astronomy applications.

The computation parameters of the latest stable version of the code in a standrad laptop are:

- Computation time:
  - Preprocess (computing data to interpolate): 37 min.
  - Computing 1000 EEPs: 1000·36 s $\sim$ 10h.
- Memory:
  - Only 17.8 MB of contiguous memory required.
- Speed:
  - 10h per simulation: excessive.
  - Sparse matrices (initial results): Simulation time reduced to 1h.
  - Requires more contiguous memory: 1.77 GB

As a result of this work two conference proceeding contributions [19, 74] have been published.

In future, several lines of work will be considered:

1. To migrate towards C code and parallelize part of the Matlab code in order to speed up the calculations.
2. Use of different NFFT (Non-uniform Fast Fourier Transform) schemes for the array pattern calculation.
3. To improve the sparse matrix solution which will speed up the calculation.
4. To get a deeper understanding on the behaviour of mutual coupling in random arrays.
5. To move to a calibration like scheme where the array response can be represented by few coefficients.
6. To improve the ratio accuracy/complexity of the method (further study of the convergence versus the radius of influence).
7. To validate the method with a scaled prototype of a SKA-AAlo station.

Chapter 7

Conclusions and Future Work

Next-generation radio astronomy will be led by the SKA telescope. The ambitious objectives of the SKA will be only possible if the required technology can be realized and within the budget. Components include: Antennas, amplifiers, communications, power supply, processing technologies, etc. It is a long list of state-of-the-art technology which needs to become real within the next few years. Actually, the design process must assume advances which will take place in the future in order to design today the most powerful telescope of tomorrow's world.

In this context, the work of this thesis was focused on the design of the most visible part of any radio telescope, and the point which first meets the space signals; the antenna layer. The SKA aims for ultra-wideband arrays to cover the sub 1 GHz frequency band. They need to be ultra-wideband among other reasons in order to reduce the cost of the system. However, the realization of ultra-wideband low-cost low-frequency arrays is not free of difficulties. The analysis of these issues and its solutions and the design of ultra-wideband arrays fulfilling the SKA requirements have been the core of this thesis.

The array designs I have presented in this thesis could be divided in two according to the frequency band they intend to cover; arrays for the high frequency band of the SKA aperture array proposal (SKA-AAhi: 0.3 to 1 GHz) and arrays for the low frequency band (SKA-AAlo: 0.07 to 0.45 GHz).

To cover the SKA-AAhi band dense arrays have been considered, as in these arrays, one can take advantage of the mutual coupling and of close inter-element spacing to deliver a fixed effective aperture across the band, wider beams that result in a faster survey speed and easier beamforming, and absence of grating lobes. This is of interest in the "high band" due to the low sky noise temperature at those frequencies. In this thesis I focused on differential technology, which in principle had a better potential for low noise applications as the balancing device can be avoided. I studied infinite dual-polarized arrays of tapered slot antenna elements and then I designed several arrays to meet the specifications of the SKA.

In chapter 3, I presented my work on arrays of these kinds where low-cost was the main target. Large antennas to reduce the number of amplifiers per square metre and the use of inexpensive materials were the main lines of work of this chapter. A design meeting the desired scan range from -45^o to 45^o in both the E- and H-plane was obtained. Then I presented the measurement process of a finite tile composed of differentially-fed elements as the ones designed in the infinite array environment. The results were good.

In chapter 4, I analyzed, through a parametric study, a dual-polarized array of differentially-excited elements ("bunny-ear" antennas), in order to demonstrate the effect of various antenna element geometries on the scan impedance characteristics of an infinite-by-infinite array. The elements had no dielectric components. I used the knowledge gained in the designs described in chapter 3 to study an E-plane differential-mode scan impedance anomaly, which was caused by an even-mode that was supported by the differentially-fed antenna array in the presence of a third conductor, such as a ground plane. I showed that the impedance resonance could be suppressed by a (low-loss) balancing-dissipation technique using a pair of resistors. The associated reduction in system sensitivity was analyzed and it showed that the increment of the corresponding antenna noise temperature was less than 10 K for 3 kΩ resistors at room temperature (290 K). An optimized antenna design was presented meeting the specifications of the SKA project while keeping the potential manufacturing cost as low as possible. I also presented the prototype built and measured.

The low-frequency band of the SKA needs sparse arrays in order to overcome the high sky noise temperature present at those frequencies. The issues associated with the design and characterization of large arrays for low-frequency radio astronomy as well as a design of an ultra-wideband element for the SKA-AAlo and a method to simulate large irregular arrays were presented in chapters 5 and 6.

In chapter 5, I presented the main issues in the design of an antenna element to be used in an ultra-wideband large aperture array, such as the SKA-AAlo. I also summarized the most relevant codes in electromagnetic simulations currently available. Finally, I described the design process of an ultra-wideband antenna element (a bow-tie antenna) that could be used in a sparse array such as the SKA-AAlo. This was based on the system noise and the effective aperture of a unit cell in an infinite regular array, which define the instrument sensitivity. The results were encouraging.

I described an analytical study of a bow-tie antenna element immersed in an infinite array, as a potential candidate for the SKA-AAlo, which both refuted some well known facts about antenna theory and gave designers some useful hints on how to design a radio astronomy station. I found that larger elements, with sizes com-

parable to the wavelength, were likely to give better sensitivities at low frequencies because of better matching to the amplifier, but at the cost of a more expensive antenna. Furthermore, the worse system temperature delivered by a smaller element could be partially mitigated by taking advantage of mutual coupling and placing antennas in a denser configuration, which improved the sensitivity at the high end of the band. However, at the low end of the band, due to the sky brightness constraint on the system noise, a sparser array delivered better sensitivity. This was due to the larger effective aperture of a sparser array which outperformed the improvement on sensitivity for denser arrays at higher frequencies. Also, a trade-off was necessary when finding the optimum size of the antenna for such an ultra-wideband application, as very large antenna elements displayed multiple lobes.

In chapter 6, I described a numerical method for the full EM simulation of large ultra-wideband arrays. The code represented the first step towards the full EM characterization of a SKA-AAlo station. It was specifically applicable to irregular arrays and it was based on an interpolation technique of the interactions between MBFs in a MoM code. The number of interactions that need to be calculated was reduced by defining a "radius of influence" for every antenna. The system could be either solved for each antenna or globally with the help of a sparse matrix solver. The convergence of the method was shown and it had a great potential for radio astronomy applications.

7.1 Contributions

The work I have done during the last for years and I have presented in this thesis has led to the construction of three prototypes for the SKA: FLOWPAD^3, FIDA^3 and the BLU antenna. The two first prototypes are dense arrays of TSA elements and represent a technology which could cover the middle frequency band of the SKA. The latest is a single element which could be part of sparse array to cover the low frequency band of the SKA.

FLOWPAD^3, developed in ASTRON, represents a **low-cost differential technology prototype** to probe the viability of using inexpensive materials and construction techniques for the SKA-AAhi. A **measurement procedure for arrays of differentially-fed elements** was undertaken. **FLOTT**, a specific realization of FLOWPAD^3 has been built for the **2PAD** project, demonstrator for SKADS.

FIDA^3 (OAN and the University Carlos III of Madrid) is composed of bunny-ear antenna elements and its main contribution has been to probe the viability of a **dielectric-free differentially-fed array that fulfills the SKA specifications**. Furthermore, a **solution to narrow band anomalies** has been proposed and evaluated in terms of the noise temperature of the array.

The **BLU antenna**, developed in the University of Cambridge, is a single element built from the results of the designs and analysis of sparse arrays for the SKA-AAlo. These studies explored the different trade-offs in the **design of large aperture arrays for low-frequency radio astronomy**. The main parameters of the array were analyzed in terms of the system sensitivity.

Finally, in collaboration with the Université Catholique de Louvain, I worked in the development of a numerical method for **characterization of large irregular arrays for radio astronomy**. This has shown to be a fast and accurate solution when a simulation of a large finite irregular array is needed.

The contents of this thesis have been published in a number of publications (see the *List of Publications* at the beginning of the thesis).

7.2 Future work

In future, several lines of work will be considered:

1. The relationships between the common-mode and the differential-mode scan impedances and their relationships to high-Q anomalies associated with differential technology. Also, it is important to study the optimal matching conditions that apply to differential antenna and LNA designs.

2. The effect of the finiteness of the array. Even if the array is regarded as infinite due to the large number of elements present in each station of the telescope, it is important to analyze the effect of different realizations of the array, e.g. if this is regarded as a collection of tiles, what is the effect of connections between tiles. It will be also necessary to quantify the edge effects for large stations. This should be done by simulating infinite-by-finite arrays and large finite arrays, making use of numerical-method-based codes such as [19]. This information is especially valuable for calibration purposes. The results of such an analysis would useful to elaborate on the necessity of e.g. dummy elements in the outside of the array in order to reduce the effect of the finiteness of the array.

3. The characterization of the cross-polarization patterns of the array for all angles and scan angles. The next phase of the SKA project will be focused on developing calibration systems, which in most cases will require a very accurate knowledge of the cross-polarization patterns.

4. An analogue ultra-wideband beamforming network will be necessary if the conversion to digital happens at a later stage. Undesired anomalies could

arise from specific designs of the LNAs and the beamforming network and these must be properly characterized as in the present study.

5. A scale version of a SKA-AAlo station will be built and tested. It will also serve as a test bench for analyzing potential antenna elements and grid configurations.

6. The bow-tie antenna presented in chapter 5 will be optimized in terms of cost based on the results obtained in the study described. It will also be extended to a dual-polarization configuration. Then it will be measure and the matching with the LNA will be analyzed in detail.

7. New configurations (other than regular arrays) will be analyzed in a similar way to the process described in chapter 5 for regular sparse arrays.

8. Migration of the MoM code presented in chapter 6 towards C code and parallelization of part of the Matlab code in order to speed up the calculations.

9. The use of different NFFT (Non-uniform Fast Fourier Transform) schemes for the array pattern calculation.

10. Improvement of the sparse matrix solution which will speed up the calculation.

11. Analysis of the behaviour of mutual coupling in random arrays.

12. Migration to a calibration like scheme where the array response can be represented by few coefficients.

13. Improvement of the ratio accuracy/complexity of the method (further study of the convergence versus the radius of influence).

14. Validation of the method with a scaled prototype of a SKA-AAlo station.

List of Figures

List of Tables

Bibliography

[1] W. T. Sullivan, *The early years of Radio Astronomy (reflections 50 years after Jansky's discovery)*. Cambridge University Press, 1984.

[2] B. F. Burke and F. Graham-Smith, *An introduction to Radio Astronomy*. Cambridge University Press, 2nd ed., 2002.

[3] www.nrao.edu/index.php/learn/radioastronomy/radioastronomyhistory.

[4] T. L. Wilson, K. Rohlfs, and S. Hüttemeister, *Tools of Radio Astronomy*. Springer, 5th ed., 2009.

[5] J. D. Kraus, *Radio Astronomy*. Powell, Ohio: Cygnus-Quasar Books, 2nd ed., 1986.

[6] www.wikipedia.org.

[7] www.skatelescope.org.

[8] R. Bolton, A. Faulkner, P. Alexander, S. Torchinsky, A. van Ardenne, P. Wilkinson, M. de Vos, L. Bakker, S. Garrington, G. Harris, T. Ikin, M. Jones, D. Kant, D. Kettle, R. McCool, P. Patel, and J. Romein, "Skads benchmark scenario design and costing - 2 (the ska phase 2 aa scenario)," SKA memo 111, July 2009. available on www.skatelescope.org.

[9] A. van Ardenne, H. Butcher, J. G. bij de Vaate, A. J. Boonstra, J. D. Bregman, B. Woestenburg, K. van der Schaaf, P. N. Wilkinson, and M. A. Garrett, "The aperture array approach for the square kilometre array," white paper, May 2003. Available on www.skatelescope.org.

[10] W. L. Stutzman and G. A. Thiele, *Antenna Theory and esign*. John Wiley & Sons, 2nd ed., 1998.

[11] C. A. Balanis, *Antenna Theory*. John Wiley & Sons, 3 ed., 1997.

[12] R. C. Hansen, *Phased Arrays Antennas*. John Wiley & Sons Inc., 2001.

[13] R. J. Mailloux, *Phased array antenna handbook*. Artech House, 1994.

[14] D. M. Pozar and D. Schaubert, "Scan blindness in infinite phased arrays of printed dipoles," *IEEE Trans. On Antennas and Propagation*, vol. 32, pp. 602–610, June 1984.

[15] D. H. Schaubert, "A class of e-plane scan blindnesses in single-polarized arrays of tapered-slot antennas with a ground plane," *IEEE Transactions on Antennas and Propagation*, vol. 44, pp. 954–959, July 1996.

[16] www.cst.com.

[17] www.ansoft.com.

[18] R. Maaskant, R. Mittra, and A. Tijhuis, "Fast analysis of large antenna arrays using the characteristic basis function method and the adaptive cross approximation algorithm," *IEEE Transactions on Antennas and Propagation*, vol. 56, pp. 3440–3451, November 2008.

[19] D. González-Ovejero, E. de Lera Acedo, N. Razavi-Ghods, and C. Craeye, "Fast mbf based method for large random array characterization," in *IEEE Antennas and Propagation Society International Symposium, APSURSI '09*, (Charleston, SC), pp. 1–4, 1-5 June 2009.

[20] T. S. Bird and G. Cortes-Medellin, "Multibeam feed array design for the arecibo radio telescope," in *IEEE Antennas and Propagation Society International Symposium*, vol. 1, pp. 116–119, 22-27 June 2003.

[21] J. Simons, J. G. bij de Vaate, M. Ivashina, M. Zuliani, V. Natale, and N. Roddis, "Design of a focal plane array system at cryogenic temperatures," in *First European Conference on Antennas and Propagation, EuCAP 2006*, pp. 1–6, 6-10 November 2006.

[22] M. A. Garrett, H. Rampadarath, E. Lenc, and O. Wucknitz, "Lofar, e-lofar and low-frequency vlbi," in *European VLBI Network IX Symposium*, September 2008.

[23] A. van Ardenne, P. N. Wilkinson, P. D. Patel, and J. G. bij de Vaate, "Electronic multi-beam radio astronomy concept: Embrace a demonstrator for the european ska program," *Experimental Astronomy*, vol. 17, pp. 65–77, June 2004.

[24] P. W. Hannan, "The element-gain paradox for a phased array antenna," *IEEE Transactions on Antennas and Propagation*, vol. 12, pp. 423–433, July 1964.

[25] E. de Lera Acedo and E. G. Muñoz, "Mutual coupling edge effect approximation for phased-array antennas," in *IEEE AP-S International Symposium 2007*, (Honolulu, Hawaii, EEUU), 11-15 June 2007.

[26] C. Craeye and M. Arts, "On the receiving cross section of an antenna in infinite linear and planar arrays," *Radio Science*, vol. 39, no. RS2010, 2004.

[27] www.zeland.com/ie3d.htm.

[28] M. F. Morales, "Design princples of the mileura wide-field array low frequency demonstrator (mwa-lfd)," in *From Clark Lake to the Long Wavelength Array: Bill Erickson's Radio Science ASP Conference Series*, vol. 345, (Santa Fe, New Mexico, USA), p. 452, 8-11 September 2004.

[29] J. Craig, L. Rickard, S. Ellingson, G. Taylor, Y. Pihlstrom, N. Kassim, P. Ray, T. Clarke, L. D'Addario, R. Navarro, A. Cohen, P. Crane, B. Hicks, E. Polisensky, H. Schmitt, and L. Cox, "The architecture of an lwa station - a new phased-array radio telescope," in *Bulletin of the American Astronomical Society*, vol. 41, p. 671, May 2009.

[30] H. Holter, T. H. Chio, and D. H. Schaubert, "Experimental results of 144-element dual polarized endfire tapered-slot phased arrays," *IEEE Trans. On Antennas and Propagation*, vol. 48, pp. 1707–1718, November 2000.

[31] R. Maaskant, M. Popova, and R. van de Brink, "Towards the design of a low cost wideband demonstrator tile for the ska," in *Proc. European Conf. on Antennas and Propag.*, (Nice, France), 2006.

[32] T.-H. Chio and D. H. Schaubert, "Parameter study and design of wide-band widescan dual-polarized tapered slot antenna arrays," *IEEE Trans. On Antennas and Propagation*, vol. 48, pp. 879–886, June 2000.

[33] D. H. Schaubert, S. Kasturi, A. O. Boryssenko, and W. M. Elsallal, "Vivaldi antenna arrays for wide bandwidth and electronic scanning," in *The Second European Conference on Antennas and Propagation, 2007, EuCAP 2007*, pp. 1–6, 11-16 November 2007.

[34] H. Holter, "Dual-polarized broadband array antenna with bor-elements, mechanical design and measurements," *IEEE Trans. On Antennas and Propagation*, vol. 55, pp. 305–312, February 2007.

[35] S. G. Hay, J. D. O'Sullivan, J. Kot, C. Granet, A. Grancea, A. R. Forsyth, and D. Hayman, "Focal plane array development for askap (australian ska

pathfinder)," in *EuCAP 2007. The Second European Conference on Antennas and Propagation*, pp. 1–5, 11-16 November 2007.

[36] A. B. Smolders and G. W. Kant, "Thousand element array (thea)," in *IEEE Antennas and Propagation Society International Symposium, 2000*, vol. 1, pp. 162–165, 2000.

[37] www.skads-eu.org.

[38] R. T. Schilizzi, P. Alexander, J. M. Cordes, P. E. Dewdney, R. D. Ekers, A. J. Faulkner, B. M. Gaensler, P. J. Hall, J. L. Jonas, and K. I. Kellermann, "Preliminary specifications for the square kilometre array," SKA memo 100, December 2007. available on www.skatelescope.org.

[39] P. Alexander, R. Bolton, A. Faulkner, S. Torchinsky, A. van Ardenne, P. Wilkinson, M. de Vos, L. Bakker, S. Garrington, G. Harris, T. Ikin, M. Jones, D. Kant, R. McCool, and P. Patel, "Skads benchmark scenario design and costing," SKA memo 93, June 2007. available on www.skatelescope.org.

[40] http://www.ctit.utwente.nl/research/projects/national/senter/pacman.doc/.

[41] E. de Lera Acedo, "Pacman flowpad3 demonstrator (pacman active tile with cots lna) - antenna design and performance analysis," technical report, Dwingeloo, The Netherlands, June 2007. available on http://www.skads-eu.org/.

[42] E. de Lera Acedo, "Differential dual polarized antenna array design," in *2nd SKADS Workshop and Mid Term Review*, (Meudon, France), 10-11 October 2007.

[43] E. de Lera Acedo, "Low costing arrays of differentially fed tsa elements," in *SKADS MCCT Technical Workshop on Design of Wideband Receiving Array Systems*, (Dwingeloo, The Netherlands), 26-30 November 2007. available on http://www.astron.nl/other/workshop/MCCT/index.php.

[44] M. Arts, R. Maaskant, E. de Lera Acedo, and J. G. bij de Vaate, "Broadband differentially fed tapered slot antenna array for radio astronomy applications," in *3rd European Conference on Antennas and Propagation, 2009, EuCAP 2009*, (Berlin), pp. 566–570, 23-27 March 2009.

[45] J. G. bij de Vaate, L. Bakker, E. E. M. Woestenburg, R. H. Witvers, G. W. Kant, and W. van Capellen, "Low cost low noise phased-array feeding systems for ska pathfinders," in *13th International Symposium on Antenna Technology*

and Applied Electromagnetics and the Canadian Radio Science Meeting, 2009. ANTEM/URSI 2009., (Toronto, ON), pp. 1–4, 15-18 February 2009.

[46] R. Maaskant, "Antenne-inrichting, antenne-array, samenstel voor het assembleren van een antenne-array en een elektronische inrichting omvattende een antenne."

[47] B. Schüppert, "Microstrip/slotline transitions: Modeling and experimental investigation," *IEEE Traansactions on Microwave Theory and Techniques*, vol. 36, pp. 1272–1282, August 1988.

[48] K. C. Gupta, R. Garg, and I. J. Bahl, *Microstrip Lines and Slotlines*. Artech House, 1979.

[49] www.meco.nl.

[50] E. García, E. de Lera Acedo, D. Segovia, and V. Gonzalez, "Elimination of scan impedance anomalies in phased arrays," in *IEEE Antennas and Propagation Society International Symposium 2008*, (San Diego, CA), pp. 1–4, 5-11 July 2008.

[51] E. García, E. de Lera Acedo, V. González, and D. Segovia, "Elimination of scan impedance anomalies in ultra-wide band phased arrays of differentially fed tapered slot antenna," in *XXIII Simposium Nacional de la Unión Científica Internacional de Radio, URSI'08*, (Madrid), 12-15 September 2008.

[52] O. García-Perez, L. García-Muñoz, E. de Lera Acedo, J. Serna-Puente, V. Gonzalez-Posadas, J. Vazquez-Roy, and D. Segovia-Vargas, "Differential active antennas for the ska," in *3rd European Conference on Antennas and Propagation, 2009, EuCAP 2009*, (Berlin), 23-27 March 2009.

[53] E. de Lera Acedo, E. García, V. González-Posadas, J. L. Vázquez-Roy, R. Maaskant, and D. Segovia, "Study and design of a differentially fed tapered slot antenna array," *IEEE Transactions on Antennas and Propagation*, vol. 58, pp. 68–78, January 2010.

[54] L. R. Lewis, M. Fasset, and J. Hunt, "A broad-band stripline array element," in *IEEE Int. Symp. Antennas Propagat. Dig.*, pp. 335–337, 1974.

[55] P. J. Gibson, "The vivaldi aerial," in *Proc. 9th European Microwave Conf.*, (Brighton, UK), pp. 101–105, 1979.

[56] the European SKA Consortium, "The european concept for the ska," white paper, July 2002. Available on www.skatelescope.org.

[57] E. de Lera Acedo, E. G. Muñoz, E. Rajo, and D. Segovia, "A coplanar vivaldi antenna with wide band balun proposal for the low frequency band of the ska: approach to the fpa solution," in *IEEE Mediterranean Electrotechnical Conference 2006, MELECON 2006*, (Benalmádena, Málaga, Spain), pp. 557–560, 16-19 May 2006.

[58] E. de Lera Acedo, E. G. Muñoz, E. Rajo, J. A. López, J. M. Serna, and M. Azuaga, "Dipolo plano de banda ancha con balanceador de corriente integrado," in *XXI Simposium Nacional de la Unión Científica Internacional de Radio, URSI'06*, (Oviedo, Spain), pp. 1227–1231, 12-15 September 2006.

[59] E. García, E. de Lera Acedo, and E. Rajo, "Tapered slotline antenna modification for radiation pattern improvement," *Microwave and Optical Technology Letters*, vol. 49, no. 10, pp. 2590–2595, 2007.

[60] J. J. Lee and S. Livingston, "Wide band bunny-ear radiating element," in *Antennas and Propagation Society International Symposium Digest*, vol. 3, pp. 1604–1607, 28 June-2 July 1993.

[61] S. G. Hay and J. D. O'Sullivan, "Analysis of common-mode effects in a dual polarized planar connected-array antenna," *Radio Science*, vol. RS6S04, 2008.

[62] J. P. R. Bayard, M. E. Cooley, and D. Schaubert, "Analysis of infinite array of printed dipoles on dielectric sheets perpendicular to a ground plane," *IEEE Trans. On Antennas and Propagation*, vol. 39, pp. 1722–1732, December 1991.

[63] D. H. Schaubert and A. O. Boryssenko, "Subarrays of vivaldi antennas for very large apertures," in *Proc. 34th European Microwave Conference*, (Amsterdam), pp. 1533–1536, 2004.

[64] A. Ellgardt, "A scan blindness model for single-polarized tapered-slot arrays in triangular grids," *IEEE Transactions on Antennas and Propagation*, vol. 56, pp. 2937–2942, September 2008.

[65] J. Wunsch and D. Schaubert, "Full and partial crosswalls between unit cells of endfire slotline arrays," *IEEE Transactions on Antennas and Propagation*, vol. 48, pp. 981–986, June 2000.

[66] J.-P. R. Bayard, D. H. Schaubert, and M. E. Cooley, "E-plane scan performance of infinite arrays of dipoles on protruding dielectric substrates: coplanar feed line and e-plane metallic wall effects," *IEEE Transactions on Antennas and Propagation*, vol. 41, pp. 837–841, June 1993.

[67] E. L. Pelton and B. A. Munk, "Scattering from periodic arrays of crossed dipoles," *IEEE Transactions on Antennas and Propagation*, vol. 27, pp. 323–330, 1979.

[68] D. H. Schaubert, S. Kasturi, M. W. Elsallal, and W. van Cappellen, "Wide bandwidth vivaldi antenna arrays; some recent developments," in *Proc. EuCAP 2006*, (Nice, France), 6-10 November 2006.

[69] M. W. Elsallal and D. H. Schaubert, "Electronically scanned arrays of dual-polarized, doubly-mirrored balanced antipodal vivaldi antennas (dmbava) based on modular elements," in *IEEE Antennas and Propagation Society International Symposium 2006*, pp. 887–890, 9-14 July 2006.

[70] C. Craeye, "Efficient simulation off finite wideband arrays; reconciling finite and infinite-array approaches," in *SKADS MCCT Technical Workshop on Design of Wideband Receiving Array Systems*, (Dwingeloo, The Netherlands), 26-30 November 2007. available on http://www.astron.nl/other/workshop/MCCT/index.php.

[71] M. Ivashina, R. Maaskant, and B. Woestenburg, "Equivalent system representation to model the beam sensitivity of receiving antenna arrays," *IEEE Antennas and Wireless Propagation Letters*, vol. 7, pp. 733–737, 2008.

[72] E. de Lera Acedo, N. Razavi-Ghods, E. García, P. J. Duffett-Smith, and P. Alexander, "Analysis of an ultra wideband aperture array element for low frequency radio astronomy," in *IEEE Antennas and Propagation Society International Symposium, APSURSI '09*, (Charleston, SC), pp. 1–4, 1-5 June 2009.

[73] E. de Lera Acedo, N. Razavi-Ghods, E. García, P. J. Duffett-Smith, and P. Alexander, "System noise analysis of an ultra wide band aperture array element for low frequency radio astronomy," in *Proceedings of the 6th IASETD International Conference Antennas, Radar, and Wave Propoagation (ARP 2009)*, (Banff, Alberta, Canada), July 2009.

[74] E. de Lera Acedo, N. Razavi-Ghods, D. González-Ovejero, E. García, C. Craeye, P. J. Duffett-Smith, and P. Alexander, "The ska aa-lo array; e.m. simulation and design," in *Widefield Science and Technology for the SKA - SKADS Conference 2009*, (Chateau de Limelette, Belgium), November 2009.

[75] E. de Lera Acedo, N. Razavi-Ghods, E. García, P. Duffett-Smith, and P. Alexander, "Ultra wide-band aperture array element design for low frequency radio astronomy," *IEEE Transactions on Antennas and Propagation,*

special issue on Antennas for Next Generation Radio Telescopes, 2009. Submitted.

[76] www.lofar.org.

[77] www.mwatelescope.org.

[78] www.phys.unm.edu/ lwa/index.html.

[79] R. Braun and W. van Cappellen, "Aperture arrays for the ska: Dense or sparse?," SKA memo 87, June 2006. available on www.skatelescope.org.

[80] A. J. Boonstra, *Radio Frequency Interference Mitigation in Radio Astronomy*. PhD thesis, ASTRON, 2005. ISBN: 90-805434-3-8.

[81] A. Turtle and J. E. Baldwin *MNRAS*, vol. 124, p. 459, 1962.

[82] www.mathworks.com.

[83] G. C. Medellin, "Antenna noise temperature calculation," SKA memo 95, July 2007. available on www.skatelescope.org.

[84] C. G. T. Haslam, U. Klein, and C. J. Salter, "A 408 mhz all-sky continuum survey. i - observations at southern declinations and for the north polar region," *Astronomy & Astrophysics*, vol. 100, pp. 209–219, July 1981.

[85] P. Reich and W. Reich, "A radio continuum survey of the northern sky at 1420 mhz. ii," *Astronomy & Astrophysics*, vol. 63, pp. 205–288, February 1986.

[86] P. Reich, J. C. Testori, and W. A. Reich, "Radio continuum survey of the southern sky at 1420 mhz. the atlas of contour maps," *Astronomy & Astrophysics*, vol. 376, pp. 861–877, September 2001.

[87] J. L. Jonas, E. E. Baart, and G. D. Nicolson, "The rhodes/hartrao 2326-mhz radio continuum survey," *MNRAS*, vol. 297, pp. 977–989, July 1998.

[88] D. M. Pozar, *Microwave Engineering*. John Wiley & Sons Inc., 2nd ed., 1998.

[89] B. Woestenburg, "Definition of array receiver gain and noise temperature," SKA memo 98, February 2008. available on www.skatelescope.org.

[90] J. Jin, *The Finite Element Method in Electromagnetics*. Wiley-IEEE Press, 2nd ed., June 2002.

[91] Y. Li and J. M. Jin, "A vector dual-primal finite element tearing and interconnecting method for solving 3-d large-scale electromagnetic problems," *IEEE Transactions on Antennas and Propagation*, vol. 54, pp. 3000–3009, October 2006.

[92] Y. Li and J. M. Jin, "A new dual-primal domain decomposition approach for finite element simulation of 3d large-scale electromagnetic problems," *IEEE Transactions on Antennas and Propagation*, vol. 55, pp. 2803–2810, October 2007.

[93] Z. Lou and J. M. Jin, "A novel dual-field time-domain finite-element domain-decomposition method for computational electromagnetics," *IEEE Transactions on Antennas and Propagation*, vol. 54, pp. 1850–1862, June 2006.

[94] Z. Lou and J. M. Jin, "A dual-field domain-decomposition method for time-domain finite-element analysis of large finite arrays," *J. Comput. Phys.*, vol. 222, pp. 408–427, March 2007.

[95] V. V. S. Prakash and R. Mittra, "Characteristic basis function method: A new technique for efficient solution of method of moments matrix equation," *Microw. Opt. Technol. Lett.*, vol. 36, pp. 95–100, January 2003.

[96] M. Degiorgi, G. Tiberi, A. Monorchio, G. Manara, and R. Mittra, "An svd-based method for analyzing electromagnetic scattering from plates and faceted bodies using physical optics bases," in *IEEE Antennas Propagat. Soc. Int. Symp.*, vol. 1, (Washington, DC), pp. 147–150, 3-8 July 2005.

[97] C. Delgado, F. Cátedra, and R. Mittra, "Application of the characteristic basis function method utilizing a class of basis and testing functions defined on nurbs patches," *IEEE Transactions on Antennas and Propagation*, vol. 56, pp. 784–791, March 2008.

[98] G. A. E. Vandenbosch and F. J. Demuynck, "The expansion wave concept-part ii: A new way to model mutual coupling in microstrip arrays," *IEEE Transactions on Antennas and Propagation*, vol. 46, pp. 407–413, March 1998.

[99] L. Matekovits, V. A. Laza, and G. Vecchi, "Analysis of large complex structures with the synthetic-functions approach," *IEEE Transactions on Antennas and Propagation*, vol. 55, pp. 2509–2521, September 2007.

[100] W. B. Lu, T. J. Cui, Z. G. Qian, X. X. Yin, and W. Hong, "Accurate analysis of large-scale periodic structures using an efficient sub-entiredomain basis function method," *IEEE Transactions on Antennas and Propagation*, vol. 52, pp. 3078–3085, November 2004.

[101] E. Bleszynski, M. Bleszynski, and T. Jaroszewicz, "Aim: Adaptive integral method for solving large-scale electromagnetic scattering and radiation problems," *Radio Sci.*, vol. 31, no. 5, pp. 1225–1251, 1996.

[102] N. Engheta, W. D. Murphy, V. Rokhlin, and M. S. Vassiliou, "The fast multipole method (fmm) for electromagnetic scattering problems," *IEEE Transactions on Antennas and Propagation*, vol. 40, pp. 634–641, June 1992.

[103] W. C. Chew, J. Jin, E. Michielssen, and J. Song, *Fast and Efficient Algorithms in Computational Electromagnetics*. Norwood, MA: Artech House, 2001.

[104] Y. Zhang and T. K. Sarkar, *Parallel Solution of Integral Equation-Based EM Problems in the Frequency Domain*. John Wiley & Sons, Inc., 2009.

[105] D. González-Ovejero and C. Craeye, "Fast computation of macro basis functions interactions in non-uniform arrays," in *IEEE AP-S Soc. Int. Symp. 2008*, (San Diego, CA), July 2008 2008.

[106] E. Suter and J. R. Mosig, "A subdomain multilevel approach for the efficient mom analysis of large planar antennas," *Microwave and Optical Technology Letters*, vol. 26, pp. 270–277, March 2000.

[107] J. Yeo, V. Prakash, and R. Mittra, "Efficient analysis of a class of microstrip antennas using the characteristic basis function method (cbfm)," *Microwave and Optical Technology Letters*, vol. 39, pp. 456–464, December 2003.

[108] C. Craeye, "A fast impedance and pattern computation scheme for finite antenna arrays," *IEEE Transactions on Antennas and Propagation*, vol. 54, pp. 3030–3034, October 2006.

[109] C. Craeye and R. Sarkis, "Finite array analysis through combination of macro basis functions and array scanning methods," *Journal of Applied Comput. Electromagnetics Soc. (ACES)*, vol. 23, pp. 999–1007, September 2008.